THE DESIGN AND APPLICATION OF WIRELESS MEMS INERTIAL MEASUREMENT UNITS FOR THE MEASUREMENT AND ANALYSIS OF GOLF SWINGS

by

Kevin W. King

A dissertation submitted in partial fulfillment
of the requirements for the degree of
Doctor of Philosophy
(Mechanical Engineering)
in The University of Michigan
2008

Doctoral Committee:

      Professor Noel C. Perkins, Chair
      Professor Richard B. Gillespie
      Professor Karl Grosh
      Research Professor James A. Ashton-Miller

ACKNOWLEDGEMENTS

Table of Contents

List of Figures

Figure

List of Tables

CHAPTER 1

INTRODUCTION

1.1 Motivation and Background

Golf Swing Measurement Systems

Golf swing training aids address one of the major obstacles towards advancement in the sport, namely developing a controlled and consistent swing. The most common swing measurement systems utilize photographic technologies including high-speed video, motion capture cameras, or stroboscopic photography. High speed video, which is extensively used to capture both club and human kinematics [1-3], requires the careful alignment and calibration of two (and preferably three) high-speed cameras. Once the video is captured, the rather large video data files must be analyzed which can become computationally burdensome. In addition, the finite precision of positional and angular coordinates derived from digital images of a club must be carefully considered particularly when trying to resolve the three-dimensional motions of a complete golf swing. Alternatively, one may use optical tracking systems that employ transmitting 'markers' (often infrared LED's) placed on the golfer and the club. The use of optical markers may increase position accuracy and speed data analysis [4-6]. All camera-based systems require expensive equipment, careful set-up (alignment), and often controlled lighting. These limitations frequently restrict their use to specialized indoor facilities, although systems for outdoor use also exist. Motion capture is also possible using other media for triangulation including magnetic [7-8], radio frequency [9], and ultrasonic markers [10]. These alternatives may overcome some of the limitations of optical triangulation, such as the need for a direct line of sight, but they also have limitations arising from electro-magnetic and acoustic interference, portability, and cost. In addition,

all marker-based systems require the attachment of markers on, or in close proximity to, the club head which render these methods invasive to the club.

Measured swing data has also guided the development of mathematical models of golf swings. For instance, the multi-body models of Teu [11] and Tsunoda [12] are extensively compared with experimental swing measurements and reveal the limitations of the commonly used 'double pendulum' model of a golf swing. For example, Iwatsubo [13] explores the validity of assuming a rigid link connecting the wrist and neck. The planar dynamics of the golf swing predicted by the double pendulum model was addressed by Simon [14]. The interested reader is referred to [15] which reviews the scientific literature on swing dynamics including the many mathematical models of golf swings.

Pertaining to golf instruction, measurements of club acceleration, angular velocity, and club head speed reveal distinct differences between professional and amateur golfers [16-18]. Understanding and quantifying these differences is clearly essential for golf instruction. Research in golf swing instruction has largely focused on the human kinetics of the swing motion. For instance, high speed video was used to study the influences of hip and trunk motions [19-20]. Subsequently, shoulder [21-22] and knee [23] rotations were evaluated using optical motion tracking. The essential timing of all of these motions is emphasized in [15].

The golf swing measurement technologies reviewed above all generate quantitative measurements of swing dynamics. They also possess one or more major limitations including 1) extensive set-up and alignment, 2) restriction to indoor use, 3) high cost, 4) lack of portability, 5) placement of instruments (markers) on/near the head of the club, and 6) time consuming data processing and analysis. This study introduces an alternative means to measure golf swing dynamics that largely overcomes these limitations. In particular, we introduce a miniature and wireless six degree-of-freedom MEMS inertial measurement unit (IMU) that fits entirely within the shaft of a golf club at the grip end. Upon the development of a companion measurement theory, the resulting golf swing

training system achieves one example of a broad class of possible sports training aids based on this concept [24-25].

The Opportunity for a MEMS-Based Measurement System

The novel golf swing measurement system described in this study rests on the capabilities of MEMS inertial sensors including accelerometers and angular rate gyros. Ultimately, the sensor data are integrated in computing the position and orientation of the club which may execute both slow and fast dynamics depending on the swing (e.g., a putting stroke versus a full swing). The general system-level performance targets for an integrated IMU that can effectively resolve golf swings are summarized in the Table 1.1.

System Level Performance Targets				
Resolution	Angular < 1 deg Position < 6mm		Current Draw	< 40mA
Sensor Ranges	150 deg/s & 1.5g (putting) 2500 deg/s & 20g (full swing)		Battery Life	> 2 hours cont.
Sense Axes	Three-axis acceleration Three-axis angular velocity		Cross Section Diameter	< 13mm

Table 1.1: Performance targets for a miniature, MEMS-based IMU for resolving putting and full swings in golf and target limits on size and battery life.

MEMS accelerometer technology is relatively mature with MEMS devices nearing inertial-grade performance. The stringent stability requirements of inertial-grade devices establish performance goals for MEMS accelerometers as detailed in [26] and [27]. Specific device characteristics for accelerometers that enable the golf swing IMU described herein include low power (e.g., $600 \, \mu\text{A/axis}$), programmable ranges (e.g., 1.5 g to 15 g for three-axis devices), and small footprint (e.g., 5mm x 5mm for three-axis devices); see, for example, [28]. Many commercially available devices may be readily employed as part of the golf swing sensor system. MEMS angular rate gyros are significantly more complicated than accelerometers and their design remains an active research topic; see, for example [29-32]. A major goal is again to attain inertial grade performance which demands superior sensitivity, resolution, scale factor stability, and bias drift stability [29]. Key device characteristics for gyros that enable the golf swing

sensor IMU include low power (e.g., 6 mA/axis), adjustable ranges (e.g., 75 deg/s to 3000 deg/s), and small footprint (e.g., 7mm x 7mm); see, for example [33]. Several commercially available MEMS rate gyros meet these basic requirements. The ultimate performance of the integrated IMU rests on careful calibration of all (six) sensors as detailed herein. A major consideration is sensor drift but this concern is somewhat lessened in the golf application due to the rather short integration time intervals associated with golf swings (2-3 seconds typical).

Inertial Measurement Units and Error Sources

As reviewed above, currently available MEMS inertial sensors enable the development of a miniature and wireless six degree-of-freedom inertial measurement unit for measuring the dynamics of a golf swing. Within the context of sports training devices, the MEMS inertial sensors are deployed on the sports equipment and therefore measure both acceleration and angular velocity in a body-fixed frame of reference. This is the configuration used in the distinct field of inertial navigation where body-fixed inertial sensors form what is often called a "strap down inertial navigation system" [27, 34-35]. Systems capable of accurately measuring the rigid body dynamics of an object using a plurality of accelerometers and rate gyroscopes are commonly called inertial measurement units (IMUs). It is important to recognize and understand the work in this different field as many challenges in accurately measuring the dynamics of sporting equipment relate to methods in using IMUs to navigate ships, aircraft, spacecraft and missiles. Particularly useful are sensor error models and system calibration methods.

At the device level, the dominant error sources are fixed bias, scale factor, cross-axis coupling, vibro-pendulous error and random error [27]. Vibro-pendulous errors occur when the sensor is subjected to vibration along the sensitivity and pendulum axes simultaneously. Certain sensor designs are either impervious to or greatly reduce this error mechanism. There are four categories of bias error [27]. Fixed or repeatable bias error is a component that is predictable and present each time the sensor is switched on. Temperature-induced bias error arises from the unwanted effects of device heating and

4

can be corrected with suitable calibration. Switch-on to switch-on bias is a random error which varies from run to run but is otherwise constant for any one run. In-run variations are a random bias which varies throughout a run and the precise form of this error varies from one sensor type to another. The first two bias error types (fixed and temperature-induced) can be corrected with proper calibration. The performance of an IMU will be limited by the latter two forms of bias error (switch-on and in-run). These two types of error can also be compensated for if there is *apriori* knowledge about the motion of the body that can indicate the magnitude of these errors.

Static and quasi-static calibration methods are often used to identify sensor bias, scale factor error and system-level misalignment of the sense axes. Dynamic calibration methods are also used to quantify additional contributions to scale factor error as well as cross-coupling and vibro-pendulous error. Titterton [27] suggests the following error models for accelerometers and gyros to cover the majority of sensor errors.

Accelerometer Error Model

$$\vec{f}_{actual} = \vec{f}_{measured} - \delta\vec{f}$$

$$\begin{bmatrix} \delta f_x \\ \delta f_y \\ \delta f_z \end{bmatrix} = B_A + B_v \begin{bmatrix} a_y a_z \\ a_z a_y \\ a_x a_y \end{bmatrix} + S_A \begin{bmatrix} a_x \\ a_y \\ a_z \end{bmatrix} + M_A \begin{bmatrix} a_x \\ a_y \\ a_z \end{bmatrix} + w_A \qquad (1.1.1)$$

$f = \vec{a} - \vec{g}$, where f is the specific force measured by the accelerometers

B_A: A three element vector representing the fixed biases.
B_v: A 3x3 matrix representing the vibro-pendulous error coefficients.
S_A: A diagonal 3x3 matrix representing the scale-factor errors.
M_A: A 3x3 skew symmetric matrix representing the mounting misalignments and cross-coupling terms.
w_A: A three element vector representing in-run random bias errors.

Rate Gyro Error Model

$$\vec{\omega}_{actual} = \vec{\omega}_{measured} - \delta\vec{\omega}$$

$$\begin{bmatrix} \delta\omega_x \\ \delta\omega_y \\ \delta\omega_z \end{bmatrix} = B_G + B_g \begin{bmatrix} a_x \\ a_y \\ a_z \end{bmatrix} + B_{ae} \begin{bmatrix} a_y a_z \\ a_z a_x \\ a_x a_y \end{bmatrix} + B_{ai} \begin{bmatrix} \omega_y \omega_z \\ \omega_z \omega_x \\ \omega_x \omega_y \end{bmatrix} + S_G \begin{bmatrix} \omega_x \\ \omega_y \\ \omega_z \end{bmatrix} + M_G \begin{bmatrix} \omega_x \\ \omega_y \\ \omega_z \end{bmatrix} + w_G \qquad (1.1.2)$$

B_G: A three element vector representing the fixed biases.
B_g: A 3x3 matrix representing the *g*-dependent bias coefficients.
B_{ae}: A 3x3 matrix representing the anisoelastic coefficients.
B_{ai}: A 3x3 matrix representing the anisoinertia coefficients.
S_G: A diagonal 3x3 matrix representing the scale-factor errors.
M_G: A 3x3 skew symmetric matrix representing the mounting misalignment and cross-coupling terms.
w_G: A three element vector representing the in-run random bias errors.

In our research we will not need to consider all of the error sources incorporated into the two models above, however these error models serve as the foundation for our error correction strategies as will be described in Chapter 2.

The Role of Shaft Flexibility

The MEMS sensor technology discussed above is capable of measuring the *rigid body motion* of a golf club. In golf, the shaft of a driver and an iron is flexible and it is known to deflect during highly dynamic swings. Therefore, quantifying the contribution of flexible body dynamics to the golf swing is an important addition to a golf swing measurement system for drivers and irons. By contrast, there is little to no flexible body dynamics for a putter. In this research, we ultimately *predict* the flexible body dynamics of the shaft via a mathematical model for which the input is the rigid body accelerations and angular accelerations measured by the MEMS sensor. An alternative approach would be to embed sensors in the shaft (e.g. strain gauges) to directly measure the flexible body components as in [36]. However, this 'direct' approach has major disadvantages when considering future commercialization that include a) the invasive attachment of sensors

on or in the shaft (e.g., via epoxy), b) the added cost for significant preparation and installation of sensors during manufacturing, and c) the added system complexity (creation of many additional sensor channels, added signal conditioners, and significant temperature-dependence, etc.).

The mechanics of a golf shaft during a swing is well-approximated using classical linear theories for the bending and torsion of beams. A golf shaft has length to cross-section dimension (i.e. a slenderness ratio) consistent with the use of Euler-Bernoulli beam theory [37]. As mentioned above, the MEMS sensor directly measures the kinematics of the rigid motion of the shaft and specifically the rigid motion of the grip end of the club. This measured motion ultimately becomes the input to a flexible body model for the remainder of the club. One derivation of the general theory for a flexible beam undergoing large prescribed rigid body motions is developed by Kane et al. [38]. This theory assumes the flexible motion remains 'small' compared to the rigid body motion. Butler and Winfield [39] measured the deflections of the golf shaft and their results clearly demonstrate that the shaft deflections remain very small corrections to what is otherwise rigid body motion. The theory developed by Kane et al. [38] simplifies significantly when applied to a golf club since the shaft has uniform mass density and is cone shaped (tapered) which adds symmetry (e.g., eliminates products of inertia). For rotating circular beams, the model developed by Yigit et al. [40] is closer to that needed for a flexible golf club and thus it serves as a useful reference for this research. Suitable approximations to this model are also likely to yield accurate predictions of the flexible motion of a golf club as described in Chapters 5 and 6.

1.2 Research Objectives and Organization of Dissertation

Objectives

The objective of this research is to develop an accurate golf swing measurement and analysis system that is highly portable and potentially quite inexpensive. The measurement and analysis system relies on deducing the rigid body dynamics of the golf

club using embedded MEMS inertial sensors. Flexible body dynamics, if and when needed, are estimated using dynamical models of flexible golf shafts. A major related objective is to identify promising metrics of swing performance by systematically analyzing player putting strokes and full swings. These objectives are achieved through the theoretical and experimental studies outlined in the following five chapters.

Organization of Dissertation

Chapter 2 describes the theory, design and performance of a high-resolution, miniature, six degree-of-freedom, wireless IMU for measuring putting strokes. Section 2.1 opens with a careful development of the measurement theory for obtaining the kinematics of the putting stroke. The theory details how the raw sensor data (body-fixed measurements of acceleration and angular velocity) is reduced to yield the orientation, position, and velocity of the putter relative to a lab-fixed frame of reference. Section 2.2 follows with a detailed description of the wireless IMU design that includes sensors, micro-processor, wireless transceiver, and battery power supply. Section 2.3 presents test results that systematically explore the accuracy of the wireless IMU following precise calibration. To this end, a putting robot is also introduced which independently measures the kinematics of the putting stroke using a high-resolution optical encoder.

Chapter 3 employs the measurement theory and sensor hardware established in Chapter 2 to identify promising metrics of putting performance. This chapter opens with a review of the major literature on putting techniques and Section 3.2 follows by introducing a simple but very useful kinematic model for all putting strokes. This model is then applied to the highly controlled putting strokes using the putting robot (Section 3.3) and then to the unconstrained putting strokes of players (Section 3.4). The results of Section 3.5 clearly demonstrate how this technology can successfully deduce common faults in the putting strokes of players with varying skill levels.

Chapter 4 extends the measurement theory, hardware and experiments for putting strokes (Chapters 2 and 3) to the measurement and analysis of full golf swings with drivers and

irons. The chapter opens by summarizing the necessary changes in the hardware for resolving highly dynamic swings with drivers and irons. The resulting "high-range" sensor system is then used in Section 4.2 to explore the major features of the full golf swings. Results for the three-dimensional trajectory of the club and the clubface lie, loft and face angles reveal the major phases of the swing including the address, the backswing, the downswing, and the associated "wrist release" just prior to impact.

The results of Chapter 4 report the *rigid body* dynamics of golf clubs during highly dynamic full swings. The influence of shaft flexibility is now examined in Chapter 5 in the context of a two-dimensional model for the flexible shaft/club head system. This model includes the planar bending of the shaft as induced by the acceleration and angular acceleration of the grip during a swing. The derivation of the resulting two-dimensional model for a flexible club is detailed in Section 5.1 while Section 5.2 summarizes companion experimental results. Measurements of the bending natural frequency and transient dynamics for a flexible club demonstrate the accuracy of the two-dimensional model.

The final chapter, Chapter 6, extends the theory of Chapter 5 to a full three-dimensional model of a flexible golf club. Section 6.1 summarizes the derivation of the equations of motion for the shaft considering the simultaneous bending about two orthogonal axes and torsion about the long axis of the shaft. Section 6.2 summarizes initial experimental results for validating the three-dimensional model.

1.3 Summary of Major Research Contributions

Overall this research contributes a highly portable and inexpensive measurement and analysis system for analyzing golf swing dynamics. This contribution follows from the theory, design, and experimental evaluation of a wireless, six degree-of-freedom, MEMS inertial measurement unit that fits wholly within the shaft of a golf club. Additional contributions follow from applying this novel technology to understand both putting strokes and full swings.

For analyzing putting strokes, the measurement and analysis system resolves the three-dimensional position of the clubface to within 3 millimeters and the three-dimensional orientation of the clubface (i.e., the lie, loft and face angles) to within 0.5 degrees, both with millisecond updates. This measurement speed and significant precision enable the detailed characterization of putting strokes. In particular, the measurements support a simple kinematic model for all putting strokes that unifies the "pendulum style" and "gate style" strokes previously distinguished in the literature. In addition, a suite of "putting metrics" is identified that pin-points common putting faults from the measured club head trajectory and orientation. These findings confirm the significant opportunity for using this technology for putting instruction and training.

The same opportunity arises for full swings upon incorporating high-range angular rate gyros and accelerometers to resolve swings made with drivers and irons. By extending the measurement theory for putting, one can resolve the rigid-body dynamics of full swings from sensor data. Doing so immediately reveals two well-characterized swing planes, one for the backswing and one for the downswing, that are largely tangent to the otherwise three-dimensional trajectory of the club. In addition, one observes the significant acceleration of the club head that results from the "release of the wrists" in the downswing just prior to impact. Furthermore, the predicted clubface lie, loft and face angles at address and at impact provide immediate and valuable metrics of swing performance.

In addition to resolving the *rigid body* dynamics of a golf club, we propose and then demonstrate how the measurement theory can be extended to predict the *flexible body* dynamics as well, and with no additional sensor technology. Doing so relies on formulating dynamic models for the bending and twisting of the club shaft that incorporate, as inputs, the measured rigid body motion of the grip. This research contributes both two- and three-dimensional forms of the flexible body model of a golf club and experimental data that support their accuracy.

Beyond golf, the measurement theory and hardware design described in this dissertation hold significant promise for training systems for numerous other sports including, for example, baseball, hockey, tennis, and bowling. In addition, this technology has relevance to far broader fields of application including, for example, sports injury mechanics, rehabilitation science, gait analysis, surgeon training, etc. This research has contributed the foundation for these upcoming applications, many of which have already been initiated as a direct result of this study.

CHAPTER 2

WIRELESS MEMS INERTIAL SENSOR FOR
MEASURING GOLF PUTTING DYNAMICS

The objective of this chapter is to describe the design and performance of a novel sensor system. More specifically, we focus herein on a MEMS based IMU (inertial measurement unit) that measures the dynamics of the putting stroke, with stringent accuracy requirements placed on the computed orientation and position of the club head in three-dimensions. We open by reviewing the measurement theory that enables one to employ a club-fixed MEMS inertial sensor to compute the kinematics of the club including dynamic lie, loft and face angles of the club head, the velocity of the club head, and the path described by the club head in space. Next, we summarize the sensor hardware that incorporates MEMS inertial sensors, a microprocessor, and a wireless transceiver into a miniature, battery-powered IMU that can fit within the small confines of the golf club shaft. We then present experimental data that demonstrates the accuracy of the sensor system in measuring putting dynamics. We close with conclusions and a summary of the performance characteristics of the assembled sensor system.

2.1 Measurement Theory: Kinematics of a Golf Swing

The overall objective of this measurement system is to predict the kinematics of a golf swing and specifically the *orientation, velocity,* and *path* of the club head; see for instance, [18-20], [41-42]. This paper assumes that the golf club remains rigid throughout the swing, which is an appropriate assumption for putting as the club undergoes a slow, smooth motion that will not lead to appreciable flexing of the shaft. More precisely, we wish to predict three angles that define the orientation of the club head and the position and velocity of the geometric center of the face of the club head by exploiting

measurements from MEMS inertial sensors mounted remotely and within the grip end of the shaft of the club.

Definitions of Reference Frames and Orientation Angles

Consider Fig. 2.1(a) which illustrates a golf club at 'address', where the club is first lined up with the ball, and at the end of the backswing for a typical putting stroke. The geometric center of the face of the club is denoted by point f and the location of the sensor module within the shaft at the grip end is denoted by point s. At address, point f coincides with point O which is the origin of an inertial or *lab* frame $(\hat{I}, \hat{J}, \hat{K})$. In the lab frame, the unit vector $\hat{K}$ points vertically up (gravity $\vec{g} = -g\hat{K}$) and the unit vectors $(\hat{I}, \hat{J})$ define the horizontal plane with $\hat{J}$ aligned with the initial target line of the clubface which is established at address.
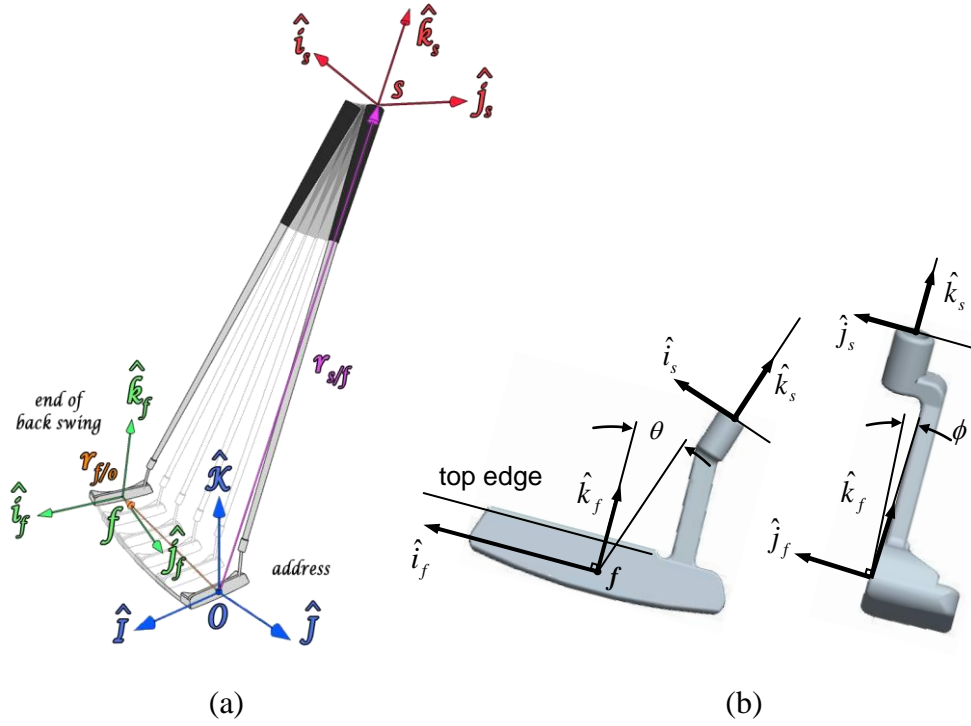
Figure 2.1: (a) Club illustrated at address ($t=0$) and at the end of the backswing during a putting stroke. The frame $(\hat{I}, \hat{J}, \hat{K})$ denotes a lab-fixed (inertial frame) at O which coincides with the location of the centroid f of the clubface at address. At address, $\hat{J}$ defines the target line. $(\hat{i}_f, \hat{j}_f, \hat{k}_f)$ denotes a body-fixed frame at f (face frame), whereas $(\hat{i}_s, \hat{j}_s, \hat{k}_s)$ denotes a body-fixed frame at s (shaft frame) within the shaft near the end of the grip. (b) Exploded club head view showing how the face frame and the shaft frame are related by the manufactured lie and loft angles θ and ϕ.

A body-fixed frame $(\hat{i}_f, \hat{j}_f, \hat{k}_f)$ is introduced at f, on the plane of the clubface, with $\hat{j}_f$ being the outward normal to this plane. The unit vector $\hat{i}_f$ lies in the plane of the face where it is chosen to be parallel to the flat indexing surface that defines the top of the clubface as shown in Fig. 2.1(b). The unit vector $\hat{k}_f$ then follows from $\hat{k}_f = \hat{i}_f \times \hat{j}_f$. A second body-fixed frame $(\hat{i}_s, \hat{j}_s, \hat{k}_s)$ is introduced at point s within the shaft at the grip. This frame defines the three mutually-orthogonal sense axes of the accelerometers and the angular rate gyros located within the shaft as detailed in the following section. The two body-fixed frames differ by a rigid-body translation $\vec{r}_{s/f}$ (position of s relative to f)

and a rotation that is determined *apriori* by the known club geometry. The rotation matrix $^F R^S$ defines this rigid body rotation per

$$\begin{pmatrix} \hat{i}_f \\ \hat{j}_f \\ \hat{k}_f \end{pmatrix} = {}^F R^S \cdot \begin{pmatrix} \hat{i}_s \\ \hat{j}_s \\ \hat{k}_s \end{pmatrix} \tag{2.1.1}$$

which, in turn, depends upon two angles determined by the design of the club. These two angles, referred to as the *manufactured club lie* θ and *loft* ϕ angles in Fig. 2.1(b), yield the following form for this rotation matrix

$$^F R^S = \begin{bmatrix} \cos\theta & \sin\phi\sin\theta & -\cos\theta\sin\phi \\ 0 & \cos\phi & \sin\phi \\ \sin\theta & -\sin\phi\cos\theta & \cos\phi\cos\theta \end{bmatrix} \tag{2.1.2}$$

The angles θ and ϕ are Euler angles and the rotation matrix of equation (2.1.2) is derived by first rotating an amount θ about the $\hat{j}_f$ direction and then an amount ϕ about the $\hat{i}_f$ direction. Notice here that the third Euler rotation about the $\hat{k}_f$ axis is 0.

The sensor module within the shaft measures the acceleration of point *s*, denoted $\vec{a}_s^S(t)$, and the angular velocity of the club, denoted $\vec{\omega}^S(t)$. Here the superscript *S* is used to emphasize that the components of these vectors are measured with respect to the body-fixed frame $(\hat{i}_s, \hat{j}_s, \hat{k}_s)$. The overall objective is to utilize these measurements, from MEMS inertial sensors mounted within the grip end of the shaft, to deduce the orientation of the club head as well as the velocity and position of point *f* dynamically during the putting stroke.

Defining the Orientation of the Club Head

We begin by defining the orientation of the club head which is equivalent to describing the orientation of the body-fixed frame $(\hat{i}_f, \hat{j}_f, \hat{k}_f)$ relative to the lab frame $(\hat{I}, \hat{J}, \hat{K})$. To this end, we introduce three orientation angles for the club head referred to as the *dynamic loft* α, *lie* β, and *face* σ angles. These three angles, which are commonly mentioned in the literature on golf, are critical in understanding the kinematics of a golf swing. Despite their common use however, there does not appear to be precise definitions for these angles. We answer this shortcoming by introducing the following definitions in reference to Fig. 2.2.
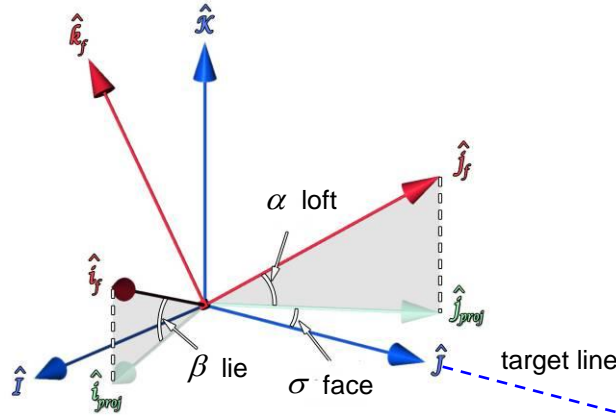
Figure 2.2: Definitions of dynamic loft $\alpha(t)$, lie $\beta(t)$ and face angle $\sigma(t)$ of the club head using projections of the face frame $(\hat{i}_f, \hat{j}_f, \hat{k}_f)$.

Begin by defining the loft angle α as the angle formed between the normal to the face, $\hat{j}_f$, and its projection, $\hat{j}_{proj}$, onto the horizontal plane. Next, define the lie angle β as the angle formed between the top edge of the face, $\hat{i}_f$, and its projection, $\hat{i}_{proj}$, onto the horizontal plane. Finally, introduce the face angle σ as the angle formed between $\hat{j}_{proj}$ and the original target line $\hat{J}$. When $\sigma > 0$, the face angle is said to be 'closed'; whereas when $\sigma < 0$, the face angle is said to be 'open'. Ideally one desires that $\sigma = 0$ at impact so that the ball travels solely along the original target line. For convenience below,

16

we also introduce the angle γ formed between $\hat{i}_{proj}$ and $\hat{I}$ which is determined by the prior three angles. To establish the relationship between γ and the other three angles one could use any of the constraint properties of direction cosine matrices. For example using the constraint that the columns of the matrix must be orthogonal, one could take the dot product of column 1 and 2, then solve for γ in terms of the other three angles. Recognize that the dynamic loft, α, and lie, β, of the club head vary significantly with time during the swing and that they are also distinct from the previously introduced manufactured loft, ϕ, and lie, θ, of the club which remain constant.

The dynamic orientation of the club head can now be defined by the rotation matrix $^{L}R^{F}$ between the body-fixed frame at f and the lab frame at O per

$$\begin{pmatrix} \hat{I} \\ \hat{J} \\ \hat{K} \end{pmatrix} = {}^{L}R^{F} \cdot \begin{pmatrix} \hat{i}_{f} \\ \hat{j}_{f} \\ \hat{k}_{f} \end{pmatrix} \tag{2.1.3}$$

Using the above definitions for $(\alpha, \beta, \sigma, \gamma)$, this rotation matrix becomes

$$^{L}R^{F} = \begin{bmatrix} \cos\gamma\sin\beta & -\sin\sigma\cos\alpha & \sin\gamma\cos\beta\sin\alpha - \sin\beta\cos\sigma\cos\alpha \\ \sin\gamma\cos\beta & \cos\sigma\cos\alpha & -\sin\beta\sin\sigma\cos\alpha - \cos\gamma\cos\beta\sin\alpha \\ \sin\beta & \sin\alpha & \cos\gamma\cos\beta\cos\sigma\cos\alpha + \sin\gamma\cos\beta\sin\sigma\cos\alpha \end{bmatrix} \tag{2.1.4}$$

Deducing the Instantaneous Orientation of the Club Head from Sensor Data

We shall now demonstrate how this rotation matrix can be constructed upon integrating the angular velocity of the club, $\vec{\omega}^{S}(t)$, to obtain the instantaneous or *dynamic* clubface loft, lie and face angles. The integration procedure begins by establishing the initial conditions of the clubface orientation angles as follows.

At address ($t=0$), the club is at rest, and thus

$$\vec{\omega}^{S}(0) = 0 \tag{2.1.5}$$

and

$$\vec{a}_s^S(0) = g\hat{K} \qquad (2.1.6)$$

In (2.1.6), we recognize that the MEMS accelerometer, which measures dynamic signals down to DC, detects an apparent upwards acceleration equivalent to gravity during address. Transforming this measured initial acceleration of point s from the shaft frame to the face frame via (2.1.2) yields

$$\vec{a}_s^F(0) = {}^F R^S \cdot \vec{a}_s^S(0) = a_x^F(0)\hat{i}_f + a_y^F(0)\hat{j}_f + a_z^F(0)\hat{k}_f = g\hat{K} \qquad (2.1.7)$$

where $(a_x^F(0), a_y^F(0), a_z^F(0))$ are the three components of gravity with respect to the face frame.

By definition at address, $\sigma(0) = 0$ which then simplifies ${}^L R^F$ (2.1.4). Using this simplified form, (2.1.3) yields

$$\hat{K} = \sin\beta(0)\hat{i}_f + \sin\alpha(0)\hat{j}_f + \cos\gamma(0)\cos\beta(0)\cos\alpha(0)\hat{k}_f \qquad (2.1.8)$$

Substituting (2.1.8) into (2.1.7) enables the solution of the initial clubface loft angle,

$$\alpha(0) = \sin^{-1}\left(\frac{a_y^F(0)}{g}\right) \qquad (2.1.9)$$

and the initial lie angle,

$$\beta(0) = \sin^{-1}\left(\frac{a_x^F(0)}{g}\right) \qquad (2.1.10)$$

from the measured initial acceleration data. Computation of $\gamma(0)$ follows readily from the same simplified form of (2.1.4) by exploiting the properties of this orthogonal transformation. For instance, using the fact that the first two columns are orthogonal yields

$$\gamma(0) = \sin^{-1}\left(-\frac{\sin\beta(0)\sin\alpha(0)}{\cos\beta(0)\cos\alpha(0)}\right) \qquad (2.1.11)$$

With the above initial conditions on the orientation angles, we now proceed to integrate the measured angular velocity vector forward in time. To this end, we rewrite the rotation matrix ${}^L R^F$ (2.1.4) in terms of standard Euler parameters [43]

$$
{}^{L}R^{F} = \begin{bmatrix} e_1^2 - e_2^2 - e_3^2 + e_4^2 & 2(e_1 e_2 - e_3 e_4) & 2(e_1 e_3 + e_2 e_4) \\ 2(e_1 e_2 + e_3 e_4) & e_2^2 - e_1^2 - e_3^2 + e_4^2 & 2(e_2 e_3 - e_1 e_4) \\ 2(e_1 e_3 - e_2 e_4) & 2(e_2 e_3 + e_1 e_4) & e_3^2 - e_1^2 - e_2^2 + e_4^2 \end{bmatrix} \tag{2.1.12}
$$

Evaluating both (2.1.4) and (2.1.12) at address ($t=0$) and equating components leads to the following initial conditions for the four Euler parameters

$$
e_1(0) = \frac{\sin \alpha(0) + \cos \gamma(0) \cos \beta(0) \sin \alpha(0)}{4 e_4(0)} \tag{2.1.13}
$$

$$
e_2(0) = \frac{\sin \gamma(0) \cos \beta(0)}{4 e_4(0)} \tag{2.1.14}
$$

$$
e_3(0) = \frac{\sin \gamma(0) \cos \beta(0) \sin \alpha(0) - \sin \beta(0) \cos \alpha(0) - \sin \beta(0)}{4 e_4(0)} \tag{2.1.15}
$$

$$
e_4(0) = \frac{1}{2} \sqrt{1 + \cos \gamma(0) \cos \beta(0) + \cos \alpha(0) + \cos \gamma(0) \cos \beta(0) \cos \alpha(0)} \tag{2.1.16}
$$

Next, we transform the measured angular velocity with components in the shaft frame to its equivalent representation with components in the face frame per

$$
\vec{\omega}^{F} = {}^{F}R^{S} \cdot \vec{\omega}^{S} \tag{2.1.17}
$$

The Euler parameter state equations for the face frame are [43]

$$
\dot{\vec{e}}^{F} = \frac{1}{2} \begin{bmatrix} e_4 & -e_3 & e_2 \\ e_3 & e_4 & -e_1 \\ -e_2 & e_1 & e_4 \\ -e_1 & -e_2 & -e_3 \end{bmatrix} \cdot \begin{pmatrix} \omega_x^F \\ \omega_y^F \\ \omega_z^F \end{pmatrix} \tag{2.1.18}
$$

which may now be integrated forward in time using the initial conditions (2.1.13)-(2.1.16) above and the measured angular velocity. This computation must also satisfy the constraint $e_1^2 + e_2^2 + e_3^2 + e_4^2 = 1$ which can be achieved in a variety of ways (e.g., via a penalty formulation following [44]).

The resulting Euler parameters at each time step can then be used to reconstruct the dynamic orientation angles of the face frame. Equating the components of (2.1.4) and (2.1.12) and solving for the dynamic clubface loft, lie and face angles yields

$$\alpha(t) = \sin^{-1}\left(2(e_2 e_3 + e_1 e_4)\right) \tag{2.1.19}$$

$$\beta(t) = \sin^{-1}\left(2(e_1 e_3 - e_2 e_4)\right) \tag{2.1.20}$$

$$\sigma(t) = \sin^{-1}\left(\frac{-2(e_1 e_2 - e_3 e_4)}{\cos\alpha}\right) \tag{2.1.21}$$

Deducing the Velocity and Position of the Club Head from Sensor Data

Upon determining the dynamic orientation of the club head relative to the lab frame, one may now turn attention to computing the absolute velocity and position of the clubface in the lab frame by suitable integration of the accelerometer data. We begin by first determining the absolute velocity and position of point s.

The acceleration of point s in the shaft is originally measured with respect to the shaft frame. Its equivalent representation with respect to the lab frame can be constructed by two successive rotations

$$\vec{a}_s^L = {}^L R^F \cdot {}^F R^S \cdot \vec{a}_s^S - g\hat{K} \tag{2.1.22}$$

Here, we also subtract gravity so that the remaining vector represents the absolute acceleration of point s. Integration of this result

$$\vec{v}_s^L(t) = \int_0^t \vec{a}_s^L(t)\,dt \tag{2.1.23}$$

yields the absolute velocity of point s in the lab frame recognizing that $\vec{v}_s^L(0) = 0$. One further integration yields the absolution position of point s in the lab frame

$$\vec{r}_s^L(t) = \int_0^t \vec{v}_s^L(t)\,dt + \vec{r}_s^L(0) \tag{2.1.24}$$

where

$$\vec{r}_s^L(0) = \vec{r}_f^L(0) + \vec{r}_{s/f}^L(0) \tag{2.1.25}$$

At address, $\vec{r}_f^L(0) = 0$ by definition. Furthermore,

$$\vec{r}_{s/f}^L = {}^{L}R^F \cdot {}^{F}R^S \cdot \vec{r}_{s/f}^S \tag{2.1.26}$$

where $\vec{r}_{s/f}^S$ is a *constant* vector known *apriori* from the club geometry. Pursuing our objective, one may now compute the absolute velocity and position of point f in the lab frame via

$$\vec{v}_f^L = \vec{v}_s^L + \left({}^{L}R^F \cdot {}^{F}R^S \cdot \vec{\omega}^S \times -\vec{r}_{s/f}^L \right) \tag{2.1.27}$$

$$\vec{r}_f^L = \vec{r}_s^L - \vec{r}_{s/f}^L = \begin{bmatrix} X\hat{I} \\ Y\hat{J} \\ Z\hat{K} \end{bmatrix} \tag{2.1.28}$$

where X, Y, and Z are Cartesian coordinates that describe the position of point f in a lab fixed frame.

2.2 Miniature Wireless IMU Hardware

Having established the measurement theory above, we now describe the inertial sensor unit that provides the requisite acceleration $\vec{a}_s^S(t)$ of point s and the angular velocity of the club, $\vec{\omega}^S(t)$, both measured with respect to the shaft frame. Begin with Fig. 2.3, which illustrates an exploded view of the portion of the IMU that contains the MEMS inertial sensors.
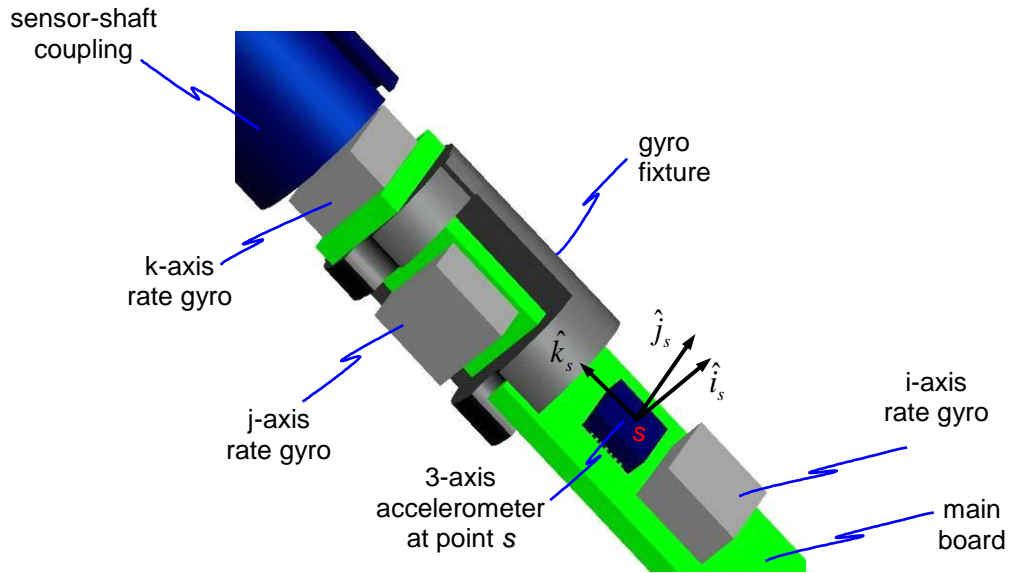
Figure 2.3: Partially exploded CAD drawing of a portion of the miniature IMU showing position and orientation of MEMS accelerometer and angular rate gyros. The location and orientation of the shaft reference frame $(\hat{i}_s, \hat{j}_s, \hat{k}_s)$ is defined by the sense axes of a tri-axis accelerometer. Three angular rate gyros on mutually-orthogonal faces have sense axes aligned with the axes of the accelerometer. The sensor circuit boards are highlighted in green.

This portion of the design consists of three sensor circuit boards (green) arranged to form three-mutually orthogonal planes. Mounted on the main board is a tri-axis accelerometer which defines point *s*. The orientation of the sense axes of this accelerometer defines the shaft fixed frame $(\hat{i}_s, \hat{j}_s, \hat{k}_s)$. Three single-axis angular rate gyros are illustrated having sense axes aligned with $(\hat{i}_s, \hat{j}_s, \hat{k}_s)$. The *i*-axis rate gyro is mounted on the main board whereas the *j*- and *k*-axis gyros are mounted on separate boards that define mutually-orthogonal planes with the main board. The orientation of all three planes is achieved by a small, machined gyro fixture that also provides mechanical support. The entire sensor assembly is captured at the upper end by a cylindrical coupling (portion shown) that assures the proper positioning and alignment of the IMU within the shaft of the club. The coupling forms a close slip fit with the inner diameter of the shaft and positive orientation of the IMU is provided via a small key way machined on the end of the shaft. A photo of

the entire assembled IMU is shown in Fig. 2.4 which also shows the physical scale of the design relative to the grip end of a golf club.
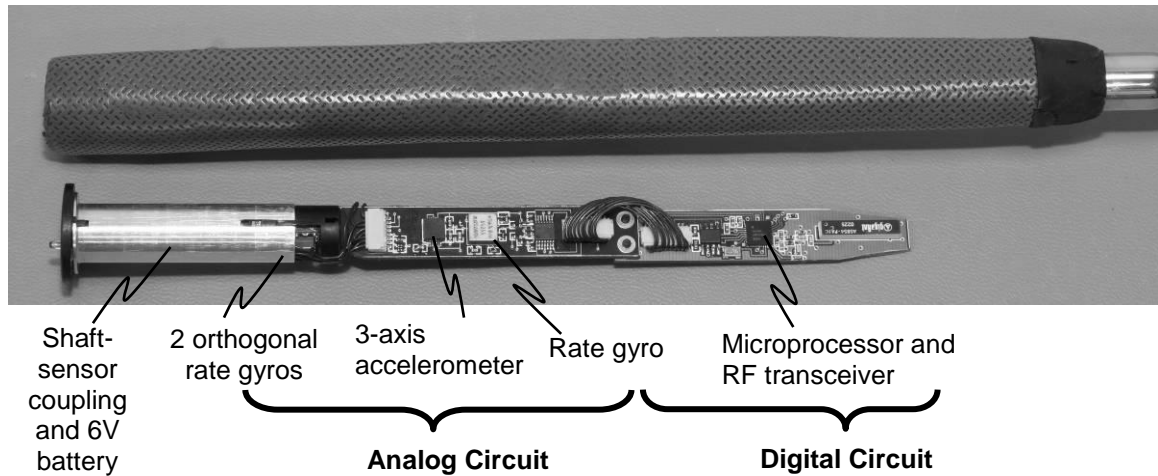
Figure 2.4: Photo illustrates the major components of the fully assembled wireless IMU that fits within the small confines of the shaft of a golf club. An analog circuit includes the MEMS inertial sensors (see Fig. 2.3) and a digital circuit includes a microprocessor, wireless transceiver, and an antenna. A battery is housed within the hollow shaft-sensor coupling at the far left.

The complete design yields a very compact and lightweight IMU that adds minimal mass to a golf club as detailed below. An analog circuit, powered by a regulated 5V source, includes the MEMS inertial sensors described above as well as a battery housed within the shaft-sensor coupling at the far left. Also at the far left is a small cap that finishes the end of the design and it is the only portion visible when the IMU is installed. A miniature power switch, which protrudes from this cap, is also visible in the photograph. A digital circuit finishes the opposite end of the design and it is powered by a regulated 3V source. The major digital components include a microprocessor (for performing 10-bit A/D, controlling RF transmission, and other circuit functions), a low-power RF transceiver (2.4GHz), and a surface-mount antenna.

The total continuous current draw of the assembled wireless IMU is 37mA including a 28mA draw from the analog components and a 9mA draw from the digital components. The total assembled mass is 25.1gm with 7.1gm (28%) of that total attributed the 6V

battery which provides continuous operation for two hours. The total mass is extremely small relative to that of a golf club (e.g., 490gm) rendering it virtually undetectable. Note that the total mass of the IMU is also a small fraction of the mass of a grip alone (60gm). The performance and accuracy limits of the design are carefully evaluated next.

2.3 Performance and Accuracy

The putting stroke is an excellent candidate for this sensor system since 1) the dynamics of the stroke are well within the design ranges of commercial MEMS accelerometers and angular rate gyros, and 2) the outcome of the putt is highly dependent on the orientation and position of the club head [41]. In addition, the entire stroke is completed within a very short time frame (typically 1-2 seconds), which minimizes the adverse influence of sensor drift, and within a modest bandwidth (e.g., 25 Hz). The putting stroke, however, does place stringent accuracy limits on the computed orientation angles of the clubface. For example, to make a 20 foot putt, the face angle σ must remain within 1 degree of the intended target line; refer to Fig. 2.2.

The accuracy of the computed clubface orientation angles, club head velocity, and club head position rests on: 1) the performance limits of the inertial sensors, 2) the calibration of the fully assembled IMU, and 3) the data reduction (integration) methods employed. Fortunately, the low noise and bias drift stability characteristics of most commercial MEMS inertial sensors lead to acceptable resolution limits for acceleration and angular velocity over the short duration, low bandwidth dynamics of the putting stroke. For instance, under these conditions, the noise limits of commercially available accelerometers and angular rate gyros remain less than 2 mg and 0.3 deg/sec, respectively.

System-Level Calibration

The system-level calibration of the wireless IMU employs algorithms adapted from [34-35]. In particular, the IMU is subject to three precise 180 degree rotations about each of the sensor axes $(\hat{i}_s, \hat{j}_s, \hat{k}_s)$ in succession; refer to Fig. 2.3. Prior to each rotation, the selected 'active' axis is aligned with gravity (and to within ± 0.03 deg via a bullseye level) so that the associated accelerometer undergoes a 2g change following a 180 degree rotation about a horizontal axis. This procedure is achieved using the custom calibration fixture pictured in Fig. 2.5 that includes a leveling plate (with bullseye level), a precision mounting block with a bored hole for fixturing the IMU, and a ground shaft equipped with a high-resolution optical encoder. The encoder is used to insure a 180 degree rotation to within the encoder resolution limits (± 0.07 deg).
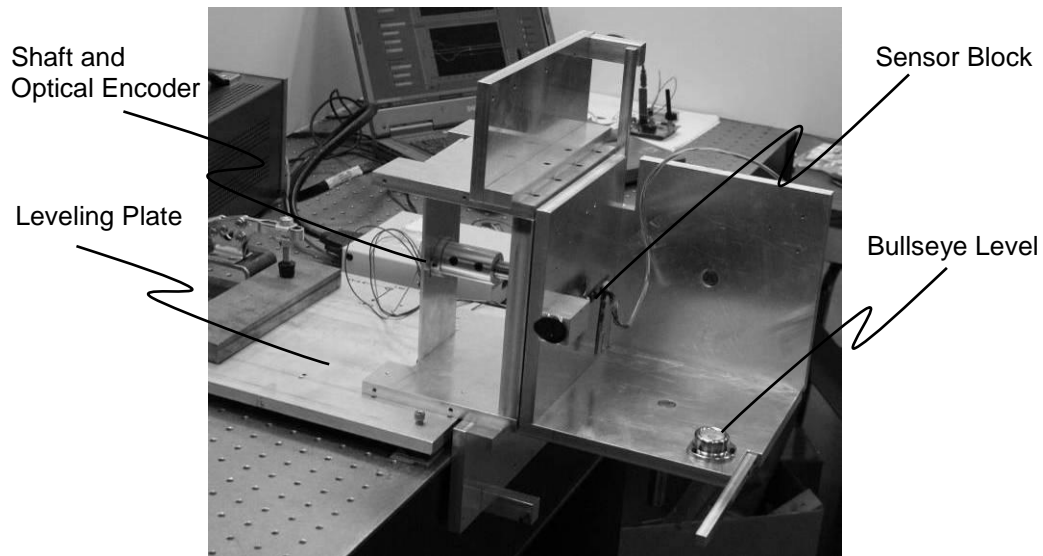
Figure 2.5: Calibration fixture used to characterize the 24 calibration constants for the assembled IMU. The principal components include a leveling plate, a bullseye level, a precision sensor mounting block, and a shaft with an optical encoder.

Calibration of the accelerometers is achieved by noting the sum and difference of the acceleration signals before and after each 180 degree rotation. The angular rate gyros are calibrated by requiring their integrated signals ultimately yield the controlled 180 degree rotation. This procedure characterizes 24 calibration constants for the assembled IMU.

These constants include the scale factor, the two cross-axis sensitivity scale factors, and the dc offset for each axis of the six degree-of-freedom sensor system. The cross-axis sensitivities originate from minute but unavoidable misalignment of the individual axes of each sensor relative to the axes $(\hat{i}_s, \hat{j}_s, \hat{k}_s)$ defined by the shaft of the club.

Once calibrated, the sensor system can be effectively used to measure putting strokes. Prior to doing so, however, we report next on the expected accuracy of these measurements.

Accuracy

We shall evaluate the accuracy of the sensor system by separately evaluating the accuracy achieved 1) at address of the ball, 2) during the putt, and 3) at impact of the ball. In each of these phases, the kinematical quantities obtained using the sensor system are benchmarked against those measured using independent instruments (e.g., optical encoders). We begin by considering time $t = 0$ when the club is at address with the ball.

At address, the club is momentarily still and the accelerometer signals yield the initial lie and loft of the club head as discussed in Section 2.2; refer to Eq. (2.1.9) and (2.1.10). To independently measure the initial orientation of the club, we again employ the calibration fixture which enables one to measure the lie and loft to within the limits of precision of the bullseye level (± 0.03 deg) and the optical encoder (± 0.07 deg). To this end, the platform is first leveled which establishes the origin (zero angle) for the optical encoder. The platform is then rotated about a horizontal axis to a new orientation as measured by the encoder and then held stationary while data are collected from the sensor. The initial orientation angles calculated by the MEMS sensor system are compared to those measured by the encoder over a wide range of initial lie and loft as reported in Table 2.12.. These results clearly demonstrated that the MEMS sensor system resolves the initial lie and loft angles to within $\pm \frac{1}{4}$ deg.

Accuracy at Address					
Range of Lie Angles	±50 deg		Range of Loft Angles	±50 deg	
Number of Tests	42		Number of Tests	40	
Average Angular Error	−0.01 deg		Average Angular Error	0.05 deg	

Table 2.1: Statistics of initial lie and loft angle testing. Table reports differences (error) between angles measured using the MEMS sensor system and an optical encoder for numerous tests over a large (±50 deg) range.

The initial lie and loft angles form the initial conditions for the subsequent computation of the dynamic lie, loft and face angles during a putting stroke; refer to Section 2.2. To evaluate the sensor accuracy during this dynamic phase and at impact with the ball, we designed an instrumented putting robot as illustrated in Fig. 2.6. This is a passive single degree-of-freedom robot that executes a perfect "pendulum-style" putt [41] by swinging freely under gravity. Even though this system is completely passive it will be referred to as a robot, since previous golf literature refers to similar fixtures as "robots". The robot swing is driven by gripping the upper arm and pulling the arm back to make the desired backswing and then releasing it, thereby allowing the forward swing to occur freely under the effect of gravity. The club is clamped at the grip below an adjustable "wrist joint" which is at the distal end of an adjustable "forearm". An "upper" arm connects an adjustable "elbow" joint to a "shoulder" joint which is supported by a horizontal shaft captured by a pair of bearings. The shaft incorporates an optical encoder for precise measurement of the rotation of the club (±0.1 deg) about the shaft at the shoulder joint. The pendulum robot yields a highly repeatable putting stroke wherein the forward swing repeats (in reverse) the backswing. Thus, at impact, the club head must return to the same position and orientation it had at address. This required 'closure' provides a powerful means to evaluate the accuracy of the sensor system during the dynamic phase of the putting stroke and with realistic putting speeds and range of motion.
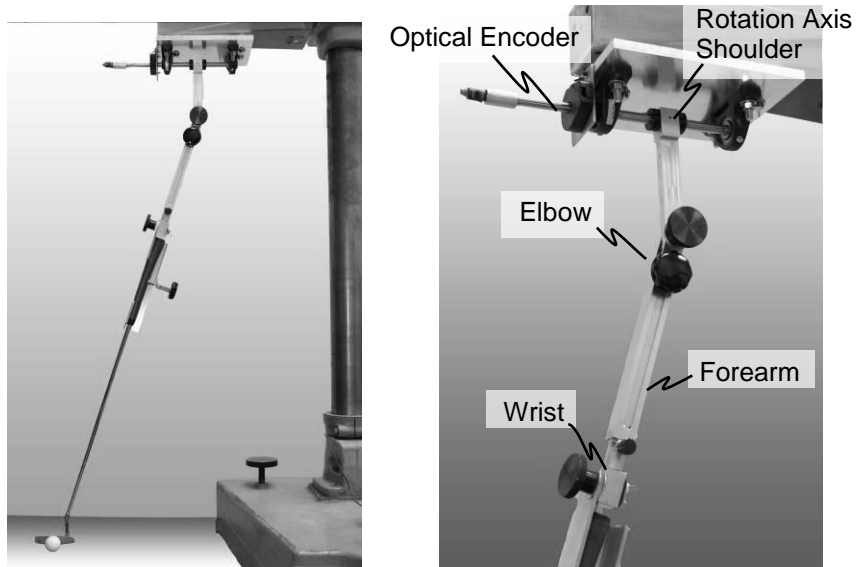
Figure 2.6: Single degree-of-freedom (pendulum) putting robot used to assess the accuracy of the sensor system during the dynamic phase of putting and at impact. Photos illustrate the principal components of the robot including a "shoulder" joint that allows rotation about one axis as measured by an optical encoder, adjustable (then fixed) "elbow" "forearm", and "wrist" joints, and a clamp that grips the club.

We next report results obtained from ten trials measured with the sensor system embedded in a club swung by the putting robot. The results include the *closure error* at impact as well as the *dynamic tracking error* during the backswing and forward swing. By *closure error*, we refer to the difference in the computed club head lie, loft and face angles between address and impact. Ideally, these differences should be zero as the putting robot enforces a kinematically closed path from address to impact. In addition, the angle measured by the encoder is equal to the clubface loft angle which provides a quantitative means to assess the accuracy of the sensor system all throughout the putting stroke. We refer to difference between these latter two measures as the *dynamic tracking error*.
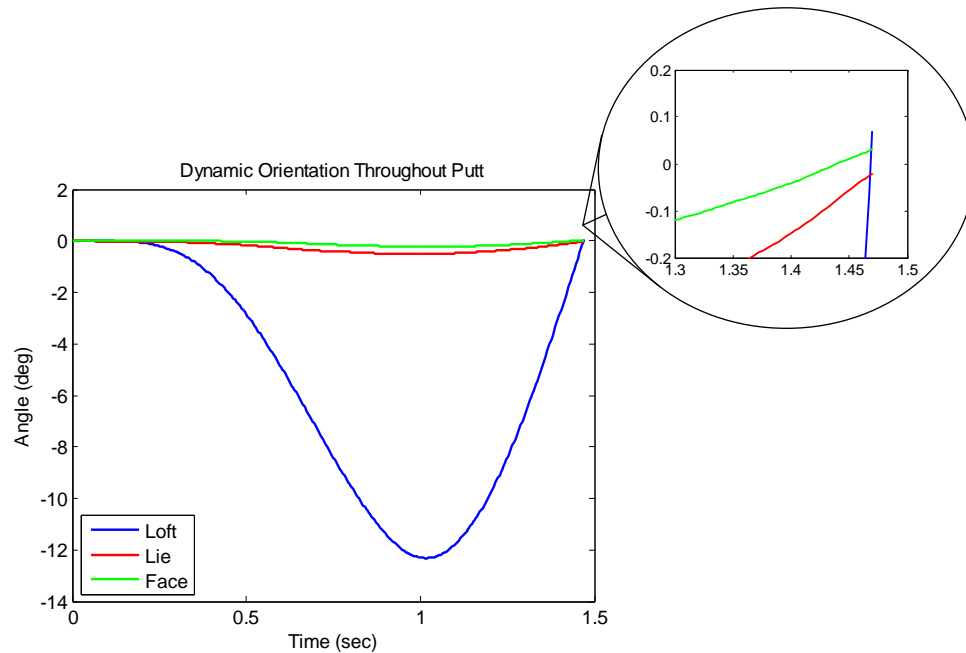
Figure 2.7: Dynamic loft, lie and face angles computed from MEMS sensor system for a typical swing using the putting robot.

Figure 2.7 illustrates typical results for the dynamic loft, lie and face angles for a swing using the putting robot from address ($t=0$ sec) to impact ($t \approx 1.5$ sec.). The initial (non-zero) loft and lie angles at address are subtracted from these results to better illustrate the closure errors at impact. Thus, all three angles start at zero and should ultimately end at zero at impact for perfect closure. In the example shown however, there is a minute closure error for the loft angle which finishes approximately at $+ 0.07$ degrees as shown in the enlarged view. The statistics of ten such closure tests are reported in Table 2.2 which includes the mean and standard deviation for the closure errors for the lie, loft and face angles, rounded to the nearest 0.1 degrees, which is the resolution of the optical encoder used to benchmark the IMU accuracy. These results confirm that the wireless, miniature IMU and the associated integration algorithm (Section 2.2) yield closure errors on the order of 0.1 deg (standard deviation) yielding highly accurate measurements of putting dynamics.

Angular Closure Errors for MEMS IMU			
	Lie Closure Error (deg)	Loft Closure Error (deg)	Face Closure Error (deg)
Mean	0.0	0.0	0.0
Stand. Dev.	0.1	0.1	0.1

Table 2.2: Mean and standard deviation of closure errors for clubface lie, loft and face angles for ten swings using putting robot. Results are rounded to the nearest 0.1 degrees because that is the resolution of the optical encoder used for independent measure.
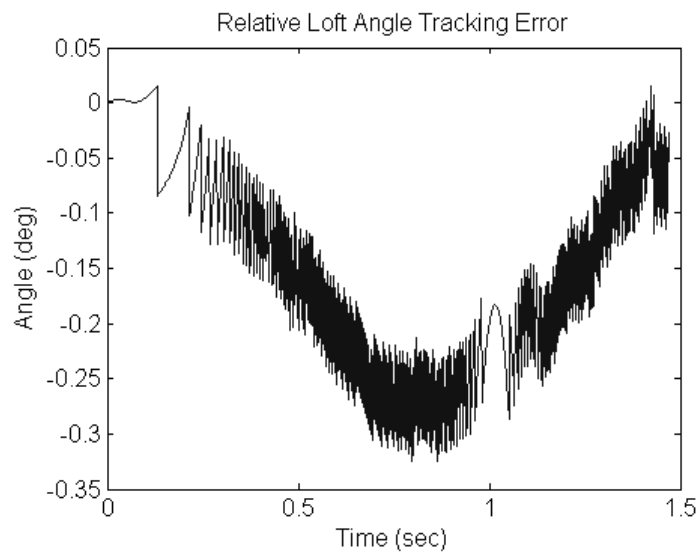
Figure 2.8: Enlarged view of dynamic tracking error during a typical swing with putting robot.

Figure 2.8 illustrates an enlarged scale view of the dynamic tracking error defined as the instantaneous difference between the loft angle computed using the MEMS sensor and that reported by the optical encoder. The loft angle changes by approximately 15 degrees during the swing and the maximum tracking error remains smaller than 0.35 degrees and has an average of 0.15 degrees. The average of the ten trials was 0.11 degrees. The dither in Fig. 2.8 is due to comparing the analog output of the sensor to the digital signal from the optical encoder. Since the resolution of the encoder is 0.1 degrees the fluctuation of approximately 0.1 degrees seen in Fig. 2.8 is expected. These results confirm that the tracking errors are also on the order of 0.1 degrees.

The results above consider the accuracy of the predicted lie, loft and face angles obtained using the rate gyro data and the algorithms summarized in Section 2.2. The accelerometer data are also used in tandem with the rate gyro data to predict the club head speed, the club head path, and ultimately the impact position of the ball on the clubface; refer again to Section 2.2. The putting robot requires that the clubface at impact align with its position and orientation at address. To demonstrate that the robot actually achieves this closed path, we directly measure the location of the impact using 'impact tape' for a number of swings. Impact tape leaves a visible mark where ball impact occurs as seen in the images of Fig. 2.9. These images confirm that the club path closes at impact to the same position as at address to within the (visual) resolution of the tape (approximately 2 mm).
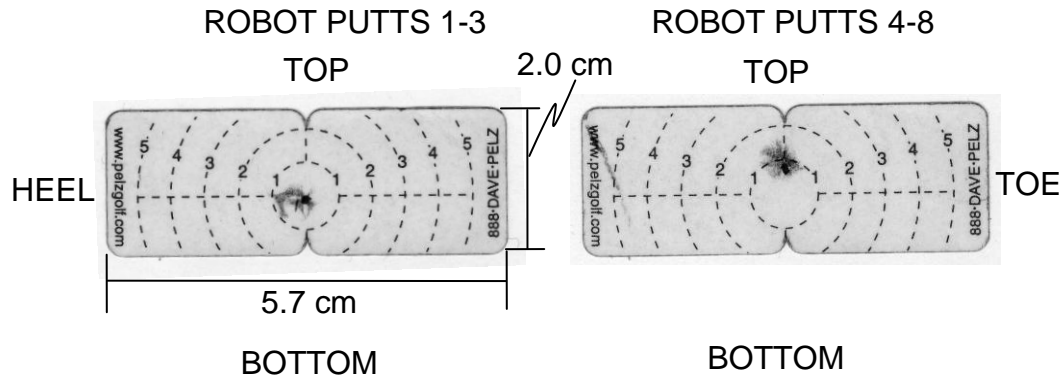
Figure 2.9: Impact tape records of eight swings made with the putting robot. Left (putt nos. 1-3) and right (putt nos. 5-8) records demonstrate that the clubface returns at impact to same position at address to within the (visual) accuracy of the tape (approximately 2 mm). The two impact tape strips are for identical setups of the robot, but allow a clear view of the impact patterns. The general dimensions of the tape are noted in the figure and the concentric circles increase in diameter by 1cm for each successive circle.

The predicted path of the club head for a typical putt is illustrated in Fig. 2.10 which illustrates the computed Cartesian coordinates of point f on the clubface relative to the lab-fixed frame; refer to $\vec{r}_{f/_o}^{\,L}$ in Fig. 2.1. The path largely lies in the (vertical,

$\hat{J} - \hat{K}$ plane) as expected. The maximum backswing position occurs at $Y \approx -32cm$ where the clubface has also been lifted $Z \approx 3cm$ above its height at address. The X motion

reaches a maximum $\approx 12mm$ which should be zero based on robot construction, but is the sum total effect of finite precision on aligning the sensor in the golf club and aligning the club in the robot. At impact, the closure on position is excellent as observable in the exploded view. Here the maximum position closure error is less than 3mm and it occurs in the vertical (*Z*) direction. The average and standard deviations of the position closure errors over ten swings are 0.0 ± 1.5 mm for the *X*-direction and 2.0 ± 1.3 mm for the *Z*-direction. These tight errors on position closure again confirm the accuracy of the design and the data reduction algorithm for resolving the dynamics of a putting stroke.
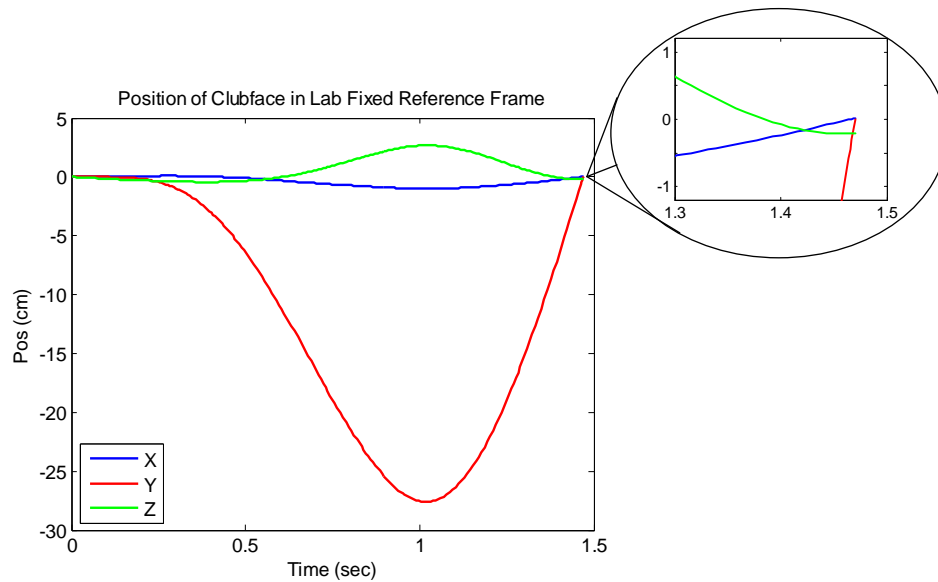
Figure 2.10: Computed Cartesian coordinates for path of point *f* on the face of the putter based on measured accelerometer and gyro data for a typical swing with the putting robot.

The accuracy measures above focus largely on the closure of the club head position and orientation at impact when using the putting robot. Given that the backswing and the forward swing of the robot trace the same path, one can also evaluate the accuracy of the MEMS sensor system at intermediate times during the swing. For example, Fig. 2.11(top) illustrates the computed path of the club head during the backswing (blue curve) and the forward swing (red curve) for a typical putt using the putting robot. The companion face angle data are presented in Fig. 2.11(bottom). The forward path traces nearly perfectly the path of the backswing; note the highly magnified scale for motion in the lab-based *X*-

direction (direction transverse to target line). Likewise, the face angle remains close to zero and retraces the same curve to a high degree. The small but systematic departure from the target line ($\hat{J}$-axis) in each case arises from a very small initial misalignment between the $\hat{i}_f$ axis of the sensor frame and the fixed axis of rotation of the putting robot. For this trial, the maximum deviation of the club head paths during the backswing and the forward swing is less than 1.5mm. Similarly, the maximum deviation between the face angles along these paths remains less than 0.03 degrees. Over ten such trails, the average and standard deviation for these path and angular errors were 2.3 ± 1.3 mm and 0.07 ± 0.09 degrees, respectively. These results again confirm that the MEMS sensor system and the associated numerical algorithms yield outstanding positional and angular accuracies for the objective of resolving a putting stroke.
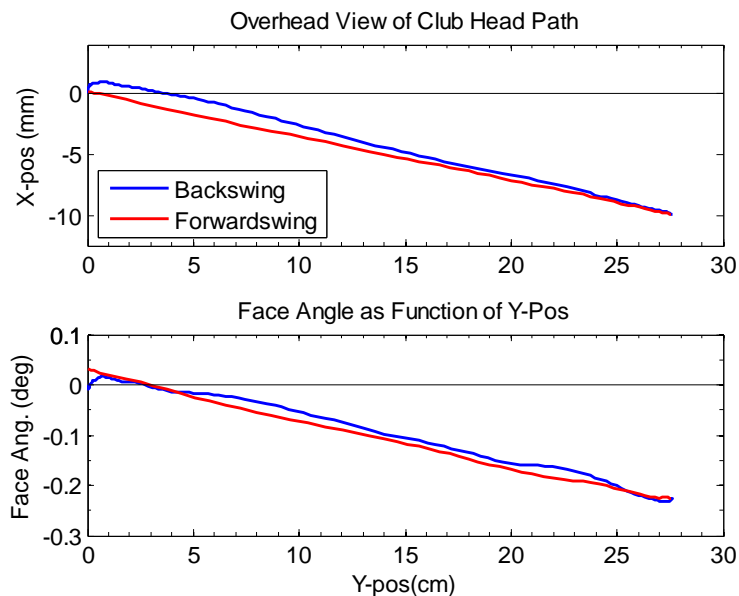
Figure 2.11: (Top) Overhead view of position data from one trial putt. (Bottom) Face angle as a function of position. Note the highly magnified scale for the X position coordinate (ordinate).

2.4 Closure

This chapter presents the theory, design, and experimental evaluation of a miniature, wireless six degree-of-freedom inertial measurement unit (IMU) for computing the dynamics of a golf swing. The design integrates a three-axis MEMS accelerometer, three single-axis MEMS angular rate gyros, a microprocessor, and a wireless (RF) transceiver in forming a battery-powered IMU that nests within the small confines of the shaft of a golf club. The inertial sensors, located at the grip end of the shaft, are used to compute the kinematics (e.g., velocity, position and orientation) of the club head located at the opposite end of the shaft. The requisite measurement theory is carefully developed and the accuracy of the assembled sensor system is systematically evaluated by experiment. The experiments utilize a putting robot that executes a highly repeatable 'pendulum' stroke for putting. The robot is equipped with an optical encoder for independent assessment of swing kinematics.

The achieved accuracy and performance of the MEMS sensor system for the target application (putting) are summarized in Table 2.3.

Accuracy and Performance				
	Angular Accuracy	Performance		
Initial Orientation	± 0.2 deg	Total Mass	25 g	
Absolute Orientation	± 0.5 deg	Total Current Draw	37 mA	
	Position Accuracy	X-Section Diameter	13 mm	
Absolute Position	± 3 mm	Continuous Run-Time	2 hr	

Table 2.3: Achieved accuracy and performance characteristics of the miniature, wireless MEMS IMU for putting dynamics.

By employing the measurement theory, the sensor system yields the position of the club head with an absolute accuracy of 3 mm and the orientation of the club head with an absolute angular accuracy of 0.5 degrees. The resulting design yields a highly portable, inexpensive, and highly accurate sensor system for measuring golf swing dynamics. Possible uses include golf swing training, custom club fitting, and club design. This sensor system also addresses many shortcomings of existing camera-based swing training

systems. The example sensor system for putters is readily adapted to other golf clubs (irons and drivers) by appropriately changing the dynamic ranges of the inertial sensors.

CHAPTER 3

UNDERSTANDING PUTTING STROKE KINEMATICS
VIA THE MEMS SENSOR

The objective of this chapter is to use the MEMS sensor detailed in the previous chapter to quantify the putting stroke and thereby advance the fundamental knowledge of putting techniques. In realizing this objective, we also propose a generalization of all putting strokes by introducing a two-parameter kinematic model of putting. This model unifies the previous classifications of putting strokes which were categorized as either "pendulum style" strokes or "gate style" strokes [41]. The MEMS sensor technology allows us to quantitatively explore these two putting styles and to demonstrate their strong relationship through a simple kinematic model. In addition, this chapter introduces a novel diagnostic tool for analyzing putting strokes and quantitative metrics for common putting faults. We begin by reviewing the literature specific to putting techniques.

3.1 Literature Specific to Putting Techniques

A successful putt requires skill in reading the green, aligning the putt, and then striking the ball with the club. This technology, which focuses on mechanics of the golf swing, is a tool to evaluate the last skill. Nevertheless, we recognize the importance of reading the green and properly aligning the putt at address.

The putting stroke ultimately determines the initial velocity and angular velocity of the ball following impact. These 'initial conditions' for the ball following impact result from three prior conditions at the time of impact, namely: 1) the velocity of the club head, 2) the orientation of the club head, and 3) the impact location of the ball on the clubface. As the means to explain how players develop these impact conditions, coaches and teachers often study related aspects of the putting stroke that are easier to describe such as the

"putter path" (e.g., the path traced by the centroid of the club head during putting) and the "power source" (e.g., the sources of the kinetic energy of the club). After surveying the writings of three well-respected teachers, David Pelz [41], Stan Utley [45], and Edward Craig [46], we summarize a contemporary understanding of the putting stroke.

David Pelz, who is a coach of PGA players and author of *Dave Pelz's Putting Bible* [41], advocates a kinematically simple and thus "repeatable" stroke often referred to as the "pendulum style" stroke. In this stroke, the putter head never deviates from the intended target line and the putter face remains square to this target line. Thus, following address, the putter head is brought back along the target line and raised slightly above the green in proportion to the length of the 'backswing'. The forward swing is the reverse motion which is ideally powered solely by the gravitational potential energy of the club as if it were a simple pendulum; refer to Fig. 3.1(a).

(a)   (b)
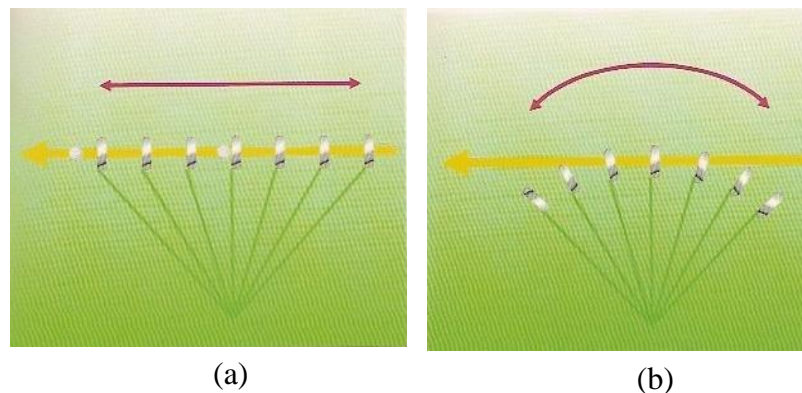
Figure 3.1: Illustration of pendulum and gate style putting strokes as viewed from overhead [41]. (a) Pendulum stroke is also referred to the Pure Inline and Square (PILS) stroke by Pelz. (b) Gate stroke, showing the club head moving on an arc and the clubface opening and closing during the stroke.

Pelz concludes that the pendulum style stroke, or the Pure Inline and Square "PILS" stroke, is the stroke players should adopt since the use of gravity alone to power the club leads to a highly repeatable stroke. He also mentions that the "gate" or "screen door" stroke taught by Harvey Penick, a highly respected golf teacher, is based on a pendulum motion where the axis of rotation is inclined from the horizontal. This is a keen

observation that we later return to in developing a simple kinematic model for all putting styles. Pelz asserts that if the axis of rotation is inclined from the horizontal, the player must supply a reaction force (actually a reaction torque) to maintain this angle against gravity. This reaction force is a perturbation to the PILS stroke.

Stan Utley, who is a current professional player, a current coach of PGA players, and author of *The Art of Putting* [45], teaches putting using a natural, free-flowing swing. He advocates for the putting stroke being a miniature version of a "full swing' and this also leads to a "gate style" putting stroke. The gate style swing derives its name from the analogy of a swinging gate whose hinge line is not plumb. As the gate 'opens', the center of mass of the gate raises slightly and then falls as the gate 'closes.' Kinematically, the club head during a gate swing follows a slightly curved path, when viewed from overhead, the clubface opens relative to the target line during the backstroke, and then closes during the forward stroke. Ideally, the clubface remains perpendicular to the putter path throughout the stroke so that at impact the face is again square to the target line; refer to Fig. 3.1(b).

Edward Craig, who is the editor of Britian's top golf magazine *Golf Monthly* and author of *Putt Perfect* [46], discusses the potential benefits of both the gate and the pendulum strokes. Craig focuses on the motion of the shoulder, arms and wrists and concludes that the motions of these body parts should be independent of the putter path. He says that the shoulder muscles should be the power source for the backswing. The arms and wrists should provide a rigid connection from the rotation axis to the putter. The lower body should remain still.

3.2 Two-Parameter Kinematic Model for Putting

A keen reader may note that the description of the gate stroke above lacks a precise definition. By contrast, the pendulum (or PILS) stroke definition precisely describes the path and orientation of the putter head. Thus, while there are definitive means to test whether a stroke comes close to an ideal pendulum stroke, no analogous means have been

proposed to test whether a stroke comes close to an ideal gate stroke. We shall now introduce a two-parameter kinematic model of the putting stroke that quantitatively predicts the path and orientation or the putter head for all strokes, including ideal pendulum and gate strokes. Later, we also show that this model correlates well with the measured putts from players of varying skill levels.

Figure 3.2: Definition of two-parameter kinematic model for putting. (a) The parameter Θ defines the angle the rotation axis makes with the horizontal and the parameter L_{arm} defines the perpendicular distance from the rotation axis to the top of the grip (point s). (b) View in the $\left(\hat{J}', \hat{K}' \right)$-plane showing the parameters L_{arm}, Y_{grip}, and the angle of rotation Φ about the rotation axis.

Figure 3.2 illustrates the proposed model which has a single rotational degree of freedom and is defined by the two parameters Θ and L_{arm}. Θ is the angle that the rotation axis makes with the horizontal and L_{arm} is the perpendicular distance from the rotation axis to the top of the grip. The top of the grip is essentially point s, the origin of the body fixed sensor frame $\left(\hat{i}_s, \hat{j}_s, \hat{k}_s \right)$ defined in the previous chapter.

Establishing the Model Parameters from Experimental Data

We now illustrate how to construct the model parameters Θ and L_{arm} from the measured data from a player's putt. Doing so also allows us to predict the ideal kinematics of the player's putt as predicted by a model that most closely fits the player's natural stroke. This is a novel approach in that the player's stroke is ultimately compared to a standard that closely fits the natural stroke of the player rather than to some pre-determined standard (say a perfect pendulum stroke).

Figure 3.2(a) illustrates a lab-fixed frame $\left(\hat{I}', \hat{J}', \hat{K}' \right)$, where $\hat{I}'$ is aligned with the rotation axis. This frame is distinguished from the second lab-fixed frame $\left(\hat{I}, \hat{J}, \hat{K} \right)$ by the rotation Θ about the $\hat{J}' = \hat{J}$ axis. The angular velocity vector $\vec{\omega}$ of the club is along $\hat{I}'$ and thus orthogonal to $\hat{J}$. The $\hat{I}$ and $\hat{K}$ components of $\vec{\Omega}$, Ω_x and Ω_z respectively, are related to Θ through

$$\tan \Theta = \frac{\Omega_z}{\Omega_x} \tag{3.2.1}$$

The quantities Ω_x and Ω_z can be derived from the sensor measurements of $\vec{\Omega}$.

The position vector $\vec{R}_{s/p}$ lies wholly within the $\left(\hat{J}', \hat{K}' \right)$ plane and the length of this vector is the parameter L_{arm}. One may compute L_{arm} from the $\hat{J}$ component of the grip position Y_{grip}, upon computing the rotation angle Φ as suggested in Fig. 3.2(b). Φ is computed by integrating $\vec{\Omega}(t)$ using $\Phi(0) = 0$ at address. These quantities are related through

$$L_{arm} = \frac{Y_{grip}}{\sin(\Phi)} \tag{3.2.2}$$

The quantity Y_{grip} is derived from the sensor measurements as detailed in Chapter 2.

Predicting the "Ideal Putt" Based on the Model

Having established a method for determining the model parameters, we now predict the kinematics of the "ideal" putt as predicted by the model. The key kinematical quantities to predict include the three club head orientation angles (lie, loft, and face angles) and the path of the putter head.

The model assumes that the club rotates about a constant rotation axis, $\vec{\lambda} = \hat{I}'$. Thus, the Euler parameters for this rotation are easily derived [43]. Explicit expressions for the rotation axis and Euler parameters as functions of Φ and Θ are

$$\vec{\lambda} = \cos\Theta\hat{I} + 0\hat{J} + \sin\Theta\hat{K}$$

$$\begin{bmatrix} e_1 \\ e_2 \\ e_3 \end{bmatrix} = \vec{\lambda}\sin\frac{\Phi}{2} = \begin{bmatrix} \cos\Theta\sin\dfrac{\Phi}{2} \\ 0 \\ \sin\Theta\sin\dfrac{\Phi}{2} \end{bmatrix} \qquad (3.2.3)$$

$$e_4 = \cos\frac{\Phi}{2}$$

In the previous chapter the relationships between the Euler parameters and the clubface orientation angles (lie, loft, and face angles) were derived and are reproduced here as

$$\alpha(t) = \sin^{-1}\left(2(e_2 e_3 + e_1 e_4)\right)$$
$$\beta(t) = \sin^{-1}\left(2(e_1 e_3 - e_2 e_4)\right)$$
$$\sigma(t) = \sin^{-1}\left(\frac{-2(e_1 e_2 - e_3 e_4)}{\cos\alpha}\right) \qquad (3.2.4)$$

By substituting the results of Eq. (3.2.3) into Eq. (3.2.4), the simple kinematic model yields the lie, loft and face angles of the club head throughout the putting stroke.

To predict the putter path, we now develop an expression for the vector $\vec{R}_{f/p}$ illustrated in Fig. 3.3(a).

At Address (t=0)   View along axis

(a)   (b)
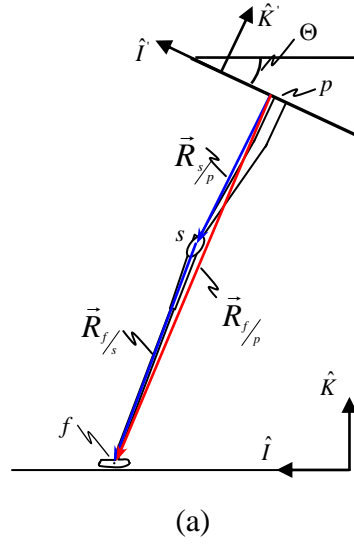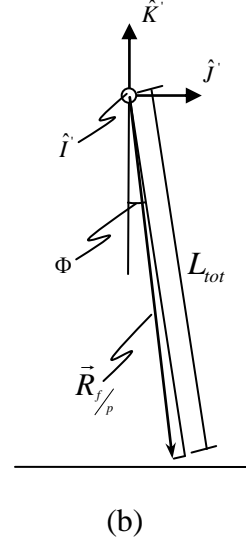
Figure 3.3: (a) Definitions of $\vec{R}_{s/p}$, $\vec{R}_{f/s}$, and $\vec{R}_{f/p}$, which are used to describe the predicted putter path based on the model proposed in this section. (b) View looking down the $\hat{I}'$ direction showing the constant length L_{tot}.

Figure 3.3(b) illustrates the distance L_{tot}, which is the $\hat{K}'$ component of the vector $\vec{R}_{f/p}$ when the club is at address $\Phi = 0$. This distance is constant as it is determined by the (constant) putter geometry and the parameter L_{arm}. To derive an expression for $\vec{R}_{f/p}$, first we establish $\vec{R}_{f/s}$ at address and then $\vec{R}_{s/p}$ for all time t as follows.

$$\vec{R}_{f/s}(0) = X(0)\hat{I} + Y(0)\hat{J} + Z(0)\hat{K} \tag{3.2.5}$$

$$\vec{R}_{s/p} = L_{arm}\sin\Phi\hat{J}' - L_{arm}\cos\Phi\hat{K}' \tag{3.2.6}$$

$\vec{R}_{f/s}$ is most conveniently written using the $\left(\hat{I}, \hat{J}, \hat{K}\right)$ frame while $\vec{R}_{s/p}$ is conveniently written using the $\left(\hat{I}', \hat{J}', \hat{K}'\right)$ frame. The components of $\vec{R}_{f/s}$ are the result of calculating the initial position of the golf club as detailed in Chapter 2 and $\vec{R}_{s/p}$ can be derived by inspection of Fig. 3.2. The transformation between these two frames, $^{I'}C^L$, which is required prior to adding these two vectors, is given by

$$
\begin{bmatrix} \hat{I}' \\ \hat{J}' \\ \hat{K}' \end{bmatrix} = {}^{L'}C^{L} \begin{bmatrix} \hat{I} \\ \hat{J} \\ \hat{K} \end{bmatrix} = \begin{bmatrix} \cos\Theta & 0 & \sin\Theta \\ 0 & 1 & 0 \\ -\sin\Theta & 0 & \cos\Theta \end{bmatrix} \begin{bmatrix} \hat{I} \\ \hat{J} \\ \hat{K} \end{bmatrix} \tag{3.2.7}
$$

Evaluating equation (3.2.6) at $t = 0$ and $\Phi = 0$, and applying equation (3.2.7) yields the following expression for the vector $\vec{R}_{f/p}$ at address

$$
\vec{R}_{f/p}(0) = \left(X\cos\Theta + Z\sin\Theta \right)\hat{I}' + Y\hat{J}' + \left(-X\sin\Theta + Z\cos\Theta - L_{arm} \right)\hat{K}' \tag{3.2.8}
$$

The distance L_{tot} is the $\hat{K}'$ component. The $\hat{I}'$ component remains constant since the club is rotating about the $\hat{I}'$ axis. The final expression for $\vec{R}_{f/p}$ at any time t is given as follows where the superscripts L and L' are used to denote which lab-fixed frame is used to describe each vector quantity.

$$
\begin{aligned}
\vec{R}_{f/p}^{L'} &= \left(X\cos\Theta + Z\sin\Theta \right)\hat{I}' + \left(Y\cos\Phi + L_{tot}\sin\Phi \right)\hat{J}' + \left(Y\sin\Phi - L_{tot}\cos\Phi \right)\hat{K}' \\
\vec{R}_{f/p}^{L} &= {}^{L}C^{L'}\vec{R}_{f/p}^{L'} \\
{}^{L}C^{L'} &= \left({}^{L'}C^{L} \right)^{T}
\end{aligned} \tag{3.2.9}
$$

Equation (3.2.9) can now be used to predict the path of the center of the putter face, point *f*, throughout the putt.

Shortly we shall demonstrate that this simple model correlates well with the measured putting strokes from subject players. Before analyzing the player strokes however, we first present measurements of putts made using the putting robot described in the previous chapter. Doing so allows us to confirm the accuracy of the kinematic model in a mechanism that truly possesses just a single degree-of-freedom.

3.3 Evaluation of Robot Putting Strokes Using Kinematic Model

The putting robot introduced in the previous chapter is now used to demonstrate the utility of the two-parameter kinematic model under highly controlled conditions. Figure 3.4 reintroduces the putting robot which is essentially a single degree-of-freedom

pendulum with adjustable linkages extending from the axis of rotation to the grip on the club.
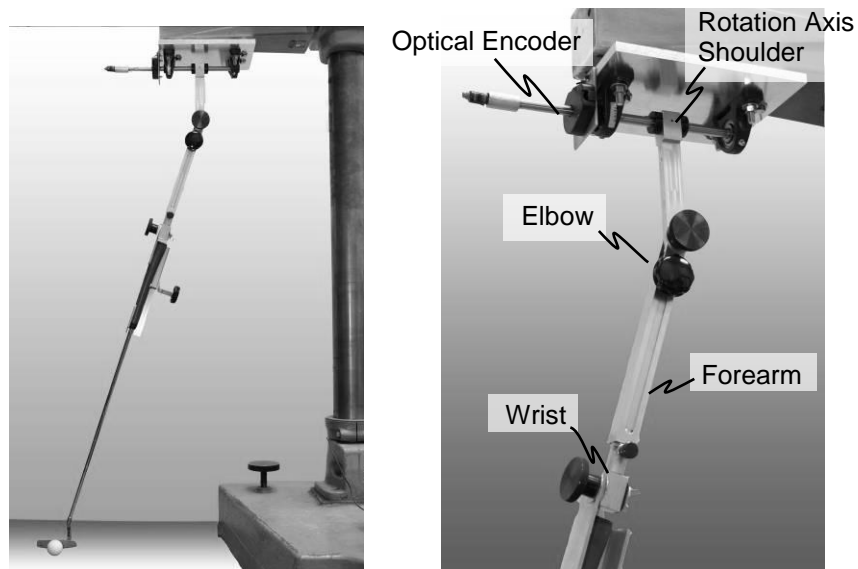
Figure 3.4: Images of the putting robot introduced in the previous chapter.

The putting robot was used to perform both PILS strokes and gate strokes by simply controlling the orientation of the axis of rotation. For the PILS stroke, the angle $\Theta = 0$. For example gate strokes, the robot base was inclined to achieve $\Theta \approx 10^\circ$. Measured putting data for both types of strokes is summarized below.

Starting with the PILS strokes, Eq. (3.2.1) was used to estimate an average inclination angle $\Theta \approx 1.1^\circ$ from computed results of Ω_x and Ω_z. This rather small angle is quite reasonable considering that the robot base is essentially level. Direct measurement of the parameter L_{arm} provides $L_{arm} \approx 21.5 \pm 0.25\, in$. This agrees well with the value $L_{arm} \approx 21.51\, in$ (and standard deviation 0.37 in) predicted from Eq. (3.2.2) based on the average of 10 trials. Having established that parameters of the model and the physical set up agree, we next present results for the predicted and measured clubface orientation and path.

The model predicts the orientation of the putter face throughout the putting stroke using Eqns. (3.2.3) - (3.2.4). The sensor measurements provide direct measurement of these

same quantities per the theory developed in Chapter 2. Figure 3.5 compares the orientation angles of the putter face predicted by the model and measured from the sensor data for a typical PILS stroke by the putting robot. The predicted loft angle (cyan curve) and the measured loft angle (blue curve) lie nearly on top of each other demonstrating excellent correlation between the simple model and the sensor measurements. Similarly good agreement is observed for the face angle (black curve = predicted vs. green curve = measured). A slight disparity exists between the measured lie angle (red curve) and the predicted lie angle (magenta curve). This modest difference derives from a slight misalignment of the sensor axes in the putter relative the axis of rotation of the robot as revealed next in an analysis the putter path.
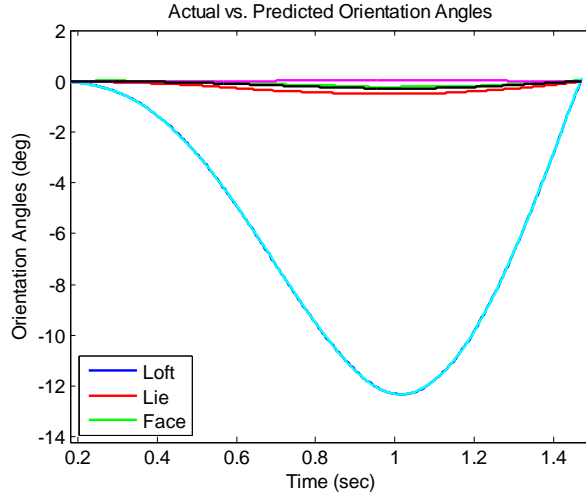
Figure 3.5: Measured and predicted orientation angles for a robot-generated PILS putting stroke. The blue, red and green curves are the measured loft, lie, and face angles, respectively. The cyan, magenta and black curves are the corresponding angles predicted by the simple, two-parameter kinematic model.

Having demonstrated good agreement between the predicted and measured orientation of the putter face, we now examine the putter path. Figure 3.6 shows the predicted putter path (cyan curve) and the calculated putter path (backswing = blue curve; forward swing = red curve). Notice that the measured path is very nearly straight (as predicted by the model) and that displacements along the lab-fixed "X" axis are greatly enlarged due to the refined vertical scale used in this figure (scale units of 0.1 *in*). The results shown in the Fig. 3.6(a) are uncorrected for the small misalignment of the sensor axes relative to the rotation axis of the putting robot. This misalignment derives from several sources including: 1) the imprecise manner of gripping the club, 2) any slight misalignment of the sensor axes relative to the grip, and 3) the machining tolerances controlling the placement and orientation of the bearings supporting the robot shaft. Figure 3.6(b) shows the data corrected for misalignment, using a correction of -1.6°. This correction is computed from

$$\theta_{mis} = \tan^{-1}\left(\frac{X_{f\_meas}(t_b) - X_{f\_model}(t_b)}{Y_{f\_meas}(t_b)} \right)$$

$$X_{f\_corr} = X_{f\_meas} - Y_{f\_meas} \tan\theta_{mis}$$

(3.3.1)

where t_b denotes the time at the end of the backswing and $\left(X_f, Y_f \right)$ are the

$\left(\hat{I}, \hat{J} \right)$ Cartesian coordinates of clubface centroid, point f.
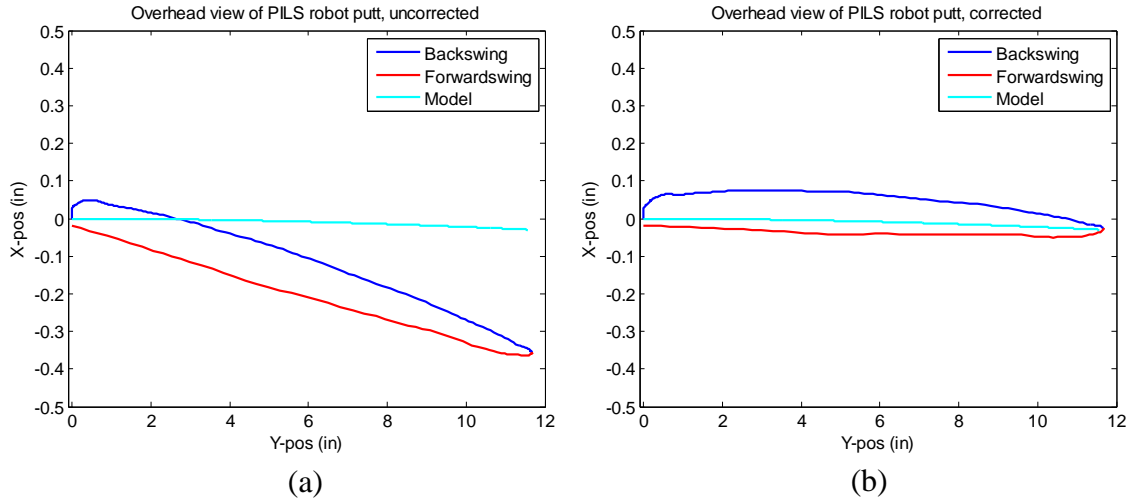
Figure 3.6: Measured and predicted path for the center of the putter head during a robot-controlled PILS putting stroke. (a) Uncorrected for slight misalignment of sensor axes to the robot rotation axis. (b) Corrected for this slight misalignment.

The measured putter path, once corrected for slight sensor misalignment, is shown Fig. 3.6(b) and it encircles the path predicted by the model. In particular, the measured path lies within 0.1 *in* of the predicted path with the greatest deviation occurring at the start of the backswing. This early "error" likely derives from clearance and compliance of the putting robot mechanism. During the backswing, the robot arm is pulled backwards from rest and any lateral clearance or compliance allows the putter head to move slightly along the lateral "X" axis. Overall, these tests of a nearly perfect PILS stroke by the robot demonstrate that the simple kinematic model accurately predicts the path and orientation of the putter throughout this stroke as expected.

The putting robot was then used to execute a nearly perfect gate strokes. To this end, the rotation axis of the robot was inclined approximately ten degrees using shims beneath the base of the robot. Using Eqns. (3.1.1)-(3.1.2), we compute the average $\Theta = 9.6^{\circ}$ (standard deviation 0.1°) and the average calculated $L_{arm} = 22.35$ *in* (standard deviation

1.14 *in*) based on six trials. (The larger standard deviation for these parameters relative to those for the PILS trials is a likely the result of small wobbling of the robot base on the added shims.)

Figure 3.7 reports the dynamic lie, loft and face angles for a representative gate stroke predicted by the two-parameter kinematic model and as measured by the sensor. As in the case of the PILS stroke, the dynamic loft predicted for the gate stroke is in near-perfect agreement with the measured loft. Similarly, the predicted dynamic face angle is in reasonably close agreement with the measurements. Unlike the PILS stroke where the face angle remained essentially zero, the gate stroke *requires* that the clubface open during the backswing (achieving a maximum of 2° for this modest example for which $\Theta \approx 10^o$) and then close back to square on the forward swing. This essential opening and then closing of the face angle during the putt is what many golf teachers and professionals identify as the key difference between the gate and PILS strokes. Here again, the largest discrepancy between the model and measurements occurs for the lie angle and it again is largely attributed to a slight and unknown misalignment of the sensor axes relative to the axis of rotation of the robot. This small discrepancy aside, these results demonstrate that one way to generate a gate stroke is to simply incline the axis of rotation. In the next section we will present further findings that suggest that most players exhibit a gate stroke developed in this very manner.
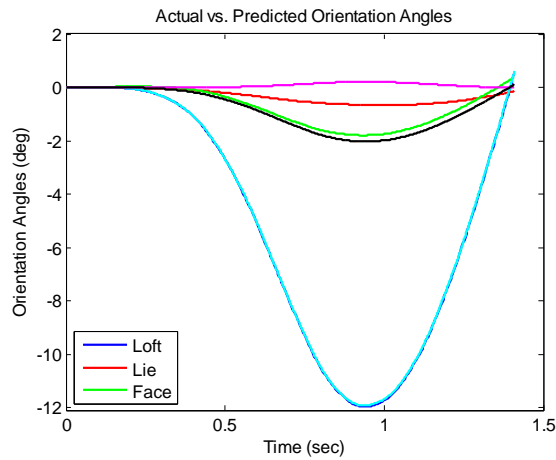
Figure 3.7: Measured and predicted orientation angles for a robot-generated gate stroke with $\Theta \approx 10^{\circ}$. The blue, red and green curves are the measured loft, lie, and face angles, respectively. The cyan, magenta and black curves are the corresponding angles predicted by the simple, two-parameter kinematic model.

The predicted and measured putter path for this example gate stroke is illustrated in Fig. 3.8. Figure 3.8(a) is not corrected for misalignment between the sensor and the robot, whereas Fig. 3.8(b) is corrected $\left(-2.92^{\circ}\right)$. The corrected measured path again encircles and closely follows that predicted by the simple kinematic model and with the small deviations attributable to robot clearance/compliance.
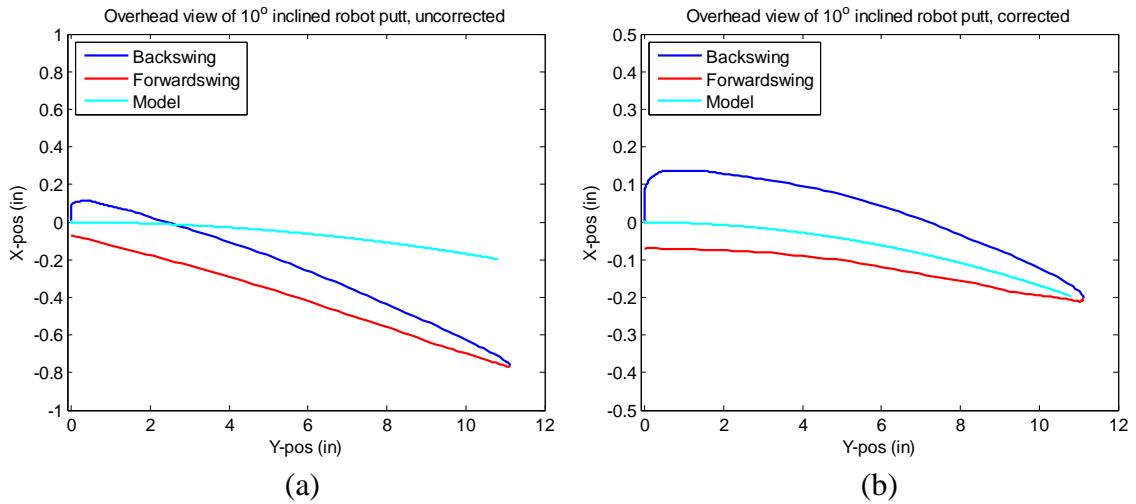
Figure 3.8: Measured and predicted path for the center of the putter head during a robot-controlled gate stroke with $\Theta \approx 10^{o}$. (a) Uncorrected for slight misalignment of sensor axes to the robot rotation axis. (b) Corrected for this slight misalignment.

Comparing the paths shown in Figs. 3.5 and 3.7 reveals that the gate stroke induces observable curvature to the path. The simple kinematic model clearly shows why. The actually 3-D path (of the center of the face of the putter) remains a circular path but now in a plane inclined from vertical by the angle Θ. The projection of this 3-D path onto the horizontal (X-Y) plane leads to the illustrated curved arc whose curvature is proportional to Θ. Thus, for larger Θ, as will be seen in many player putts, this curvature may be substantially greater than the modest example illustrated by this gate stroke by the putting robot. By contrast, the putter path remains a straight line in the horizontal (X-Y) for an ideal PILS stroke.

Overall, the results presented in this section demonstrate that the proposed two-parameter kinematic model accurately describes the idealized PILS and gate strokes performed by the putting robot. In the next section, we turn our attention to applying this model to the measured putting strokes from players of various skill levels.

3.4 Evaluation of Human Putting Strokes Using Kinematic Model

It was expected that the two-parameter kinematic model of putting agree well with measured putts using the putting robot since the robot is a single degree-of-freedom mechanism for which L_{arm} and Θ remain constant. The major finding within this section is that this simple model remains a very good approximation for players who naturally move free of the constraints of the putting robot. We shall begin by first introducing quantifiable metrics for comparing measured putting strokes to the model.

Metrics for Comparing Measured Putting Strokes to Model

Return to Fig. 3.2 and recall that the two-parameter kinematic model represents a single degree-of-freedom system allowing rotation about the inclined axis denoted by $\widehat{I}^{'}$. Therefore, how well this model describes player putting rests in part on how closely player putting can be described by rotation about a fixed (inclined) axis. To quantify this idea, we propose the following metrics which describe the degree to which the measured angular velocity of the club is aligned with a constant axis of rotation inclined by an estimated angle Θ. Let the club angular velocity vector be represented as

$$\vec{\Omega} = \Omega_x \hat{I} + \Omega_y \hat{J} + \Omega_z \hat{K} \tag{3.4.1}$$

where $(\hat{I}, \hat{J}, \hat{K})$ is the lab-based frame; refer to Fig. 3.2. Next, let Θ_{ave} represent the average value of Θ computed using Eq. (3.2.1) for all times t for which $|\vec{\Omega}|$ is greater than some reasonably small value, say 5 deg/sec. For slower angular velocities, the putter is essentially at rest. Next we introduce the following three error measures that describe the deviation of the measured angular velocity vector from one aligned with the rotation axis defined by Θ_{ave}.

$$\Omega_{x\_err}(t) = \frac{\left|\vec{\Omega}(t)\right|\cos\Theta_{ave} - \Omega_x(t)}{\left|\vec{\Omega}(t)\right|} \quad \text{for} \quad \left|\vec{\Omega}(t)\right| > 5\frac{\deg}{s}$$

$$\Omega_{y\_err}(t) = \frac{\Omega_y(t)}{\left|\vec{\Omega}(t)\right|} \quad \text{for} \quad \left|\vec{\Omega}(t)\right| > 5\frac{\deg}{s} \qquad (3.4.2)$$

$$\Omega_{z\_err}(t) = \frac{\left|\vec{\Omega}(t)\right|\sin\Theta_{ave} - \Omega_z(t)}{\left|\vec{\Omega}(t)\right|} \quad \text{for} \quad \left|\vec{\Omega}(t)\right| > 5\frac{\deg}{s}$$

If these error metrics remain small, then the putter is indeed rotating largely about a fixed axis as determined by the computed angle Θ_{ave}.

The two-parameter kinematic model also assumes that the distance L_{arm} remains constant thereby determining the length of an equivalent 'pendulum' from the sensor module to the axis of rotation; refer again to Fig. 3.2. We estimate L_{arm} by computing its average from Eqn. (3.2.2) using computed values of $Y_{grip}(t)$ and $\Phi(t)$ from the sensor data. We then compute the predicted club rotation Φ_{model} from the simple kinematic model by again using Eqn. (3.2.2) with the average value of L_{arm}. The actual club rotation $\Phi_{meas}(t)$ can be computed directly from the sensor data according to

$$\Phi_{meas}(t) = \int_0^t \left(\vec{\Omega}\cdot\hat{I}\right)dt \qquad (3.4.3)$$

using $\Phi_{meas}(0) = 0$ at address. The error between the measured rotation and that predicted by the model

$$\Phi_{err}(t) = \frac{\Phi_{model}(t) - \Phi_{meas}(t)}{\Phi_{meas}(t)} \quad \text{for} \quad \left|\vec{\Omega}\right| > 5\frac{\deg}{s}$$

$$\Phi_{model} = \sin^{-1}\left(\frac{1}{L_{arm}}Y_{grip}\right) \qquad (3.4.4)$$

yields a fourth criterion for comparing a player putt to the simple kinematic model. These four criteria will now be applied to player putts to assess how well these putts conform to the assumptions of the simple kinematic model.

Analysis of Player Putts

The putts presented in this section are examples selected from putting trials conducted over the past three years involving more than ten subjects putting in various conditions; from putts in the laboratory, to putts on artificial putting surfaces, to putts on actual putting greens.

We begin by analyzing an example putt from a study conducted at the University of Michigan golf course. In this study, we selected two (approximately straight and level) putts of 15 ft and 5 ft and requested each subject to complete three putts at both distances. The example 15 ft putt illustrated in Fig. 3.9 was completed a collegiate-level competitive player. Illustrated are the orientation and putter path measured by the sensor and predicted by the (best-fit) kinematic model.
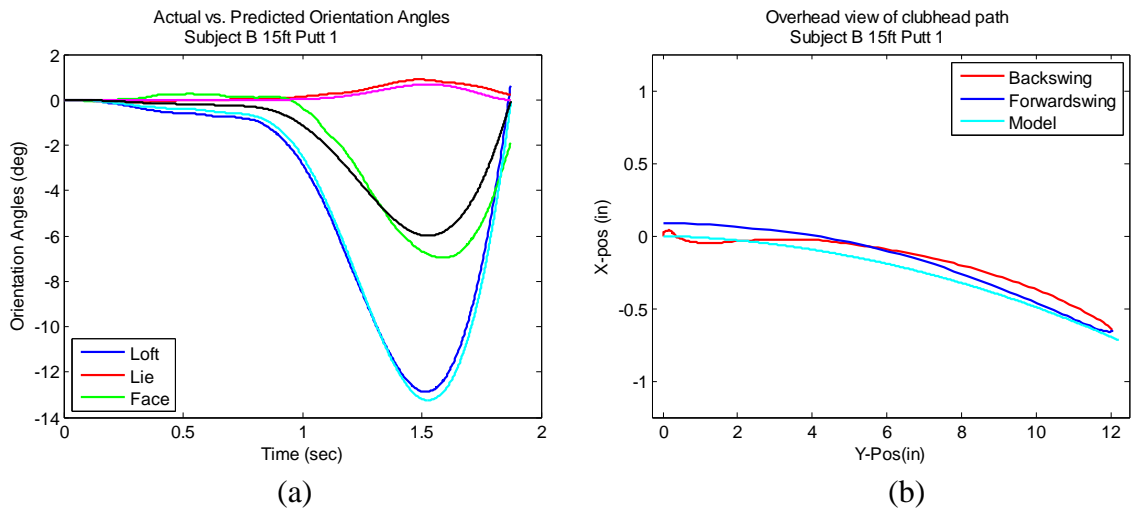
Figure 3.9: Example 15 ft putt by subject B showing excellent agreement between measured and modeled putter kinematics. (a) shows the measured and predicted club head lie, loft and face angles as functions of time (blue, red, green = measured; cyan, magenta, black = model prediction). (b) shows the path traced by the center of the clubface in the horizontal (X-Y) plane.

The measured features illustrated in Fig. 3.9 are in excellent agreement with the model predictions. In Fig. 3.9(a), the measured dynamic loft (blue curve) and lie (red curve) angles closely follow the predicted angles (cyan and magenta, respectively). The

measured face angle (green) also follows a very similar trend to the predicted angle (black), which shows the clubface opening during the backswing and closing during the forward swing. In Fig. 3.9(b), the predicted path (cyan) is closely traced by the measured clubface path (blue = backswing, red = forward swing); again, note the greatly magnified scale on the vertical axis. This example putt exhibits the main characteristics of a gate stroke; 1) face opens during the backswing and closes during the forward swing, and 2) the projection of the putter path onto the horizontal plane is distinctly curved. The overall close agreement with the model prediction is strong evidence that the model kinematics closely approximate actual putting kinematics for this subject. Figure 3.10 presents another view of the same data that allows direct estimation of the model parameters and (visual) comparison of the error metrics established by Eqns. (3.4.2) and (3.4.4).
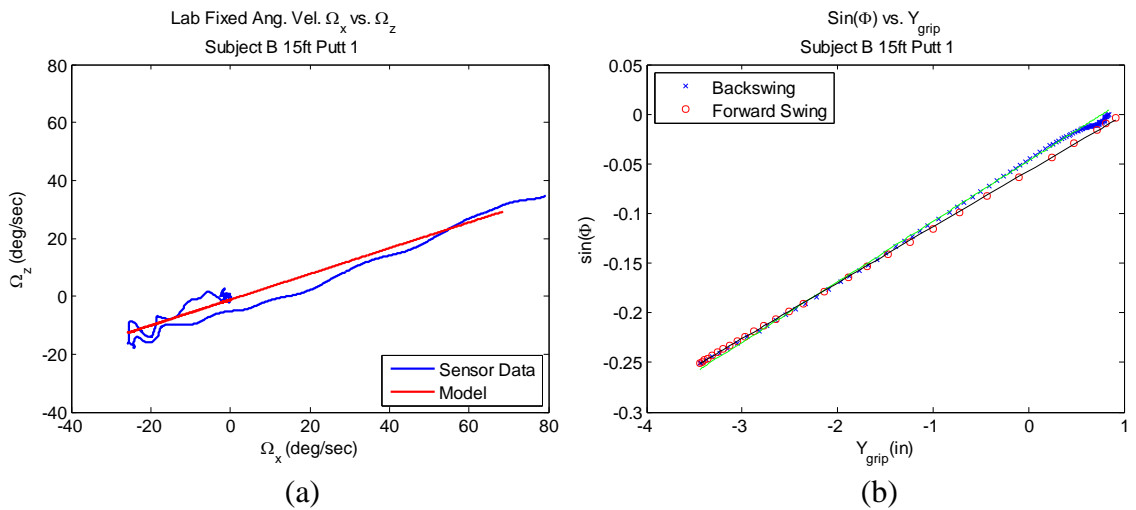
Figure 3.10: Example 15 ft putt by subject B showing excellent agreement between measured and predicted putting kinematics. (a) shows the measured relationship between the angular velocity components Ω_x and Ω_z together with that predicted by the simple model. (b) shows the measured relationship between the rotation angle Φ and the grip position coordinate Y_{grip}. The measured points are plotted for the backswing and forward swing. The best fit model predicts the green and black lines for the backswing and forward swing, respectively.

Figure 3.10(a) reports the (lab-fixed) angular velocity component Ω_z versus the component Ω_x. The experimental data are plotted with the blue dashed line and the solid

red line is the best fit line to this data. The slope of this trend line is used to estimate the model parameter Θ_{ave}, which is equivalent to averaging Eqn. (3.2.1) for all times t. In this example, the results of the model closely approximate the experimental data. Figure 3.10(b) reports $\sin(\Phi_{meas})$ versus Y_{grip} where Φ_{meas} is calculated via Eqn. (3.4.3). Data points for the backswing are plotted in blue and those for the forward swing are plotted in red. Separate linear trend lines are fit to the back and forward swings. After reviewing the putts from numerous subjects, it became apparent that most putts exhibit two distinct trend lines when viewed as illustrated in Fig. 3.10(b). Per Eqn. (3.1.2), the inverse of the slope of a trend line in this figure provides an estimate for the model parameter L_{arm}. Thus, one can compute an effective L_{arm} for the backswing which is often distinct from that computed for the forward swing. In the next section, we will further discuss how a measurable change in L_{arm} from the backswing to the forward swing represents a common putting fault. In this example, however, the two trends lines lie nearly on top of each other indicating that a single value of $L_{arm} = 17.1 in$ for the model closely approximates the kinematics of both the back and forward swings. For completeness, we report in Fig. 3.11 the error metrics defined by Eqns. (3.4.2) and (3.4.4).
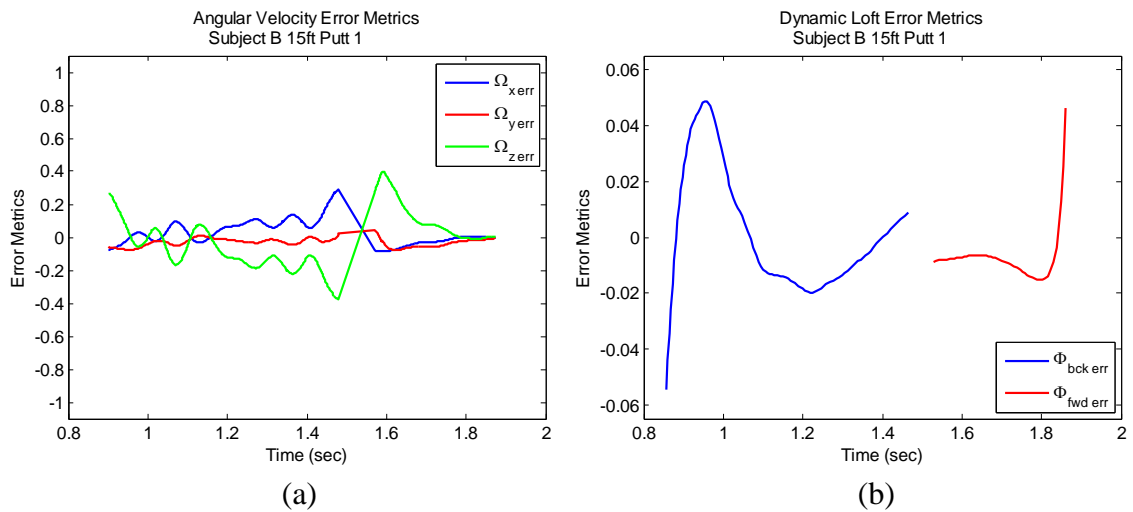
Figure 3.11: Error metrics defined by Eqns. (3.4.2) and (3.4.4) for example 15 ft putt by subject B. (a) The three angular velocity error metrics. (b) Dynamic loft error metrics for the backswing and forward swing.

The results of Fig. 3.11 demonstrate that the error metrics remain reasonably small throughout the putt. The jumps in the data in Fig. 3.11(a) at approximately 1.45s and 1.60s and the gap in the data of Fig. 3.11(b) occur at the end of the backswing and the start of the forward swing where the angular velocity remains less than the threshold (5 deg/s). The time averages of these five metrics are reported in Table 3.1. These average errors remain less than 5% indicating a superb overall fit to the assumptions of the simple kinematic model.

Subject B 15ft Putt 1	Ω_{x_err} (%)	Ω_{y_err} (%)	Ω_{z_err} (%)	Φ_{bck_err} (%)	Φ_{fwd_err} (%)
Average	4.54	4.00	-2.21	0.16	1.38
STD	13.99	3.24	20.09	2.28	8.37

Table 3.1: Average errors between predicted and measured putt kinematics for the example 15 ft putt for subject B.

As a second example, a putt from a different collegiate-level player is presented next that illustrates one of the more extreme cases where larger errors develop. This example putt is taken from trials conducted with players from the University of Michigan Women's

Golf Team. During these trials, three subjects completed 5 putts from 4 ft, 10 putts from 8 ft, and 10 putts from 15 ft. The example chosen is one 8 ft putt from subject L.
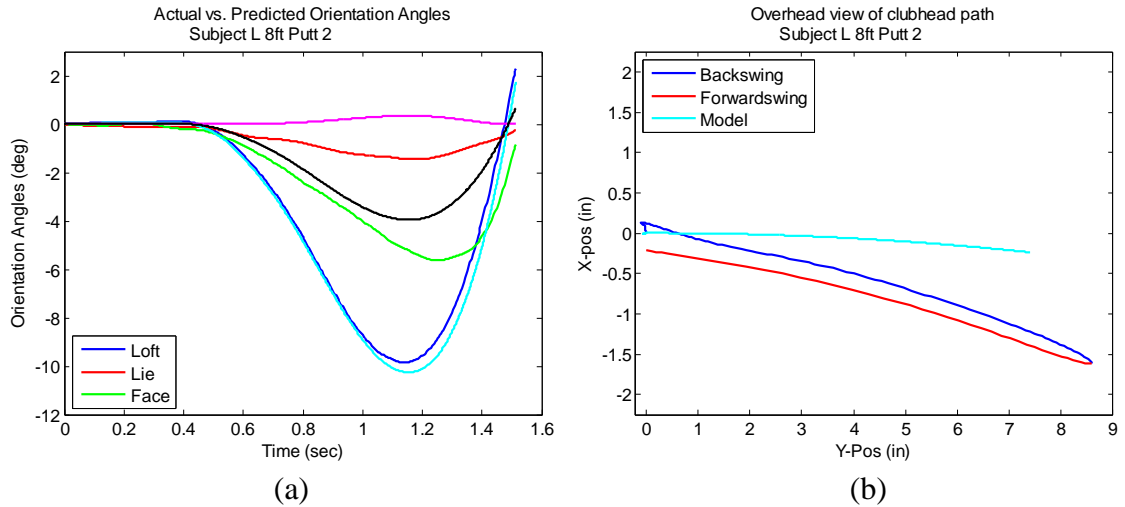
Figure 3.12: Example 8 ft putt by subject L showing more discrepancy between measured and modeled putt kinematics. (a) shows the measured and predicted club head lie, loft and face angles as functions of time (blue, red, green = measured, cyan, magenta, black = model predictions). (b) shows the path traced by the center of the face of the club head in the horizontal (X-Y) plane.

From Fig. 3.12(a), note that the measured (blue) and predicted (cyan) loft angles match well indicating that this stroke conforms to a major prediction of the simple kinematic model. The face angles show a very similar trend but the lie angles show opposite trends. A further comparison is provided in Fig. 3.13.
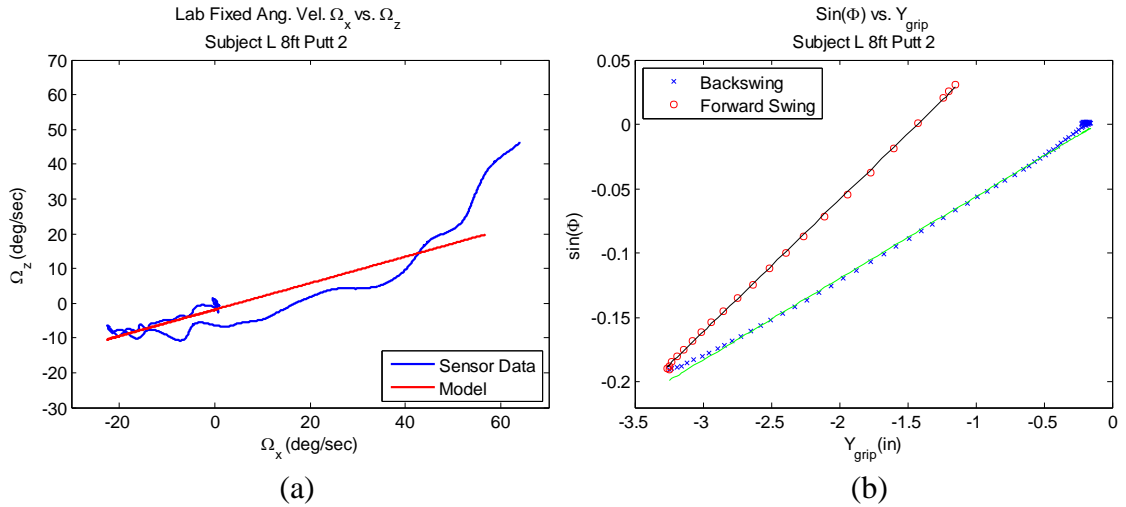
Figure 3.13: Example 8 ft putt by subject L exhibiting less agreement with the simple kinematic model. (a) shows the measured relationship between the angular velocity components Ω_x and Ω_z together with that predicted by the simple model. (b) shows the measured relationship between the rotation angle Φ and the grip position coordinate Y_{grip}. The measured points are plotted for the backswing and forward swing. The best fit model predicts the green and black lines for the backswing and forward swing, respectively.

In Fig. 3.13(a) the measured angular velocity component increasingly deviates from the model trend (red) for $\Omega_x > 40$ deg/sec, which occurs towards the end of the forward swing. Fig. 3.13(b) now clearly shows two distinct trend lines for the backswing and the forward swing, indicating distinct values for L_{arm} for these parts of the putting stroke. The abrupt change in L_{arm} occurs at the transition from the back to the forward swing, an issue that is discussed in the next section on common putting faults.
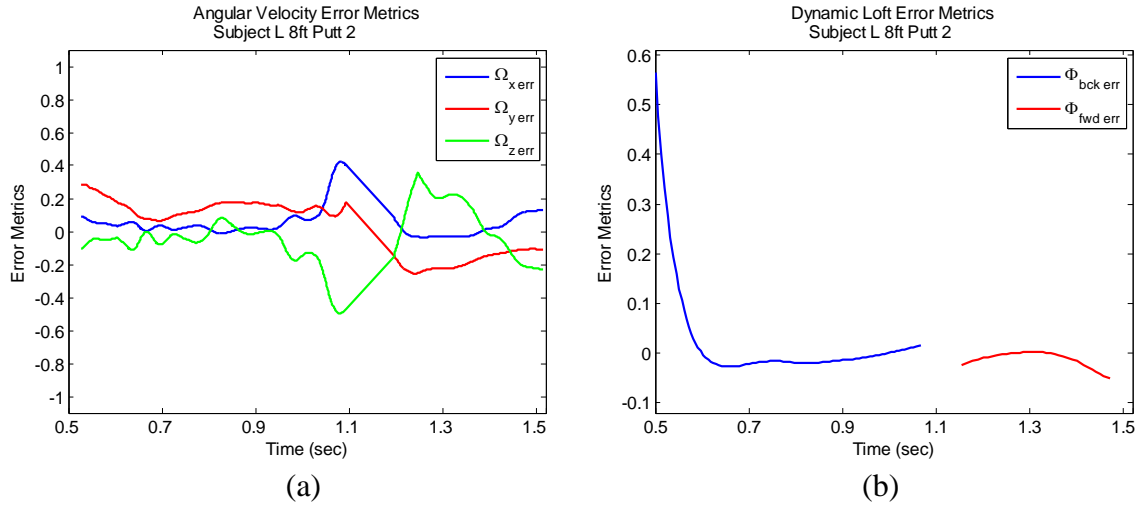
Figure 3.14: Error metrics defined by Eqns. (3.4.2) and (3.4.4) for an 8 ft putt by subject L. (a) Angular velocity error metrics. (b) Dynamic loft error metrics for the backswing and forward swing using distinct values for L_{arm}.

Figure 3.14 illustrates the time histories of the five error metrics for this example putt and the time averages of these error metrics are reported in Table 3.2. Overall, the errors (ranging from 3%-17%) are approximately twice as large as in the last example and they are also on the extreme side of all measurements taken on elite golfers. Nevertheless, the model still appears to predict the kinematics of the putt with reasonably good fidelity (to within 20%).

Subject L 8ft Putt 2	Ave Ω_{x_err} (%)	Ave Ω_{y_err} (%)	Ave Ω_{z_err} (%)	Ave Φ_{bck_err} (%)	Ave Φ_{fwd_err} (%)
Average	9.06	16.48	-8.05	2.78	-2.85
STD	16.25	6.23	20.02	10.98	5.26

Table 3.2: Average errors between predicted and measured putt kinematics for the example 8 ft putt for subject L.

Simple Kinematic Model Correlation Errors for 10 Subjects					
Subject	Ave Ω_{x_err} (%)	Ave Ω_{y_err} (%)	Ave Ω_{z_err} (%)	Ave Φ_{bck_err} (%)	Ave Φ_{fwd_err} (%)
J	1.92	5.45	-1.67	0.20	-3.14
B	3.77	4.59	-2.78	-2.61	5.78
R	8.07	5.67	-5.24	-0.12	-1.04
L	9.02	14.33	13.45	2.00	4.33
A	3.44	5.19	-12.81	5.71	0.64
KK	0.10	5.95	1.51	4.34	-6.73
JK	-0.24	12.56	3.50	2.28	0.03
K	8.01	7.51	-6.7	-12.04	-3.21
T	8.16	10.04	-6.14	2.56	-5.98
BT	10.17	27.85	0.90	9.04	-1.36
Overall	5.24	9.91	-1.60	1.14	-1.07

Table 3.3: Average error metrics for all (120) trials conducted on a total of 10 subjects.

Table 3.3 reports the compilation of errors metrics for a total of 120 trials conducted on a total of 10 subjects. For each subject, the average error metrics over all measured putts is reported to establish the overall fit of the kinematic model to that player. The subjects are arranged by skill level, with the first five subjects having played collegiate-level competitive golf and the last two subjects having just been introduced to the game. Over all of these trials, the overall average error metrics (bottom row) confirm that the simple kinematic model remains accurate to within approximately 10%. This new and fundamental understanding of the putting stroke as viewed using the simple kinematic model might have significant diagnostic value in player assessment and training.

3.5 Identification of Common Putting Faults

Having shown that human putting strokes are reasonably well predicted by the simple kinematic model, we will now examine the sources of deviations from that model. The model discussed thus far focuses on the kinematics of the putting strokes. In addition, one may also consider the forces and moments developed by the player at the grip that 'drive' the putting strokes. These forces and moments are often loosely referred to as the "power source" of a putt in popular descriptions of the game. To aid our discussion of putting techniques, we first comment on the power sources.

The 'power' used during the putting stroke may derive from two principal sources; namely, skeletal muscles and gravity. Notable teachers, Pelz [41], Utley [45], and Craig [46], advocate that the muscles across the shoulder joints should be the main skeletal muscles recruited in putting while the elbow and wrist joints should remain essentially locked. The shoulder muscles are used in the backswing to draw the club backwards opposite the target line and upwards against gravity. The experts concur that the forward swing should be powered by gravity alone. Under these circumstances the forward swing kinematics reduce to that of a gravity-driven pendulum allowing rotation about a (possibly inclined) fixed axis. Similarly, the club and the player's arms form a rigid body pendulum. In cases of very long putts and/or very slow greens, it may become kinematically impossible for players to develop the very long backswing required to power the forward swing by gravity alone. In such instances, players will actively recruit muscles to provide the requisite additional power.

With this basic understand of putting dynamics we move forward to the second goal of this chapter, to demonstrate how the MEMS sensor technology yields a novel tool for the analysis of putting technique. Specifically, we will demonstrate how the sensor can measure common faults in putting technique.

Most coaches would concur that faults in putting technique trace to one or more of the following principal sources:

- Improper face angle at impact
- Off-center impact of the ball on the clubface (related to putter path)
- Improper use of wrist
- Improper hand position relative to the club head at impact

These are common faults specifically associated with the putting strokes (back and forward swing) and they are distinguished from any additional "faults" due to improperly aligning the putt and/or improperly reading the green. We shall explore each of these principal sources in turn and provide experimental data to support our claim that the MEMS sensor technology can identify faults in the putting stroke.

Improper Face Angle at Impact

The face angle at impact is the single most critical parameter affecting the outcome of the putt. According to Pelz [41], an improper face angle at impact adversely affects the putt four times more than an improper path of the putter alone. For example, consider a straight 10 ft putt with the initial target line directed exactly to the center of the hole. A mere one degree open or closed face angle at impact will cause the ball to miss the hole. It is therefore imperative to measure and to understand how the face angle changes during the putting strokes in order to detect the root cause of this most common putting fault. A very effective way to view how errors in the face angle develop is to plot the face angle as a function of position during the back and forward swings as illustrated next.
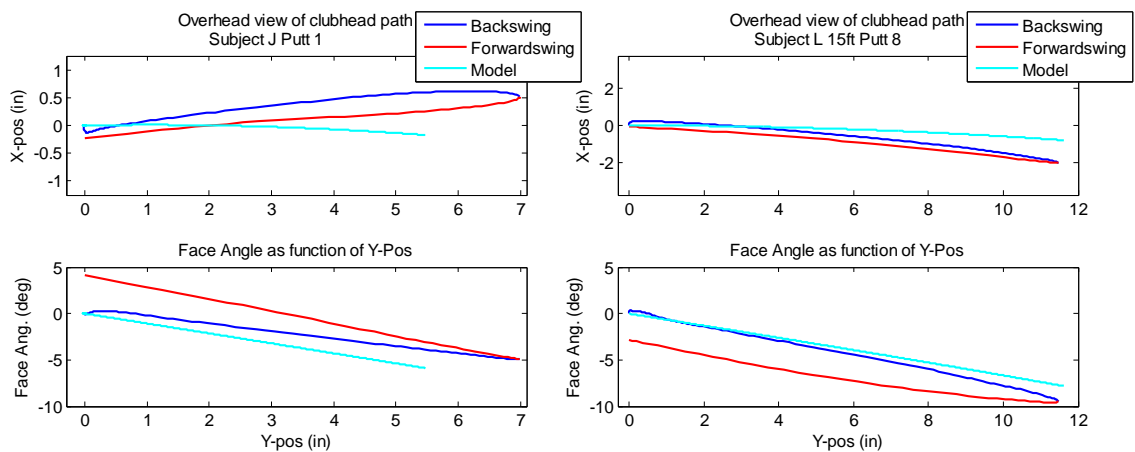
Figure 3.15:   Two example putts illustrating different faults leading to excessive face angles at impact. Top figures illustrate the measured path of the club head (and ball impact location) as viewed in the horizontal (X-Y plane). Bottom figures illustrate the measured face angle as a function of position (Y coordinate of club head) in the stroke. The example to the left illustrates significantly different closure rates (deg/in) on the forward versus backswings. The example to the right illustrates a period of near-zero rotation at the start of the forward swing.

Figure 3.15 presents two example putts having distinct root causes for excessive face angles at impact. The two bottom figures plot the face angle as a function of position within the stroke (as determined by the Y-coordinate of the club head) for both the back (blue) and forward (red) swings. Also shown is the predicted relation using the simple

kinematic model (cyan). The top portions of the figures show the measured path of the club head as viewed in the horizontal (X-Y) plane which is discussed further below.

From the bottom left figure, notice that the clubface opens at a slower rate during the backswing than the model predicts and then closes at a rate approximately equal to that of the model on the forward swing. (These face angle rates are measured in degrees per inch of displacement along target line.) Our measurements of over 100 trials from 10 subjects reveal that face angle faults frequently derive from different face angle rates for the back and forwards swings. This type of measurement is extremely difficult to make using existing camera-based systems and thus such diagnoses have not been readily available for player feedback/training. Second, the simple kinematic model suggests an expected or 'target' face angle rate that further discriminates the root cause problem of the putting fault.

For the example putt on the right, the backswing has a well-defined face angle rate that closely matches the target rate predicted by the model. By contrast, the face angle rate for the forward swing matches that of the backswing (and model) only for the last two-thirds of the forward swing extending from approximately $8 > Y > 0$ in. For the first one-third of the forward swing, extending from approximately $11.5 > Y > 8$ in, the face angle rate is considerably less and ultimately leads to a net open face angle at impact of about 3°. Again, this analysis pin-points the root cause of the putting fault which in this case is a slow face angle rate at the very start of the forward swing.

Off-Center Impact

The location of impact between the ball and the clubface is the second most important condition that determines ball dynamics following impact. Off-center impacts produce less momentum transfer to the ball and may also allow the ball to diverge from the intended target line due to sudden, inadvertent changes to the face angle. For example, impacts towards the heel (conversely the toe) of the club may allow the ball to veer left (conversely veer right) of the intended target line. To investigate where ball/head impact occurs, we now examine the final position of the club head from the measured club head path. In doing so, we tacitly assume that the player has centered the ball on the clubface at address (which is also part of our testing protocol).

The impact locations for the two prior example putts illustrated in Fig. 3.15 can be deduced by inspection of the club head paths in the top figures. For the example shown to the left, the impact occurs towards the toe (hence the center of the clubface finishes with $X < 0$ in this example) by approximately $X = -0.3$ in. Notice further that the club head remains largely "outside" (i.e., on the far side of) the target line $X = 0$ and remains there until just before impact. The proper path for both the ideal PILS and gate strokes with positive Θ is one that remains "even" with or "inside" the target line. Only in the seldom seen style where $\Theta < 0$ would the putter path be expected to lie outside the target line. In this example, $\Theta > 0$ and therefore the putter path would be expected to be inside the target line. The club head path predicted by the simple kinematic model provides a possible target for the correct path for this subject.

By contrast, for the example shown on the right, the club head at impact finishes nearly exactly at the same position where it began ($X = 0$ in) and thus this impact location is essentially perfect. Although this putt achieves proper impact location, the putter path for remains largely inside the predicted path.

Improper Use of Wrists

Many players unlock or "hinge" their wrists during the putting stroke which violates the advice of experts as well as the constraints of the simple kinematic model. As mentioned above, the experts concur that the putting stroke derives principally from rotation about the shoulder joints keeping the elbow and wrist joints locked. The sensor technology provides a quick means to detect inadvertent joint rotations.

For example, the results shown in Fig. 3.16(a) illustrate a putt having a distinctly smaller value for L_{arm} during the forward swing (9.2 in) compared to that (14.7 in) for the backswing. As a result, the player's hands "lag" behind the club head during the forward swing and create a final putter loft angle at impact that is about 3° greater than that at address. This change in L_{arm} and the resulting 'lag' of the hands are measureable putting faults. In the previous section, we noted that many player putts exhibit this type of change in L_{arm}. In nearly all examples observed to date (as in the example of Fig. 3.16), the change occurs precisely at the transition from the backswing to the forward swing. One possible explanation for this abrupt change is that the player allows his/her wrists to 'break' or 'hinge' at this transition. That makes sense considering that the putter achieves its greatest angular acceleration at this transition and thus the reaction moment on the wrists also achieves a maximum.

The example results illustrated in Fig. 3.16(b) represents an exaggerate putt intentionally executed using only wrist rotation. The exceedingly small values for L_{arm} (4.7 and 3.6 in) measured for this putt confirm that the axis of rotation is uncharacteristically close to the top of the grip due to rotation largely about the wrist joints. This limiting case confirms that any rotation about the wrist during normal putting will indeed decrease L_{arm} as observed at the start of the forward swing in the example to the left. The ability to identify if and where a player allows their wrists to break is a powerful aid in diagnosing this common putting fault.
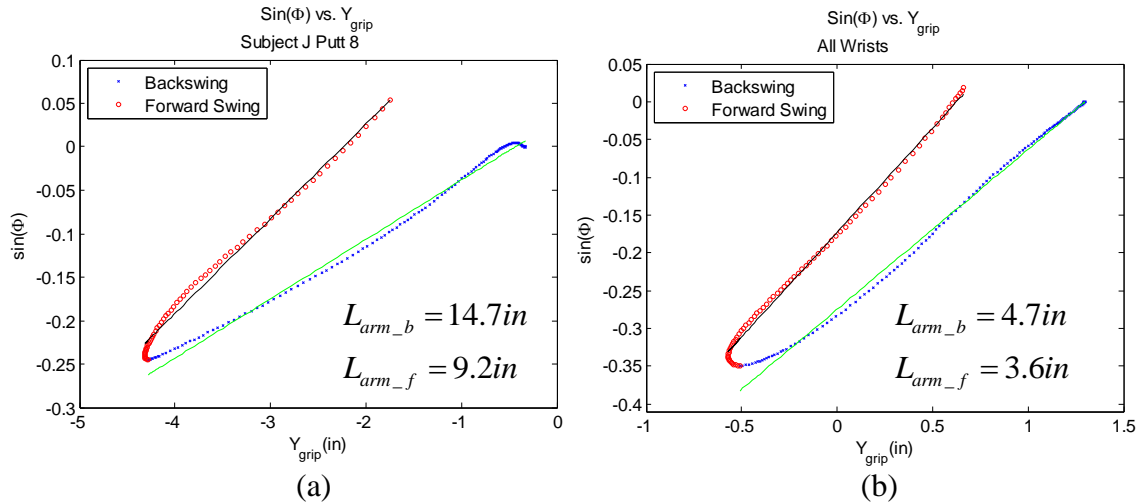
Figure 3.16: (a) example showing wrist-break at the end of the backswing. (b) example is an exaggerated putt using only wrists and leading to very small values for L_{arm} as a result.

Improper Hand Position Relative to Club Head

It is also well-understood that putting faults arise from the improper positioning of the player's hands (grip) relative to the club head during the back and/or forward swings. Ideally, the grip should be approximately even with the clubface at impact to obtain the proper loft at impact. When the clubface is forward of the hands at impact, the loft at impact is greater than the pre-set loft designed for the putter. Too much loft keeps the ball in flight too long, which contributes to poor ball tracking along the target line. Conversely, when the clubface is too far behind the hands at impact, the loft at impact is smaller than the pre-set loft design for the putter. Too little loft causes the ball to impact the ground too quickly (and possibly re-bound) which again leads to poor ball tracking.

Data for two putts illustrated below demonstrate both of these faults; namely 1) a case where the hands excessively lead the club head at impact, and 2) a case where the hands excessively lag the club head at impact. Careful analysis of the data pin-points exactly where these faults arise in these examples.
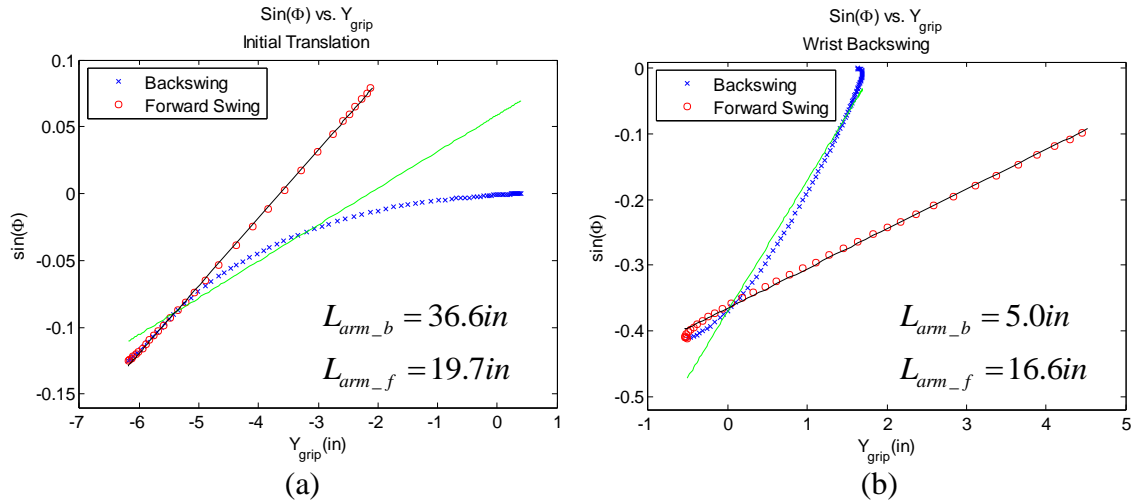
Figure 3.17: Loft angle ($\sin\Phi$) versus grip position along target line (Y_{grip}). Example (a) demonstrates how the grip can lag the club head at impact leading to excessive loft at impact. Example (b) demonstrates how grip can lead the club head at impact leading to insufficient loft at impact. Both faults develop early on in the backswing.

The two example putts are illustrated by the results of Figs. 3.17-3.18. Figure 3.17 reports the measured change in $\sin(\Phi)$ as a function of grip position Y_{grip} during the backswing (blue) and forward swing (red) and as predicted by the simple kinematic model (green and black). Fig. 3.18 reports the positions (Y coordinates) of the hands/grip (green) and the club head (blue) for the same trials.

Starting with Fig. 3.17, notice that the forward swings (red) for both example putts largely conform to the predictions of the kinematic model (black). Thus, any faults deriving from improper hand position will largely develop during the backswings. For the example on the left in Fig. 3.17, the backswing begins with a substantial change in the grip position (Y_{grip}) but with little change in the loft angle ($\sin\Phi$). Thus, the player begins this backswing by *translating* the club backwards without a commensurate *rotation* of the club. As a result, the club head is drawn back at the start of the backswing by an amount nearly equal to that of the grip as clearly seen in the results of Fig. 3.18(a). The unusually large value for L_{arm} (36.6 in) computed for the backswing is consistent with the fact that backswing begins with translation and little rotation. (For the limiting case of pure translation $L_{arm} \to \infty$). The forward swing then proceeds as predicted by the

kinematic model and does not correct any of the error developed at the start of the backswing. As a result, the players hands substantially lag (-2 in) the club head at impact and the clubface has excessive loft.

By contrast, the example shown in Figs. 3.17(b) and 3.18(b) illustrate a putt for which the hands lead the head substantially (+4 in) at impact leading to insufficient loft. The root cause of this putting fault is a "wrist break" at the very start of the backswing. Notice from Fig. 3.17(b), that the backswing has an unusually small value (5.0 in) for L_{arm} which is consistent with a wrist break; recall results for the "all-wrist" putt illustrated in Fig. 3.16(b). By contrast, the forward swing is more typical of a gate stroke for which $L_{arm} = 16.7$ in and hence it does not exhibit a possible 'counter-correcting' wrist break. Thus, the player's hands remain considerable forward of the club head throughout the backswing and throughout the forward swing where they finish at impact with a large (4 in) lead over the club head. This putt, while rather different from the example on the left, reinforces the same conclusion; namely, the backswing failed to follow the kinematics of the simple pendulum model where club motion develops solely through shoulder rotation.

(a)   (b)
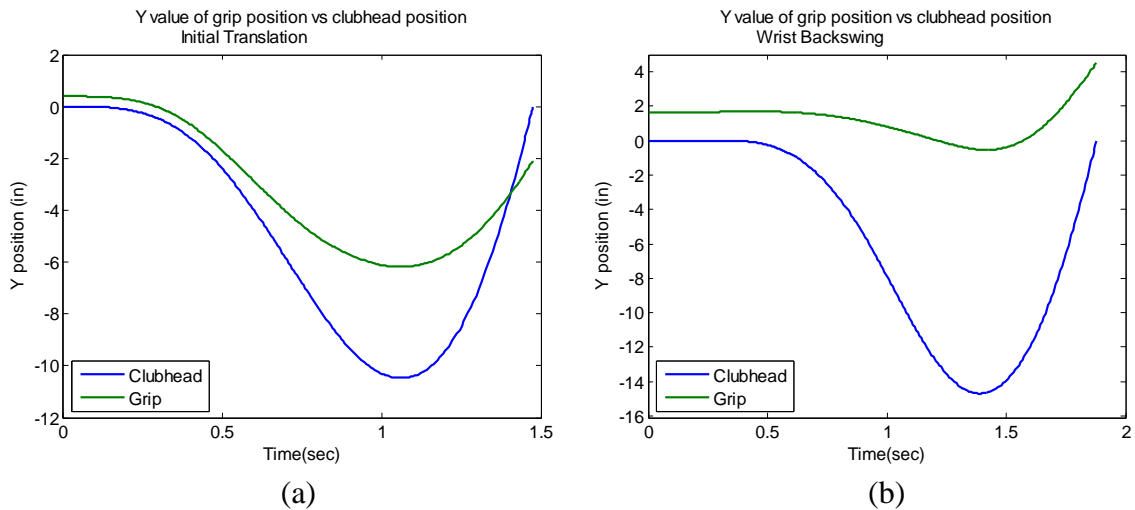
Figure 3.18: Position of club head versus grip. Example (a) demonstrates how the grip can lag the club head at impact. Example (b) demonstrates how the grip can lead the club head at impact. Both faults develop early on in the backswing.

3.6 Closure

This chapter advances our fundamental knowledge of putting strokes by exploiting measured putting kinematics provided by the MEMS sensor system. In addition, this chapter introduces a unified kinematic model for putting that encompasses the previous "pendulum style" and "gate style" strokes discussed in the literature; see, for example, [41]. Finally, this chapter introduces a suite of putting metrics that can pin-point common putting faults. In total, this measurement and analysis system provides significant and new capabilities for putting instruction.

The simple kinematic model for putting reduces to a single-degree of freedom pendulum with two parameters Θ and L_{arm} determined by the player's preferred putting style. The parameter Θ defines the (average) inclination of the axis of rotation of the pendulum and the parameter L_{arm} defines the distance from the axis of rotation to the grip. Both Θ and L_{arm} are computed from measured sensor data. Doing so yields a reasonably accurate prediction of the club head orientation (lie, loft and face angles) for both the back and forward swings. Comparison of the measured versus the predicted club head orientation yields considerable insight into the root causes of principal putting faults including the most common fault, namely an improper face angle at impact.

In using the kinematic model, we often observe that the forward swing and backswing yield distinct values of the parameter L_{arm}. In particular, abrupt changes in L_{arm} reveal that the player has 'broken' otherwise 'locked' wrists during the stroke which leads to a second major putting fault. This improper use of the wrists can produce excessively large or excessively small loft angles at impact. Upon adding distinct values for L_{arm} for the forward and backswings, the simple kinematic model remains in good agreement with measured kinematics.

The last section of this chapter introduces example metrics derived from the sensor data that pin-point common putting faults. By studying numerous putts from many subjects, it

became apparent that putting errors most often originate at the beginning of the backswing or at the transition between the back and forward swings. A fundamental reason for this is that these points represent the periods of greatest angular acceleration, hence greatest reaction moments at the wrists.

CHAPTER 4

**EXTENSION OF MEMS INERTIAL SENSOR SYSTEM
TO HIGHLY DYNAMIC GOLF SWINGS**

The objective of this chapter is to extend the measurement theory and hardware design developed in Chapter 2 for putters to the measurement of highly dynamic golf swings that arise with drivers and irons. The immediate objective is to measure the *rigid body motion* of the golf club during what we refer to as a 'full swing'. The additional flexible motion of the club, which may be induced by sizable rigid body accelerations, is discussed in both Chapters 5 and 6. Representative results of full swing measurements and analyses will be presented to demonstrate the successful application of this technology for drivers and irons. We open by first reviewing the requirements for the sensors to support this new range of measurements.

4.1 Sensor Requirements for Full swings

During a full swing as illustrated in Fig. 4.1, the golf club achieves significantly larger acceleration and angular velocity than in putting. Therefore the sensor system of Chapter 2, that was optimized to resolve the putting stroke, is ill-suited to resolve a full swing. A design capable of measuring the full swing requires sensors that can accurately resolve angular velocity upwards of 2000 deg/sec and accelerations (at the grip) in the range of 10-15 g. These rates follow from the observable fact that the golf club travels from the top of the backswing (shaft at the 3 o'clock position in Fig. 4.1) to the impact position (shaft at the 6 o'clock position in Fig. 4.1) within a mere 0.2 to 0.3 seconds [15].
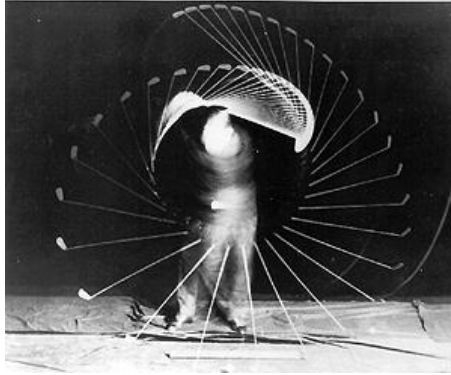
Figure 4.1: Stroboscopic photograph of Bobby Jones' golf swing which illustrates a full swing (downswing phase and follow through). [47]

Based on these high ranges a second-generation of the design described in Chapter 2 (refer to Fig. 2.4) was created with rate gyros capable of measuring up to 3000 deg/sec and a tri-axis accelerometer with a ± 15 g dynamic range. No additional hardware changes where required for this second-generation design. In particular, the first-generation design, which sampled the sensors at 1 kHz, still provides 200-300 samples during highly dynamic downswings. The measurement and analysis of full swings using this second-generation "high-range" MEMS sensor is the focus for the remainder of the chapter.

4.2 Measurement of Full Swings

Low Speed Swings Using Putting Robot

In Chapter 2, a simple putting robot was introduced that swings a golf club on a pendulum path under the action of gravity alone. The putting strokes considered were low speed and with loft ranges consistent with putting. We used this robot to establish that the first-generation sensor system accurately measures the orientation and position of the clubface. Chapter 3 then introduced a two-parameter kinematic model of the putting stroke that was shown to predict the putts executed with the robot to a high degree of accuracy. We now employ the robot and the two-parameter kinematic model to establish the accuracy of the second-generation sensor for 'exaggerated' pendulum style strokes near the kinematic limits of the robot. These strokes, which induce club head speeds two

to three times those of typical putting strokes, are still substantially slower than full swings as reported later.

Figures 4.2 and 4.3 present the results obtained for an example exaggerated pendulum robot 'putt' measured using the high-range sensor design. Figure 4.2 reports the measured loft, lie and face angles for a 'putt' that resulted in nearly a 50° change of loft (25° is substantial for putting). Also shown are the predicted loft, lie and face angles from the simple two-parameter model of Chapter 3.
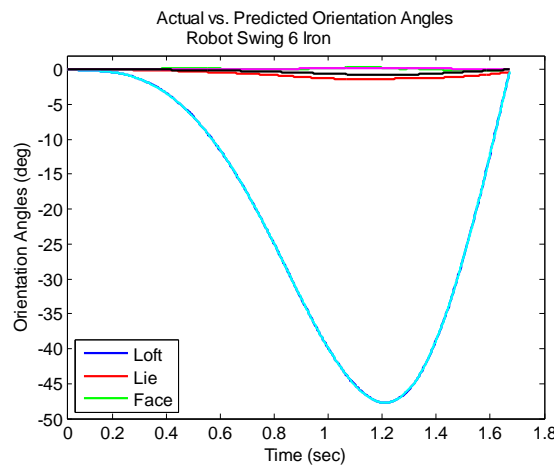
Figure 4.2: Measured and predicted orientation angles for an exaggerated robot putt. The blue, red and green curves are the measured loft, lie, and face angles, respectively. The cyan, magenta and black curves are the corresponding angles predicted by the simple, two-parameter kinematic model.

The agreement apparent in Fig. 4.2 between the measured loft angle (blue curve) and the predicted loft angle (cyan curve) is excellent. There are small discrepancies between the measured and predicted face angle (green and black, respectively) and lie angle (red and magenta, respectively). Overall, the measured lie, loft and face angles at impact return to within $\pm 0.2^{\circ}$ of their values at address, which is positive testimony of the overall accuracy of the high-range design for an 'exaggerated' putt.
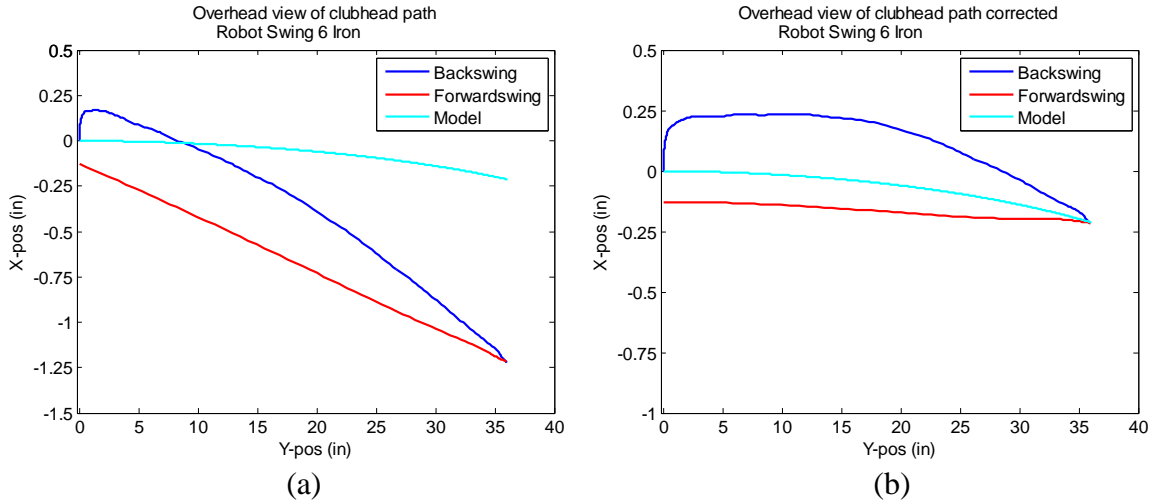
Figure 4.3: Measured and predicted path for the center of the club head during a robot-controlled putt. (a) Uncorrected for slight misalignment of sensor axes to the robot rotation axis. (b) Corrected for this slight misalignment ($-1.4°$ misalignment)

Consider next the club head path as one would observe from overhead in the horizontal (X-Y) plane. Figure 4.3 illustrates the measured club path and that predicted by the two-parameter model where Y denotes position along the intended target line and X denotes a lateral deviation from that line. The scale for the lateral deviation is greatly exaggerated in the figure. The uncorrected path of Fig. 4.3(a) shows a one-sided error due to a small misalignment of the sensor axes to the robot axis of rotation. Following the methods of Ch. 3 (refer to Eq. 3.3.1), we correct for this modest ($-1.4°$) misalignment to arrive at the results of Figure 4.3(b) which illustrate very good agreement (within 0.25 inch) between the measured and the predicted paths for this exaggerated robot putt.

Overall, these tests demonstrate that the high-range sensor yields accurate results for the slow speed dynamics of putting that can be independently measured using the putting robot. The high-range MEMS sensors incorporated in this second-generation design are reported to maintain their linearity throughout their measurement range [28, 33]. Given this expected sensor linearity, one may reasonably expect to achieve a similar level of accuracy for the higher speeds associated with full swings as discussed next.

High Speed Swings of Human Subjects

The example full swings presented in the remainder of this chapter all have the general form of the swing previously illustrated in Fig. 4.1. These swings were measured in the laboratory and with an impact made by striking a soft practice ball. The swings we shall discuss, while not exhaustive in number, capture the major characteristics (e.g., range of motion, club head speed, and club trajectory) common to all full swings. Before doing so, however, we must revisit the definitions of the clubface lie, loft and face angles for the rather large range of motions associated with full swings.

During a full swing these three orientation angles exhibit a considerably greater dynamic range than during a putt. The first definitions of these orientation angles, as given in Chapter 2, did not explicitly describe their domain of definition which must now be understood to meaningfully discuss full swings.

(a)   (b)
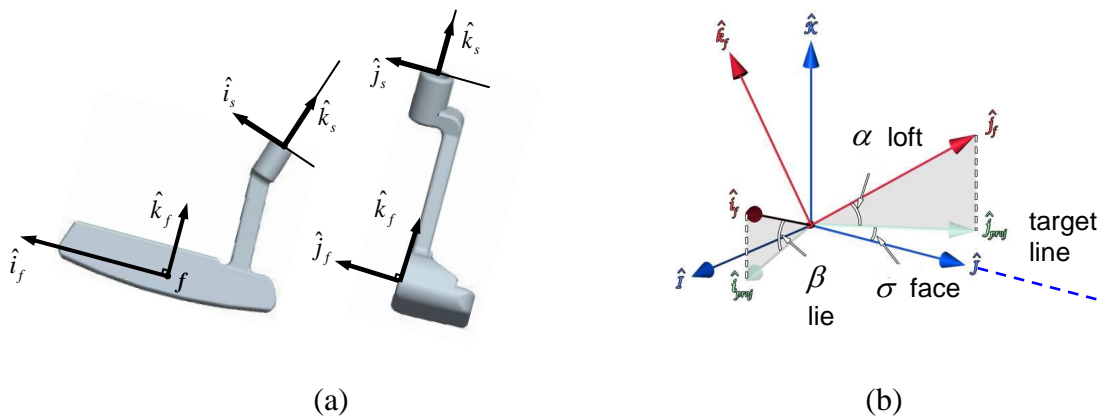
Figure 4.4:   (a) Location and orientation of body-fixed $\left(\hat{i}_f, \hat{j}_f, \hat{k}_f\right)$ and $\left(\hat{i}_s, \hat{j}_s, \hat{k}_s\right)$ frames. (b) Chapter 2 definitions for lie (β), loft (α), and face (σ) orientation angles.

Figure 4.4 contains images reproduced from Ch. 2 to refresh the reader with the definitions for the f and s body fixed reference frames and the orientation angles. We begin by returning to the definition of the lie angle β as illustrated in Fig. 4.4(b). The lie angle β is the angle formed between the horizontal plane and the unit vector $\hat{i}_f$. As

shown in Fig. 4.5 the lie angle, which is defined over the domain $-90^o \leq \beta \leq 90^o$, is positive when $\hat{i}_f$ is above the horizontal plane (a), achieves its maximum when $\hat{i}_f$ is vertically up (b), and is negative when $\hat{i}_f$ is below the horizontal plane (c).
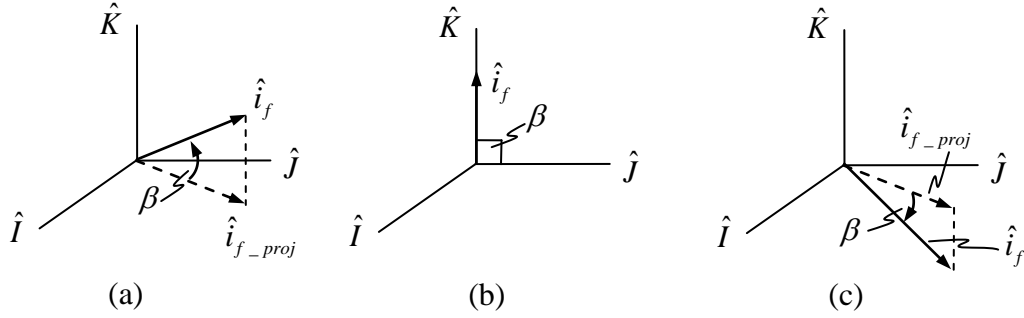
Figure 4.5: Definition of the lie angle β and its domain $-90^o \leq \beta \leq 90^o$. (a) Lie angle is positive when $\hat{i}_f$ is above the horizontal plane $(\hat{I}, \hat{J})$. (b) Lie angle achieves its maximum of $90°$ when $\hat{i}_f$ is vertically up. (c) Lie angle is negative when $\hat{i}_f$ is below the horizontal plane $(\hat{I}, \hat{J})$.

Equivalently, when the $\hat{K}$ component of the vector $\hat{i}_f$ is greater than zero as in Fig. 4.5(a), then $\beta > 0$. When the $\hat{K}$ component of the vector $\hat{i}_f$ is less than zero as in Fig. 4.5(c), then $\beta < 0$. When $\hat{i}_f = \hat{K}$ then $\beta = 90°$. Conversely, when $\hat{i}_f = -\hat{K}$, then $\beta = -90°$.

In an analogous manner, the loft angle α is defined by the angle formed between the unit vector $\hat{j}_f$ and the horizontal plane; refer to Fig. 4.4(b). Doing so establishes the domain for the loft angle as $-90^o \leq \alpha \leq 90^o$.
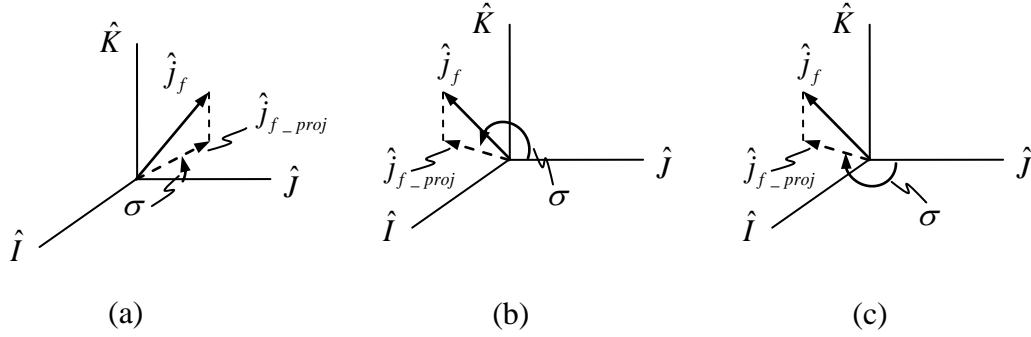
Figure 4.6: Definition of the face angle σ and its domain $-360^{o} \leq \sigma \leq 360^{o}$. (a) Face angle is positive due to counter-clockwise rotation of $\hat{j}_{f\_proj}$ from the $\hat{J}$ axis. The face angle as shown in (b) is positive, while that in (c) is negative.

We now review the definition of the face angle σ employing the illustration of Fig. 4.6. The face angle σ is the angle formed between the $\hat{J}$ axis and the projection of $\hat{j}_{f}$ onto the horizontal plane, denoted $\hat{j}_{f\_proj}$ in this figure. Recall from Chapter 2 that, by definition, the face angle is zero at address since the target line ($\hat{J}$) is established at address. The face angle may then continuously change as the swing develops. A positive face angle results when σ changes counter-clockwise from the $\hat{J}$ axis. A negative face angle results when σ increases clockwise from the $\hat{J}$ axis. Thus, the domain of the face angle is $-360^{o} \leq \sigma \leq 360^{o}$.

In Fig. 4.6(a), σ is positive as it resulted from the counter-clockwise rotation of $\hat{j}_{f\_proj}$ from the $\hat{J}$ axis. Figures 4.6(b) and 4.6(c) show the same $\hat{j}_{f}$ vector, but with σ positive in (b) and negative in (c). The face angle in Fig. 4.6(b) is again positive since it resulted from the counter-clockwise rotation of $\hat{j}_{f\_proj}$ from the $\hat{J}$ axis. By contrast, the face angle in Fig. 4.6(c) is considered negative since it resulted from the clockwise rotation of $\hat{j}_{f\_proj}$ from the $\hat{J}$ axis.

We now proceed to the analysis of an example full swing using a 6-iron. Figure 4.7 illustrates the time history of the club head orientation (lie, loft and face angles) for a typical full swing similar to that illustrated in Fig. 4.1.
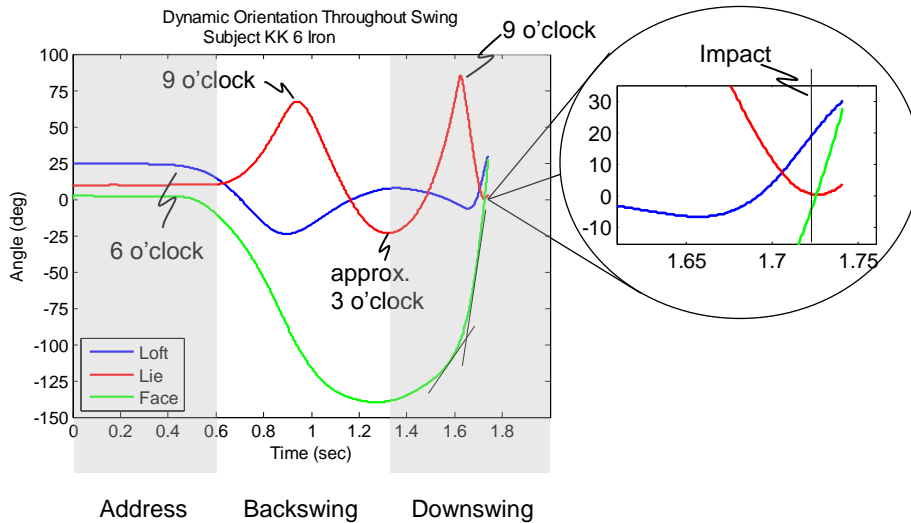
Figure 4.7: Lie, loft and face angles as functions of time for a full swing with 6-iron (subject KK). The annotations describe the approximate location of the golf shaft referred to as position on a clock. Exploded view zooms in on the angles around impact.

Focus first on the lie angle (red) which provides a clear indication of the phases of a full swing including 1) the address, 2) the backswing, and 3) the downswing. The lie angle starts near 0° as the club shaft is held still at address at approximately the 6 o'clock position. The lie angle then increases significantly as the backswing begins. When the club shaft reaches the 9 o'clock position in the backswing, the unit vector $\hat{i}_f$ is nearly aligned with vertical and therefore the lie angle is nearly 90°. The lie angle then decreases as the backswing continues, passing through 0° at approximately the 12 o'clock position of the shaft, and then becoming negative as the shaft heads towards the 3 o'clock position. The shaft frequently approaches or passes through the 3 o'clock position near the end of the backswing at which instant the lie angle achieves its minimum as clearly observable in Fig. 4.7. The ensuing downswing phase is extremely short (approximately 0.4 seconds in this example starting at $t \approx 1.3 \text{sec}$) as the shaft essentially reverses its motion. As the shaft passes back through the 9 o'clock position ($t \approx 1.6 \text{sec}$) the lie angle

again achieves a local maximum. From that point onwards, the lie angle decreases rapidly to another local minimum at or near impact with the ball. At impact the lie angle returns nearly to the value it started with at address and ideally the final lie angle should be 0° as this maximizes the potential contact area between the clubface and the ball.

The face and loft angles of the club also reveal many key elements of the full swing. For example, the face angle monotonically decreases during the backswing as the clubface 'opens' and then monotonically increases during the downswing as the clubface closes. During the downswing, there is a very pronounced increase in the rate of this closing as the shaft passes back through the 9 o'clock position. Starting approximately at the 9 o'clock position, players aggressively 'release' their wrists and rotate the shaft about its long axis thereby increasing the rate at which the clubface is closing. The two straight lines superimposed on the face angle in Fig. 4.7 highlight this large change in the closing rates. In particular, $\dot{\sigma} \approx 250 \frac{\deg}{\sec}$ just before the 9 o'clock position and then changes to $\dot{\sigma} \approx 1000 \frac{\deg}{\sec}$ after the 9 o'clock position for this example swing. This 'release' also occurs very close to the local maximum observed in the lie angle. Simultaneously, the loft angle also increases greatly at and beyond this 'release.' As a result, the entire angular velocity of the club increases very substantially at and beyond the 'release'. As the club approaches impact ($t = 1.720 \sec$ in this example), the loft angle and face angle continue to change rapidly while the lie angle is nearly stationary as best seen in the exploded view in the right side of Fig. 4.7.

Just as in the putting stroke, the final orientation of the clubface at impact should be the same as that at address. Measurable differences in lie, loft and face angles from address to impact are important swing metrics which we also referred to as "closure errors" in Chapter 2. Table 4.1 reports the initial (at address) and final (at impact) orientation angles for the example swing of Fig. 4.7, and we remind the reader that the face angle at address is zero by definition. The table lists values for lie, loft and face angles at the time of impact ($t = 1.720 \sec$) as best estimated from the measured data as well as values 10 milliseconds after this estimated impact time. The rather large changes in the final loft

and face angles during this very short (0.010 second) period are further testimony to the large angular velocity of the club head near impact. There is therefore significant sensitivity of the final loft and face angles with respect to the estimated time of impact.

Subject KK 6 Iron	Initial Lie (*deg*)	Final Lie (*deg*)	Initial Loft (*deg*)	Final Loft (*deg*)	Final Face (*deg*)
$t_{imp} = 1.722\,\text{sec}$	10.2	-1.0	24.8	20.7	-8.3
$t_{imp} + 0.01\text{sec}$	10.2	0.4	24.8	27.1	6.7

Table 4.1: Initial and final orientation angles for trial reported in Fig. 4.7. Final angles are reported for both the estimated impact time as well as 10 milliseconds later.

The initial lie angle $\beta = 10.2°$ at address indicates that the toe of the club head is initially higher than the heel. It is desirable to strike the ball with $\beta = 0°$ as this maximizes the opportunity to impact the ball on the center, "sweet spot", of the clubface. The data of Table 4.1 confirms that the final lie angle for this swing is nearly $0°$ and hence the 'error' at address was effectively corrected during the swing. The manufactured loft of the example club is $30.5°$ so this subject started with less loft than desired at address and then reduced the loft further at impact. The clubface is therefore de-lofted at impact yet the loft is also increasing significantly during the impact process as seen by the $7°$ change in a mere 10 milliseconds. If the face angle is not zero at impact, then the initial ball trajectory will not be aligned with the target line established at address. The negative value of the face angle at impact ($\sigma = -8.3°$) indicates that the initial trajectory would be to the right of the target line. However, the positive value ($\sigma = 6.7°$) a mere 10 milliseconds later confirms that the clubface passes through the 'square' position sometime time in between. Overall the time histories of the lie, loft and face angle provide significant insight into each phase of the swing and the orientation of the clubface at impact.

To gain further insight into the full swing, we now present a three-dimensional view of the position of the club in Fig. 4.8, as computed from the measured sensor data using the algorithms detailed in Chapter 2. This position data has been corrected for sensor drift

by assuming that the final club head position returns to its position at address. While this essentially zeros the position error at impact, it also yields very strong conditions for eliminating drift errors in the rate gyros and accelerometers leading to accurate predictions of club head orientation and swing path. In future work, we will seek to relax this assumption so that the impact location of the ball on the clubface can also be predicted.
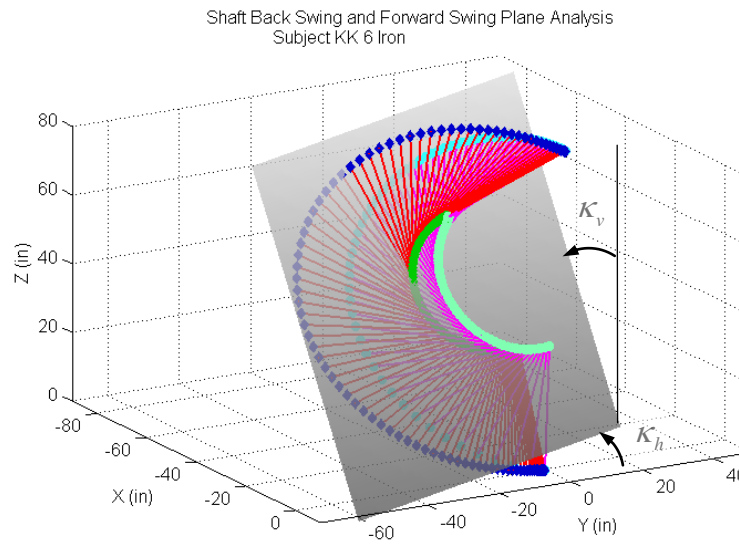
Figure 4.8: Swing path of full swing with 6-iron for example of Fig. 4.7 (subject KK). The centroid of the clubface is represented by the blue dots during the backswing and by the cyan dots during the downswing. The grip (sensor location) is represented by the green dots in the backswing and by the (lighter) sea-green dots in the downswing. The golf shaft is represented as a red line in the backswing and a magenta line in the downswing. The gray plane represents the best fit 'swing plane' during the downswing.

The path of the club in the figure is divided into the backswing and the downswing phases. During the backswing, the clubface centroid is represented by the blue dot, the shaft is represented by the red line, and the grip position (sensor origin) is represented by the green dot. In the downswing, the clubface centroid is represented by a cyan dot, the shaft is represented as a magenta line, and the grip position by the (lighter) sea-green dot. The time interval between successive images for the backswing is 0.010sec and 0.005sec for the downswing. The gray plane superimposed on the club trajectory represents the best fit plane to the shaft position data during the downswing phase.

From the perspective illustrated in Fig. 4.8, the position of the shaft and the club head at the end of the backswing can be readily identified. This position is often used to assess the quality of the backswing. The downswing arc is easily observable in Fig. 4.8, and its arc length could be calculated both for the grip and the club head. The length of the downswing arc for the club head is commonly associated with the final club head speed

for which a longer swing arc often correlates with a greater club head speed at impact. The reader can infer the speed of the club head by noting that higher speeds lead to greater spacing between successive images.

Quantitatively, the instantaneous club head velocity is readily available from calculation following the algorithms detailed in Chapter 2 and the result is shown in Fig. 4.9 where the three components of the club head velocity vector are plotted as functions of time. For the swing considered here, the club head speed at impact was 52.7 mph (and a typical 5-iron (0.5" longer than a 6-iron) speed is be 77 mph, [48]). This swing was intentionally performed at a reduced speed in the laboratory for safety. The direction of the club head velocity at impact is also a key factor in determining the direction the ball will travel. From Fig. 4.9, one observes that the lab-fixed Y component of the velocity dominates at impact as expected since the Y axis defines the target line established at address. The non-zero X velocity component at impact however confirms that the club head trajectory is not perfectly aligned with the intended target line.
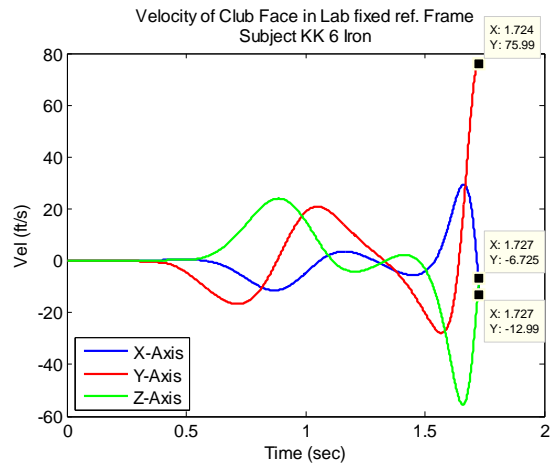
Figure 4.9: Velocity of centroid of clubface for full swing (subject KK). Components reported for the lab-fixed frame. The final data points are the values of the velocity components at impact.

The images in Fig. 4.8 show that the backswing and the downswing are largely confined to two planes which we shall refer to as the "swing planes"; refer to grey plane in the figure for the downswing. A swing plane can be defined by two angles: the angle κ_v that

the plane makes with the vertical Z axis, and the angle κ_h that the plane makes with the target line Y; refer to Fig. 4.8. We often observe that the swing plane that best fits the backswing is distinct from the one that best fits the downswing and this difference may later prove to be important in characterizing these phases of the swing. In the example swing illustrated in Fig. 4.8, the 'vertical' angle $\kappa_v = 21.3^o$ for the backswing and $\kappa_v = 25.9^o$ for the downswing. Similarly, the 'horizontal' angle $\kappa_h = 17.6^o$ for the backswing and $\kappa_h = 5.8^o$ for the downswing indicating that the swing plane for the downswing is rather closely aligned with the target line as expected.

Recall that the results of Table 4.1 demonstrate that the loft and face angles at impact are sensitive to the estimated impact time. Moreover, the impact time observed in the sensor data actually occurs slightly earlier than the associated impact with a perfectly rigid golf club, as assumed in our analysis of the data. During a highly dynamic golf swing, the golf shaft flexes and twists, and at impact the club head normally "leads" the grip. In other words, the *Y* position of point *f* (on the face of the club head) at impact is greater than the *Y* position of point *s* (within the grip) at impact [18, 39, 49]. The analysis of the sensor data tacitly assumes that the golf shaft remains rigid during the swing, an assumption that will also be re-examined in Chapters 5 and 6. Due to these facts, the measured swing (for a flexible club) would then take slightly longer to reach impact if the club were truly rigid. We believe that this time delay might be approximately 0.01 seconds for the swing illustrated in Fig. 4.8 . Extending these results by an additional 0.01 seconds leads to the results shown in Fig. 4.10. Notice now that the grip end of the club at impact finishes very close to its initial position at address. In fact, the final shaft orientation at impact is very similar to its initial orientation at address.
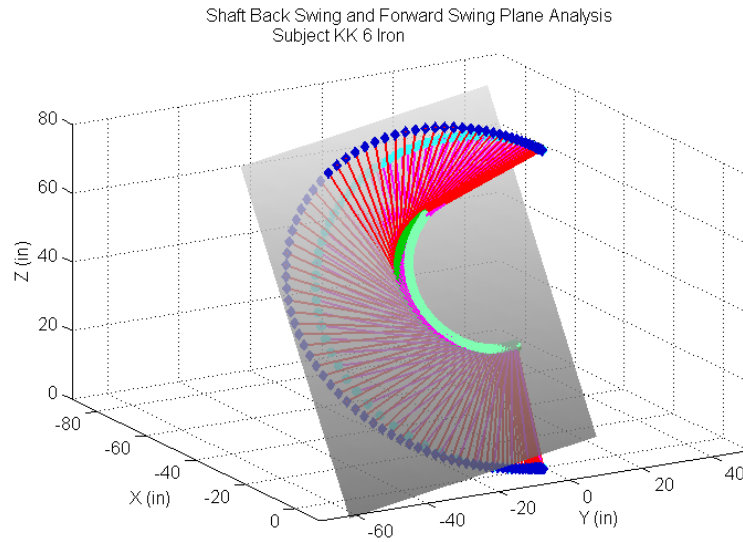
Figure 4.10: Swing path of full swing 6-iron from Fig. 4.8 with an assumed impact delayed by 0.01 seconds.

We conclude this section by presenting results for an example swing with a driver swung at full speed. Doing so confirms much of what was observed with the slower swing with the 6-iron discussed previously.
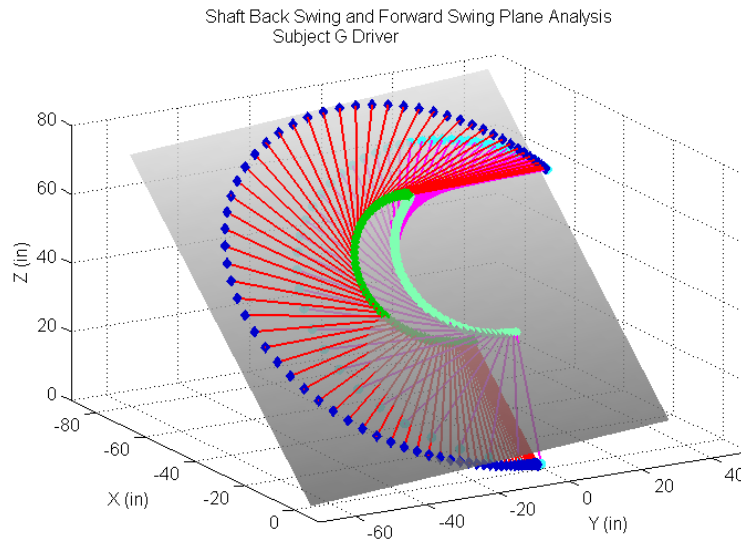
Figure 4.11: Swing path of full swing with driver (subject G). The centroid of the clubface is represented by the blue dots during the backswing and by the cyan dots during the downswing. The grip (sensor location) is represented by the green dots in the backswing and by the (lighter) sea-green dots in the downswing. The golf shaft is represented as a red line in the backswing and a magenta line in the downswing. The gray plane represents the best fit 'swing plane' during the downswing.

Figure 4.11 illustrates the three-dimensional trajectory of the club and Fig. 4.12 reports the associated time histories for the clubface lie, loft and face angles. For this swing, the vertical swing plane angle, κ_v, is 39.7° and 43.7° for the backswing and downward swing, respectively. These angles are significantly greater than those for the 6-iron swing. This is expected since the driver is significantly longer that the 6-iron (46in for driver versus 37.25in for the 6-iron). At impact the club head velocity now attains 87.5 mph which is very typical of the club head speed for drivers [48]. The horizontal swing plane angle, κ_h, is 5.2° and 4.3° for the backswing and downward swing, respectively. These small values confirm that both of these swing planes are well aligned with the target line.

The resulting lie, loft and face angles, illustrated in Fig. 4.12, also confirm the major features noted previously for the swing with a 6-iron (and a different subject). This considerable agreement lends confidence to the future use of these 'swing signatures' for comparing swings of players with different skill levels. Notice again that the lie angle

clearly demarcates the important phases of the swing including address, the backswing, and the downswing. The final values of the lie, loft and face angles at impact are again an important metric of swing performance.
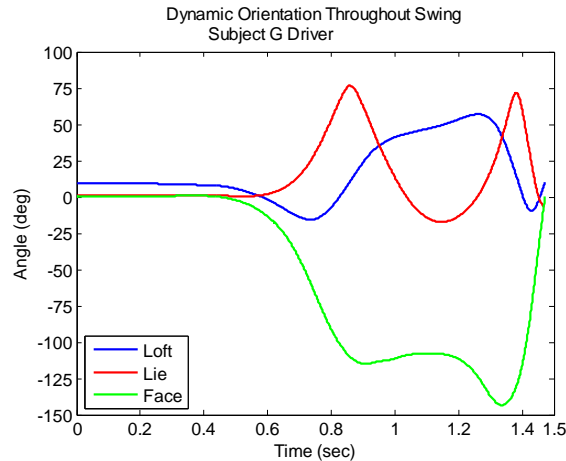
Figure 4.12: Orientation angles as function of time for a full swing with driver with final time 0.01 seconds after impact time estimated from the sensor measurements (subject G).

Table 4.2 reports the 'closure data' for this swing with a driver. The lie, loft and face angle values reported in the first row follow from the estimated impact time from the sensor data. The values of these angles 0.01 seconds later are also reported in the second row for comparison. Again, notice that while the final lie angle is essentially stationary, the loft and face angles continue to change rather rapidly near impact. Note also that the swing for this subject nearly matches the manufactured club lie at address but decreases the lie at impact by approximately 7 degrees. The initial loft at address is very close to the manufactured club loft of 9° and the final loft also remains reasonably close to this value. The open face angle at impact suggests that the initial ball trajectory would be right of the target line based on the estimated impact time from the sensor data; see value in first row. By contrast, if the 'impact' time were delayed by a mere 10 milliseconds, then the face angle is very slightly closed. Clearly, the determination of the actual impact time (or impact time *interval*) is critical to an accurate determination of the orientation of the club head during impact with the ball.

Subject G Driver	Initial Lie (*deg*)	Final Lie (*deg*)	Initial Loft (*deg*)	Final Loft (*deg*)	Final Face (*deg*)
$t_{imp} = 1.462\,\text{sec}$	1.4	-6.7	9.8	5.7	-14.0
$t_{imp} + 0.01\,\text{sec}$	1.4	-6.6	9.8	10.4	0.6

Table 4.2: Initial and final orientation angles for trial reported in Fig. 4.11. Final angles are reported for both the estimated impact time as well as 10 milliseconds later.

4.3 Closure

This chapter describes the successful extension of the hardware and analysis methods developed first for putting in Chapter 2 to 'full swings' using irons and drivers. For low speed swings that can be independently measured using the putting robot, we confirm that the second-generation "high-range" sensor system accurately predicts the planar and exaggerated pendulum stroke. The remainder of the chapter analyzes the high speed swings by human subjects using both irons and drivers.

The analysis of swings made with irons and drivers reveal important features common to all full swings. First, the three major phases of a full swing, including the address, the backswing and the downswing, are readily distinguished using the dynamic lie angle. Second, the loft and face angles change very rapidly during the final portion of the downswing following the 'release' of the wrists starting at approximately the 9 o'clock position with impact occurring at approximately the 6 o'clock position. Both the backswing and the downswing are largely confined to distinct swing planes that are well defined from the three-dimensional club trajectories computed from the sensor data. The orientation of the swing plane with respect to vertical and with respect to the target line established at address may become useful metrics in future studies of golfer skill. In addition, the measured club head speed and the lie, loft and face angles at impact are of immediate use in assessing golfer skill. However, we also note that the measurement of the impact time or the impact time *interval* requires further study and definition, perhaps by independent means.

CHAPTER 5

PLANAR FLEXIBLE MODEL OF A GOLF CLUB
AND EXPERIMENTAL VALIDATION

The objective of this chapter is to derive and validate a model which predicts the flexible

motion of a golf club. The overall motion of the club can be decomposed into the rigid

body motion of the grip and the flexible motion of the shaft relative to the grip; refer to

Chapter 2. Recall that the flexible motion is driven by the rigid body motion and that the

sensor system precisely measures the latter. Thus, a model for the flexible body motion

may now be developed with the measured rigid body motion as the "excitation". The

overall motion, of course, ultimately defines the absolute motion of the club head and

predicting this overall motion is now the goal of this chapter. This chapter establishes

this modeling concept by considering the simpler case of a purely planar motion of the

club head. Chapter 6 extends this planar model to a full three-dimensional model.

5.1 Derivation of Planar Model (Lagrange Formulation)
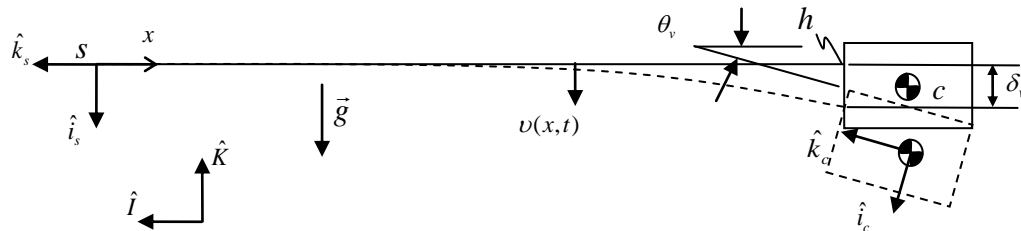
Figure 5.1: Diagram of planar model. Points s, h and c denote the origin of the shaft
frame, the hosel (point of intersection of shaft and club head), and the mass center of the
club head, respectively. Two generalized coordinates (δ_v and θ_v) are introduced to
describe the deflection and rotation of the end of the shaft at the hosel.

Figure 5.1 illustrates a massless and flexible beam (the shaft of the club) attached to the

club head (rigid body) of mass m. These components form the dynamic model of the golf

club. The lab fixed frame $\left(\hat{I},\hat{K}\right)$ is introduced with the unit vector $\hat{K}$ aligned with vertical $\left(\vec{g}=-g\hat{K}\right)$. Point s, located at the grip end of the club, represents the location of the MEMS accelerometer as previously introduced in Chapter 2. The body fixed reference frame $\left(\hat{i}_s,\hat{k}_s\right)$ is located at s and defines the tangent and normal directions of the *undeformed* or rigid shaft (solid line in Fig. 5.1). A second body-fixed frame $\left(\hat{i}_c,\hat{k}_c\right)$ is located at the mass center of the club head c, and defines the tangent and normal directions of the *deformed* shaft at the end of the shaft denoted as point h. Point h is introduced at the intersection of the shaft and the club head and it is commonly referred to as the *hosel*. The coordinate $\upsilon\left(x,t\right)$ represents the deflection of the flexible shaft from its undeformed configuration with x being the independent spatial coordinate measured along the undeformed shaft from s towards h. The deflection of the shaft at point h (where $x=L$) is denoted as δ_v (the deflection at the hosel) and the slope of the shaft at this same point h is denoted as θ_v (the rotation of the deformed shaft relative to the undeformed shaft at the hosel).

It is assumed that the shaft bends as an inextensible and massless Euler-Bernoulli beam. The justification for using the linear approximations inherent in Euler-Bernoulli beam theory rests on the observed fact that a typical maximum deflection of the shaft at the hosel in a highly dynamic swing remains less than 15 cm [39] relative to a typical shaft length of 110 cm [50]. Thus the shaft, which is truly slender, undergoes deflections that are also reasonably small. Likewise, the mass of a typical shaft is approximately 110 gm (steel) or 75 gm (graphite) [50] relative to the mass of a typical head which is 200 gm (driver) or 265 gm (irons) [50]. This fact, coupled to the fact that the shaft only changes direction once, between the back and forward swings, during the swing (prior to impact) suggests that one can reasonably ignore the mass of the shaft to a first approximation. The justification for ignoring the extension of the shaft rests on the fact that the shaft is considerably stiffer in extension than bending and that any possible extension due to the 'spin up' has negligible influence on the club dynamics. Of course, any of these

assumptions could be relaxed in the future should they someday be deemed important for improved model accuracy. Dissipation, while initially ignored in the derivation, is appended to the model at the end.

We now seek to describe the deflection of the beam, $\upsilon(x,t)$, wholly in terms of the two generalized coordinates, δ_v and θ_v. First, we establish the boundary conditions for the beam. At point s we require that the flexible beam remain *tangent* to the undeformed or 'rigid' beam. The kinematics of this rigid beam are directly measured via the sensor system. Thus, the flexible beam must satisfy a 'clamped' boundary condition at the origin, s, of the shaft frame. Meanwhile, the slope and deflection at the opposite end, point h, are the generalized coordinates δ_v and θ_v, respectively. Consider next Fig. 5.2 which shows a cantilevered beam subjected to a terminal force and moment.
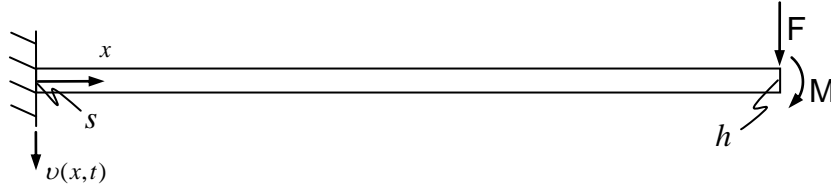
Figure 5.2: Cantilevered Euler-Bernoulli beam subject to terminal force F and bending moment M.

By superposition of classical solutions for this Euler-Bernoulli beam, the displacement $\upsilon(x,t)$, and the slope of the beam centerline, $\upsilon'(x,t)$, are

$$\upsilon(x,t) = \frac{Fx^2}{6EI}(3L-x) + \frac{Mx^2}{2EI}$$

$$\upsilon'(x,t) = \frac{x}{EI}(FL+M) - \frac{Fx^2}{2EI}$$

(5.1.1)

Evaluating these functions at $x=L$ and solving for F and M in terms of δ_v and θ_v yields

$$F = \frac{12EI}{L^3}\delta_v - \frac{6EI}{L^2}\theta_v$$

$$M = -\frac{6EI}{L^2}\delta_v + \frac{4EI}{L}\theta_v$$

(5.1.2)

Substituting (5.1.2) into (5.1.1) yields

$$\upsilon\left(x,t\right) = \frac{x^2\left(-\theta_v L^2 + 3\delta_v L + x\theta_v L - 2x\delta_v\right)}{L^3} \tag{5.1.3}$$

This displacement, now expressed as a function of the two generalized coordinates, will be used in determining the strain energy of the beam.

The potential energy due to elastic deformation can be generalized as:

$$V_{strain} = \frac{1}{2}Fx \tag{5.1.4}$$

with F being a generalized force and x being a generalized displacement. If we consider a beam subject to a normal stress, the potential energy per unit volume is

$$dV_{strain} = \frac{1}{2}\sigma\varepsilon \tag{5.1.5}$$

Applying Hooke's law (and ignoring Poisson contractions), the strain energy per unit volume is simply.

$$dV_{strain} = \frac{1}{2}E\varepsilon^2 \tag{5.1.6}$$

Figure 5.3 illustrates the kinematic relationship between the strain, the curvature $\frac{1}{\rho}$ of the neutral axis, and the distance y of a beam element from the neutral axis.

$$\varepsilon = \frac{\Delta L}{L} = \frac{\Delta\theta(\rho+y)-\Delta\theta\rho}{\Delta\theta\rho} = \frac{y}{\rho}$$
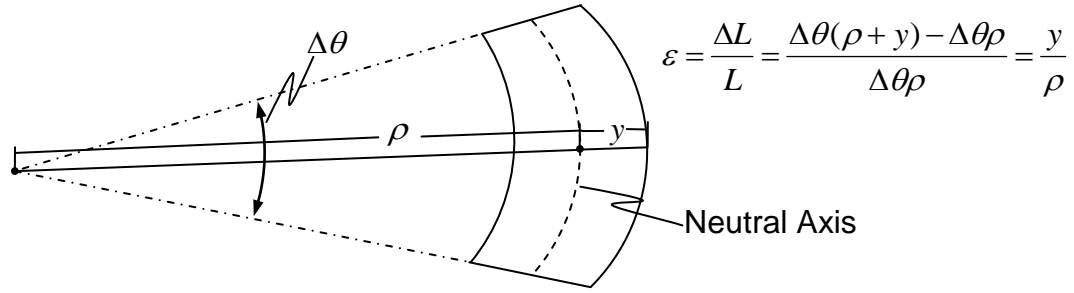
Figure 5.3: Kinematic relationship between radius of curvature and strain in a beam due to bending.

Combining this result with (5.1.6) and integrating over the volume of the beam yields the strain energy:

$$V_{strain} = \int_{vol} \frac{1}{2} E \left(\frac{y}{\rho} \right)^2 dvol$$

$$V_{strain} = \frac{1}{2} E \int_L \left(\frac{1}{\rho} \right)^2 dx \int_A y^2 dA \tag{5.1.7}$$

$$V_{strain} = \frac{1}{2} EI \int_L \left(\frac{1}{\rho} \right)^2 dx$$

recalling that integral of y^2 over the cross section area is defined the area moment of inertia I. Following the standard sign convention introduced in Bedford [37], the relationship between curvature and the displacement of the neutral axis, $\upsilon(x,t)$, is

$$\frac{1}{\rho} = \frac{\partial^2 \upsilon(x,t)}{\partial x^2} \tag{5.1.8}$$

which, when substituted into (5.1.7) yields

$$V_{strain} = \frac{1}{2} EI \int_L \left(\frac{\partial^2 \upsilon(x,t)}{\partial x^2} \right)^2 dx \tag{5.1.9}$$

Substituting the displacement (5.1.3) into (5.1.9) and integrating along the length of the beam leads to the following expression of the beam strain energy wholly in terms of the two generalized coordinates

93

$$V_{strain} = \frac{2EI\left(3\delta_v^2 - 3L\theta_v\delta_v + L^2\theta_v^2\right)}{L^3} \tag{5.1.10}$$

The 2D model considers the club's motion in the vertical $\left(\hat{I}, \hat{K}\right)$ plane, therefore the potential energy due to gravity must also be included. Fig. 5.4 provides two illustrations to aid in the development of an expression for the gravitational potential. The gravitational potential of the club head of mass m is

$$V_{grav} = mgZ \tag{5.1.11}$$

where Z is the height of the head measured in the inertial frame. Refer to Fig. 5.4 where Z is the $\hat{K}$ component of the position vector $\vec{R}_c$. Here, capital R denotes a position vector defined in the inertial frame.
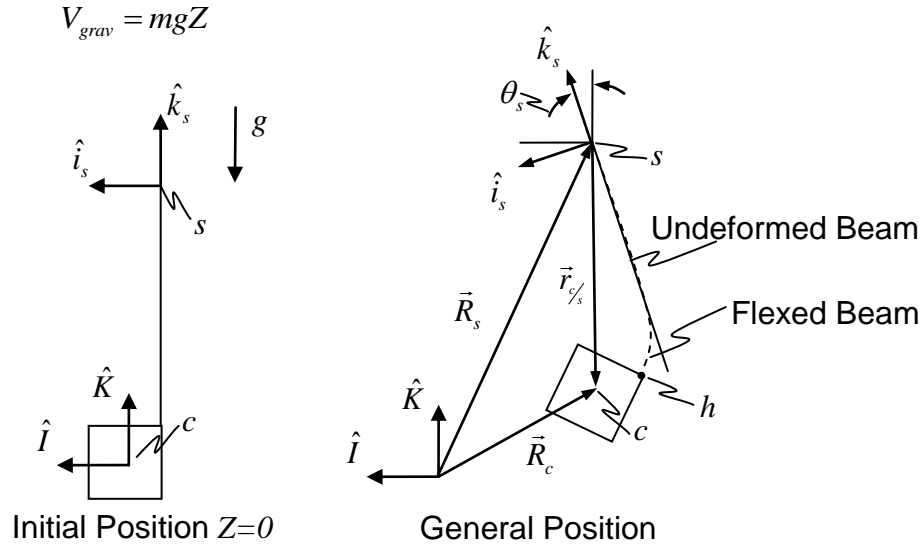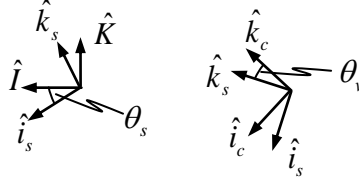
Figure 5.4: Definition of the gravitational potential energy of the club head. The initial position with $Z=0$ and a general position $Z > 0$.

The vector $\vec{R}_c \triangleq X\hat{I} + Z\hat{K}$ and can be written as $\vec{R}_c = \vec{R}_s + \vec{r}_{c/s}$ with $\vec{r}_{c/s} = \vec{r}_{c/h} + \vec{r}_{h/s}$. Here, the lower case r denotes a position vector measured in a body-fixed frame. At this point it is convenient to introduce the coordinate transformations from $\left(\hat{i}_s, \hat{k}_s\right)$ to $\left(\hat{i}_c, \hat{k}_c\right)$ and from

$\left(\hat{I},\hat{K}\right)$ to $\left(\hat{i}_s,\hat{k}_s\right)$ per the following illustration. These transformations will be referred to as $^cC^s$ and $^sC^L$ respectively.

$$\begin{bmatrix}\hat{i}_c\\\hat{k}_c\end{bmatrix}=\begin{bmatrix}\cos\theta_v & \sin\theta_v\\-\sin\theta_v & \cos\theta_v\end{bmatrix}\begin{bmatrix}\hat{i}_s\\\hat{k}_s\end{bmatrix}=\begin{bmatrix}1 & \theta_v\\-\theta_v & 1\end{bmatrix}\begin{bmatrix}\hat{i}_s\\\hat{k}_s\end{bmatrix}$$

$$\begin{bmatrix}\hat{i}_s\\\hat{k}_s\end{bmatrix}=\begin{bmatrix}\cos\theta_s & -\sin\theta_s\\\sin\theta_s & \cos\theta_s\end{bmatrix}\begin{bmatrix}\hat{I}\\\hat{K}\end{bmatrix} \quad;\ \theta_s=\int\omega_s dt$$

(5.1.12)

In doing so, we also assume that the angle θ_v remains small to be consistent with the Euler-Bernoulli hypothesis of small rotations of the beam cross section. Expanding the terms of $\vec{r}_{c/s}$ leads to

$$\vec{r}_{c/h}=x_c\hat{i}_c-z_c\hat{k}_c=\left(^cC^s\right)^T\begin{bmatrix}x_c\hat{i}_c & -z_c\hat{k}_c\end{bmatrix}^T=\left(x_c+\theta_v z_c\right)\hat{i}_s+\left(-z_c+\theta_v x_c\right)\hat{k}_s$$

$$\vec{r}_{h/s}=\delta_v\hat{i}_s-L\hat{k}_s$$

(5.1.13)

$$\vec{r}_{c/s}=\left(\delta_v+x_c+\theta_v z_c\right)\hat{i}_s+\left(-\left(L+z_c\right)+\theta_v x_c\right)\hat{k}_s$$

Transforming the result of (5.1.13) to the inertial reference frame and substituting into $\vec{R}_c$ provides

$$\vec{R}_s=X_s\hat{I}+Z_s\hat{K}\quad\text{Derived from measurement}$$

$$\vec{R}_{c/s}=\frac{\left(\sin\theta_s\left(-\left(L+z_c\right)+\theta_v x_c\right)+\cos\theta_s\left(\delta_v+x_c+\theta_v z_c\right)\right)\hat{I}}{+\left(\cos\theta_s\left(-\left(L+z_c\right)+\theta_v x_c\right)-\sin\theta_s\left(\delta_v+x_c+\theta_v z_c\right)\right)\hat{K}}$$

(5.1.14)

$$Z=Z_s+\left(\cos\theta_s\left(-\left(L+z_c\right)+\theta_v x_c\right)-\sin\theta_s\left(\delta_v+x_c+\theta_v z_c\right)\right)$$

which yields the gravitational potential wholly in terms of the two generalized coordinates. The gravitational potential and the strain energy constitute the total potential energy function for the model. We now turn our attention to describing the kinetic energy.

Since the shaft is considered to be massless the kinetic energy reduces to that of the club head. The total kinetic energy is thus given by

$$T=\frac{1}{2}m\vec{v}_c^T\vec{v}_c+\frac{1}{2}I_{yy}\vec{\omega}_c^2$$

(5.1.15)

where $\vec{v}_c$ is the absolute velocity of point c, $\vec{\omega}_c$ is the absolute angular velocity of the club head and I_{yy} is the centroidal mass moment of inertia about the out of plane axis $\hat{j}_c$.

The following equation block (5.1.16) details the expansions used to develop the kinetic energy. These expansions demonstrate that the vectors $\vec{v}_c$ and $\vec{\omega}_c$ can be written in terms of known geometrical quantities, namely L, x_c, and z_c, known measurands from the inertial sensor system, namely v_x, v_z, ω_s (refer to Chapter 2), and finally the generalized coordinates and their derivatives, $\left(\delta_v, \dot{\delta}_v, \theta_v, \dot{\theta}_v \right)$.

$$\vec{v}_c = \vec{v}_h + \vec{\omega}_c \times \vec{r}_{c/h}$$

$$\vec{r}_{c/h} = \left(x_c + \theta_v z_c \right)\hat{i}_s + \left(-z_c + \theta_v x_c \right)\hat{k}_s \quad \text{from eq. (5.1.13)}$$

$$\vec{\omega}_c = \vec{\omega}_s - \dot{\theta}_v \hat{j}_c$$

$$\vec{\omega}_s = \omega_y \hat{j}_s \quad \text{(measured by sensor)}$$

$$\vec{\omega}_c = \left(\omega_y - \dot{\theta}_v \right)\hat{j}_s \quad \text{Note: } \hat{J} = \hat{j}_s = \hat{j}_c$$

$$\vec{v}_h = \vec{v}_s + \vec{v}_{h/s} + \vec{\omega}_s \times \vec{r}_{h/s}$$

$$\vec{v}_s = v_x \hat{i}_s + v_z \hat{k}_s \quad \text{(measured by sensor)}$$

$$\vec{r}_{h/s} = \delta_v \hat{i}_s - L\hat{k}_s$$

$$\vec{v}_{h/s} = \dot{\delta}_v \hat{i}_s$$

$$\vec{v}_h = \left(v_x - L\omega_y + \dot{\delta}_v \right)\hat{i}_s + \left(v_z - \delta_v \omega_y \right)\hat{k}_s$$

$$\vec{v}_c = \begin{array}{l} \left(v_x - L\omega_y + \dot{\delta}_v + x_c \omega_y \theta_v + z_c \dot{\theta}_v - x_c \theta_v \dot{\theta}_v \right)\hat{i}_s \\ + \left(v_z - \delta_v \omega_y - \omega_y \delta_v - z_c \omega_y \theta_v + x_c \dot{\theta}_v + z_c \theta_v \dot{\theta}_v \right)\hat{k}_s \end{array}$$

$$(5.1.16)$$

At this point we introduce Lagrange's equation:

$$\frac{d}{dt}\left(\frac{\partial T}{\partial \dot{q}_i} \right) - \frac{\partial T}{\partial q_i} + \frac{\partial \left(V_{strain} + V_{grav} \right)}{\partial q_i} = 0 \quad i = 1, 2 \qquad (5.1.17)$$

with all necessary quantities developed above in terms of the generalized coordinates, denoted as q_i. Evaluating Lagrange's equation yields the following two equations of motion

$$\underline{M}\ddot{q} + \underline{C}\dot{q} + \underline{K}q + \underline{F} = 0$$

$$q = \begin{bmatrix} \delta_v \\ \theta_v \end{bmatrix}$$

$$\underline{M} = \begin{bmatrix} m & mz_c \\ mz_c & I_{yy} + mx_c^2 + mz_c^2 \end{bmatrix}$$

$$\underline{C} = \begin{bmatrix} 0 & 2mx_c\omega_y \\ -2mx_c\omega_y & 0 \end{bmatrix}$$

$$\underline{K} = \begin{bmatrix} -m\omega_y + \dfrac{12EI}{L^3} & -m\left(z_c\omega_y^2 - x_c\dot{\omega}_y\right) - \dfrac{6EI}{L^2} \\[3mm] -m\left(z_c\omega_y^2 + x_c\dot{\omega}_y\right) - \dfrac{6EI}{L^2} & -m\left(x_c^2\omega_y^2 + z_c^2\omega_y^2 + x_c\dot{v}_x - z_c\dot{v}_z - Lx_c\dot{\omega}_y\right) + \dfrac{4EI}{L} \end{bmatrix} \qquad (5.1.18)$$

$$\underline{F} = \begin{bmatrix} -m\left(x_c\omega_y^2 - v_z\omega_y + g\sin\theta_s - \dot{v}_x + \left(L + z_c\right)\dot{\omega}_y\right) \\[3mm] m\left(L\omega_y^2 x_c + gx_c\cos\theta_s - v_x\omega_y x_c + \dot{v}_z x_c - gz_c\sin\theta_s + z_c v_z\omega_y + z_c\dot{v}_x - Lz_c\dot{\omega}_y\right)\ldots \\[3mm] -\left(I_{yy} + mz_c^2 + mx_c^2\right)\dot{\omega}_y \end{bmatrix}$$

where nonlinear terms have also been dropped.

The matrix equations of (5.1.18) are a coupled set of 2nd order ordinary differential equations (ODE's) for the two unknowns generalized coordinates. There are numerous ways to numerically solve these ODE's with the measured data from the MEMS sensors. One method is to first decouple the highest order derivatives terms to arrive at a set of second order equations which can then be readily cast in first order form for implementation in standard ODE solvers. We pursued this direction to integrate the equations of motion using standard Matlab solvers.

5.2 Experimental Validation of Planar Model

Having developed a planar model that describes the flexible motion of a golf club, we now seek to utilize this model in predicting the total motion of the club head. Before doing so however, a number of model parameters must be determined from experiments or from known geometric and inertial properties of the club being analyzed as reviewed below.

97

The parameters x_c and z_c describe the location of the mass center, c, relative to the hosel, h, and are a function of the club head geometry. The parameter L is the distance from s to h as determined by the shaft geometry and the placement of the sensor within the shaft. I_{yy} and m define the club head inertia properties for the planar model. The shaft flexural rigidity EI can be estimated by numerous methods. One method is to establish E from the specific shaft material and then determine an average I, based on the shaft geometry. Golf shafts are tapered and therefore I varies along the length of the shaft. In the derivation above, we assumed an average value of I though the model could readily be modified to account for the exact taper. A pragmatic alternative is to simply measure the average EI for the entire assembled club experimentally by fitting a model for an equivalent uniform shaft to the experimental data for static shaft deflection as described further in this chapter.

We sought to develop a simple experimental method to directly measure the generalized coordinates, δ_v and θ_v, for a club. We elected to use a standard (30Hz frame rate) video camera and a specially designed club with dynamics both slow and large enough to resolve with a video camera. The club was also designed to make the calculation and identification of the model parameters relatively straight forward. A standard golf shaft was used with a large aluminum head for this purpose as shown later in Fig. 5.6. The associated model parameters are reported in Table 5.1. Note that the club head mass (4 lb) is about an order of magnitude larger than that standard club (0.46 lb) which leads to the intentional slow and exaggerated shaft flexing in these tests.

Parameter	Value	Units	Parameter	Value	Units
L	3.69	ft	m_c	4.18	lbm
x_c	0.15	ft	I_{zz}	5.93×10^{-2}	$lbm \cdot ft^2$
z_c	0.00	ft	EI	188	$lbf \cdot ft^2$

Table 5.1: Parameters for club used in the validation of the planar model.

Video Calibration

Three calibration steps are needed in order to make an accurate comparison between the video data, the measurements from the MEMS sensor, and ultimately the output from the planar model. The first step is to synchronize in time the data from the MEMS sensor and the camera. This entails determining the frame rate of the camera and identifying a starting event which is clearly visible in the camera and simultaneously detectable in the MEMS sensor data. The total time of the video clip is divided by the total number of frames in that clip to determine an average frame rate per

$$\text{Frame Rate} \left(\frac{\text{sec}}{\text{frame}} \right) = \frac{\text{Total Clip Time}}{\text{Total frames}} \left(\frac{\text{s}}{\text{F}} \right) \tag{5.2.1}$$

To ensure good synchronization of a video clip, the club head was first impacted on a (wooden) backstop block as illustrated in Fig. 5.5. This impact causes high frequency vibration of the shaft which is easily identified in the MEMS sensor output, as also shown in Fig. 5.5. From this test the impact frame in the video and the impact time in the sensor data are determined. This information, along with the frame rate, enables the synchronization of events between the video and sensor data per

$$\text{Event Frame} = \text{Impact Frame} - (t_{impact} - t_e) \frac{1}{\text{Frame Rate}} \tag{5.2.2}$$

The time when an event occurs in the MEMS data are denoted as t_e.

Frame 300   Frame 301

Raw angular velocity data
from MEMS sensor
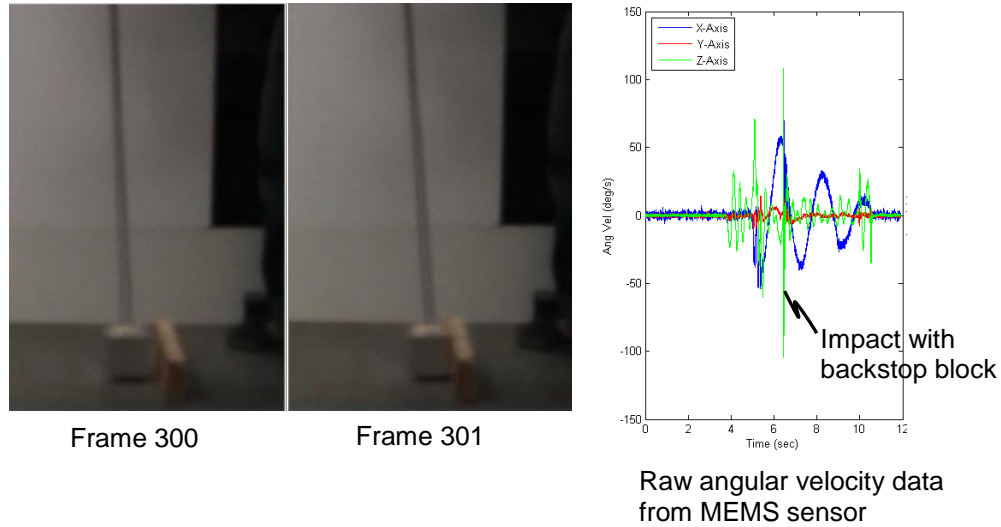
Figure 5.5: An example illustration of how the MEMS data and the video file are synchronized in time. Frame 300 shows club head just prior to impacting the wooden back stop. Frame 301 shows club head during impact.

The second step in calibrating the video is to covert pixel discretization to dimensions of length. This calibration is accomplished by viewing an object of known length in the video. For these experiments, the reference lengths used were the edges of the club head. The calibration is done in both the horizontal and vertical directions to account for any differences caused by the camera lens. The vertical and horizontal lengths of the club head were measure using a dial caliper (accurate to 0.001"). Figure 5.6 below identifies key points on the test club and includes an exploded view of the club head section. The exploded view of the club head shows example data for calibration of the horizontal and vertical pixel-to-inch scale factor.
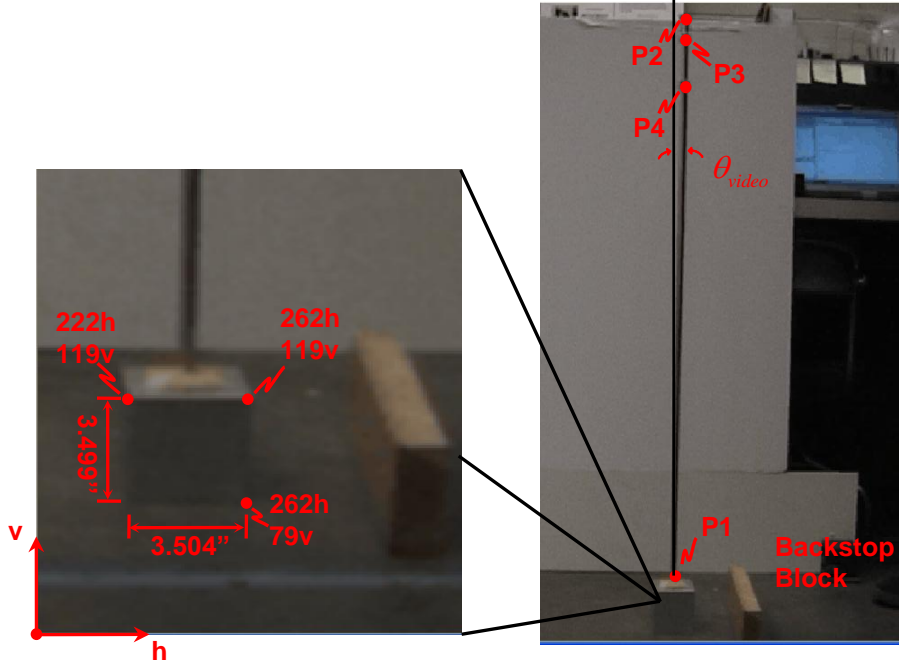
Figure 5.6: Right image shows the flexible club experimental setup calling out key points. Left image is a zoomed-in view of the club head that shows an example calculation of the horizontal and vertical pixel-to-inch scale factor calibrations.

The pixel-to-inch scale factor calibrations are given by

$$SF_v = \frac{in}{\Delta pixel_{vert}}, SF_h = \frac{in}{\Delta pixel_{horz}} \qquad (5.2.3)$$

The third step in calibration is to measure the misalignment of the camera's vertical axis from true vertical. The MEMS sensor accurately measures the sensor's orientation relative to gravity. The sensor is mounted in the shaft and therefore calculates the orientation of the shaft relative to vertical. The orientation of the shaft in the video can be calculated from points P1 and P2 shown in Fig. 5.6, using the following relationship.

$$P1 = \begin{pmatrix} h_1 \\ v_1 \end{pmatrix} pixels, P2 = \begin{pmatrix} h_2 \\ v_2 \end{pmatrix} pixels$$

$$\Delta h" = (h_2 - h_1)SF_h$$

$$\Delta v" = (v_2 - v_1)SF_v \qquad (5.2.4)$$

$$\theta_{video} = \tan^{-1}\left(\frac{\Delta v"}{\Delta h"}\right)$$

The vertical misalignment of the camera axis, θ_{vert}, represents the difference of the MEMS sensor measurement, θ_{MEMS}, and θ_{video}, calculated from analyzing the video. The amount of misalignment was one degree on average for the following tests.

The other points noted in Fig. 5.6 include the positions of two clamps attached to the shaft that can be used to hold a second and rigid 'pointer' shaft just in front of the club. The clamps also serve as visible reference points for determining locations on the shaft during analysis of the video. When the 'pointer' shaft is attached to the club, it tracks the orientation of the grip section of the shaft with no deflection and thus follows the dynamics of a perfectly 'rigid' shaft. Three different methods for determining the orientation of the grip end of the shaft where the sensor is mounted were explored. The first method uses a long 'pointer' shaft of nearly equal length to the flexible shaft and mounted in front of the flexible shaft relative to the camera. This long pointer shaft would offer the best opportunity to observe the motion of the rigid shaft were it not for the unavoidable vibrations caused during movement. A small damping element was added to the top the club head to partially address this concern. The second attempt was to use a rather short (approximately 1 *ft* long) pointer shaft which, being stiffer, did not suffer the same vibrations. However, the shorter length leads to poorer resolution of position and orientation from the pixilated video output. The final method was to use the shaft clamp as a reference point for the position of the grip end of the club and then use the MEMS sensor data to establish the orientation of the rigid portion of the shaft in the video. This final method proved to be inaccurate and the results will not be presented.

We present next three types of tests that serve to validate the flexible golf club planar model. These tests include 1) static measurements of shaft deflection, 2) dynamic measurements of the natural frequency of the shaft/head system, and 3) the transient measurements of the shaft/head system dynamics under measured accelerations of the grip.

Test 1: Validation of Static Deflections

The simplest validation test is to compare the output of the planar model with the static deflection of the club under gravity as measured by video. This test consists of holding the shaft at a known and constant angle relative to vertical and then measuring the resulting static deflection of the shaft. The results of this test were also used to determine the average *EI* for the club. Under static conditions, the planar model reduces to

$$(\ddot{\delta}_v = \dot{\delta}_v = 0 \ , \ \dot{\omega}_y = \omega_y = 0 \ , \ \ddot{\theta}_v = \dot{\theta}_v = 0 \ , \ v_x = v_z = \dot{v}_x = \dot{v}_z = 0)$$

$$\begin{bmatrix} \dfrac{12EI}{L^3} & -\dfrac{6EI}{L^2} \\ -\dfrac{6EI}{L^2} & \dfrac{4EI}{L} \end{bmatrix} \begin{bmatrix} \delta_v \\ \theta_v \end{bmatrix} = \begin{bmatrix} mg\sin\theta_s \\ -mg\left(x_c\cos\theta_s - z_c\sin\theta_s\right) \end{bmatrix} \tag{5.2.5}$$

which can readily be solved for the static shaft displacement and rotation at the hosel. Equation (5.2.5) can also be solved for *EI* in terms of the displacement at the hosel. This latter calculation results in

$$(\text{for this club } z_c = 0)$$

$$EI = \frac{mgL^2\left(\left(2L+3z_c\right)\sin\theta_s - 3x_c\cos\theta_s\right)}{6\delta_v} \tag{5.2.6}$$

The variables δ_v and θ_s, measured from a video image, are then used to estimate *EI*.

Figure 5.7 is a typical video frame analyzed during the static testing. Recall that the generalized coordinates of the flexible model are the deflection of the hosel δ_v and the rotation of the shaft at the hosel θ_v, both measured relative to the undeformed shaft as shown in Fig. 5.7.
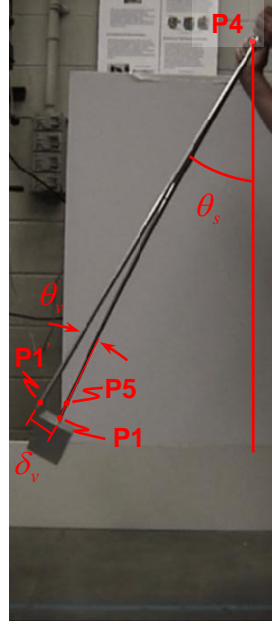
Figure 5.7: Example of static deflection test. The pointer shaft is defined by points P1$^{'}$ and P4. The flexible club shaft passes though points P4, P5 and P1. Points P1 and P5 define the tangent at the end of the shaft and the angle formed between this tangent and the pointer shaft is denoted by θ_v. The deflection of P1 from the pointer shaft is denoted by δ_v.

The tests were conducted at three nominal angles $\theta_s = 15$, 20 and 30 degrees. At each angle δ_v, θ_v, and θ_s were computed as detailed in (5.2.7) below.

$$\theta_v = \theta_s - \theta_{flex}$$

$$\theta_s = \tan^{-1}\left(\frac{\Delta v_{rigid}}{\Delta h_{rigid}}\right)$$

$$\delta_v = \sqrt{\Delta h_{in}^{\;2} + \Delta v_{in}^{\;2}} \qquad \Delta v_{rigid} = \left|v_{P4} - v_{P1'}\right| SF_v$$

$$\Delta h_{in} = \left|h_{P1} - h_{P1'}\right| SF_h \quad \text{and} \quad \Delta h_{rigid} = \left|h_{P4} - h_{P1'}\right| SF_h \qquad (5.2.7)$$

$$\Delta v_{in} = \left|v_{P1} - v_{P1'}\right| SF_h$$

$$\theta_{flex} = \tan^{-1}\left(\frac{\Delta v_{flex}}{\Delta h_{flex}}\right)$$

$$\Delta v_{flex} = \left|v_{P1} - v_{P5}\right| SF_v$$

$$\Delta h_{flex} = \left|h_{P1} - h_{P5}\right| SF_h$$

The calculated *EI* for each trial, using the computed values of δ_v and θ_s, are given in Table 5.2.

Trial	δ_v (in)	θ_v (deg)	$EI\,(lbf \cdot ft^2)$
Trial 1	1.31	15.5	182
Trial 2	1.63	21.8	203
Trial 3	2.57	30.9	178

Table 5.2: Results of *EI* calculated from static video tests

The value for *EI* used in the model, calculated as the average from the three trials above, is $188\,lbf \cdot ft^2$. Using this average value of *EI* in the planar model results in the following comparison of the video measurements and model predictions for these three trials.

Trial	Approx. Ang.	δ_v Video (in)	δ_v Model (in)	Error (in)	θ_v Video (deg)	θ_v Model (deg)	Error (deg)
Trial 1	15	1.37	1.27	0.10	5.9	2.5	3.4
Trial 2	20	1.63	1.76	-0.13	1.9	3.5	-1.6
Trial 3	30	2.57	2.44	0.13	5.6	4.8	0.8

Table 5.3: Comparison of video measurements to planar model predictions for static tests.

From this table, one observes that the shaft deflection at the hosel as predicted by the model lies within 0.15 inches of the measured deflection obtained from video. One error source arises from the limited resolution of the video. For instance, a one pixel error in locating points P1 or P1' in Fig. 5.7 translates to a displacement resolution error of approximately 0.09 inches. From Table 5.3, one also observes that the shaft rotation at the hosel as predicted by the model lies within about three degrees of that measured from video. In making these comparisons, however, one must understand the relatively poor resolution of θ_v from the video images. In particular, a 1 pixel error in locating either point P1 or P5 to define the tangent at the end of the shaft as shown in Fig. 5.7, leads to 4 degree error in the measured value of θ_v. Thus the video images, while convenient, have limited resolution in achieving more-refined comparisons with the model. Nevertheless, the generally good agreement observable in the data of Table 5.3 clearly suggests that the model can be used to estimate the static deflection of the club.

An alternative method for determining *EI* was explored whereby, a small portion of the grip end of the shaft was clamped with the shaft horizontal and then a series of weights

were hung at the opposite end of the shaft to generate lateral deflections under a known tip loads. The tip deflections so measured can be used to determined the average flexural rigidity of the shaft. From the classical result for a cantilever beam with constant cross-section the relationship between EI and the deflection at L is given by [37]

$$v\big|_L = \frac{FL^3}{3EI} \quad \text{or} \quad EI = \frac{FL^3}{3v\big|_L} \tag{5.2.8}$$

However this procedure did not yield any better results than determining EI from the static video tests as described above.

Test 2: Validation of Fundamental Natural Frequency

A logical next step in validating the model is to compare the predicted fundamental natural frequency of the assembled club with that measured in the laboratory. The free response form of equations (5.1.18) is found by setting the excitation terms $\left(\omega_y, \dot{\omega}_y, v_x, \dot{v}_x, v_z, \dot{v}_z\right)$ to zero. Doing so leads to

$$\begin{bmatrix} m & mz_c \\ mz_c & I_{zz} + mx_c^2 + mz_c^2 \end{bmatrix} \begin{bmatrix} \ddot{\delta}_v \\ \ddot{\theta}_v \end{bmatrix} + \begin{bmatrix} \dfrac{12EI}{L^3} & -\dfrac{6EI}{L^2} \\ -\dfrac{6EI}{L^2} & \dfrac{4EI}{L} \end{bmatrix} \begin{bmatrix} \delta_v \\ \theta_v \end{bmatrix} = \begin{bmatrix} mg\cos\theta_s \\ -mg\left(x_c\cos\theta_s - z_c\sin\theta_s\right) \end{bmatrix} \tag{5.2.9}$$

from which the natural frequencies can be calculated by considering perturbations about the static equilibrium. Equation (5.2.9) is of the form $\underline{M}\ddot{x} + \underline{K}x = \underline{F}$. The static equilibrium, $x = x^*$, satisfies $\underline{K}x^* = \underline{F}$. Considering perturbations of the form $x(t) = x^* + \Delta x(t)$, reduces (5.2.9) to

$$\begin{pmatrix} \Delta\ddot{v}_h \\ \Delta\ddot{\theta}_{\%_s} \end{pmatrix} + \underline{M}^{-1}\underline{K}\begin{pmatrix} \Delta v_h \\ \Delta\theta_{\%_s} \end{pmatrix} = \begin{pmatrix} 0 \\ 0 \end{pmatrix} \tag{5.2.10}$$

To find the natural frequencies, we seek solutions of the form

$$\begin{pmatrix} \Delta v_h \\ \Delta\theta_{\%_s} \end{pmatrix} = \underset{\sim}{X}e^{i\omega t} \tag{5.2.11}$$

which leads to the elementary eigenvalue problem

$$\left(\underline{M}^{-1}\underline{K}\right)\underset{\sim}{X} = \omega^2 \underset{\sim}{X} \tag{5.2.12}$$

Employing the model parameters listed in Table 5.1, the fundamental natural frequency computed from the above eigenvalue problem is 1.39 Hz. The natural frequency was then experimentally measured by clamping the club with the shaft approximately aligned with vertical ($\theta_s = 90°$), deflecting the club head and then allowing the club to vibrate freely. The frequency of this free vibration was measured by a MEMS accelerometer to be 1.30 Hz. Thus, model slightly over-predicts (+7% error) the fundamental natural frequency which could derive from an overestimate of the equivalent (averaged) value for *EI*. Part of this error is also likely to arise from clamping the shaft which necessarily shortens (hence stiffness) the shaft relative to the model. The error could also be caused by approximating the actual tapered shaft with a constant cross-section model. However, the overall good agreement clearly shows that the model adequately describes the free vibration characteristics of the club.

Test 3: Validation of Deflection under Measured Acceleration

A standard video camera was again used to measure the motion of the shaft under 'forced' conditions wherein the grip was swung (i.e., accelerated). The camera was oriented so that the optical axis was approximately perpendicular to the plane of motion of the club. We then provided a planar acceleration to the club (with large aluminum block) which caused significant flexing of the shaft over a long enough time period that the video camera could capture the resulting motion. The swing was also measured by the MEMS sensor which measures the full 3D rigid body motion of the grip. The sensor measurements in the $\left(\hat{i}_s, \hat{k}_s \right)$ plane were extracted from the data and used as input to the planar model. The output of this model was then directly compared to the video measurements as summarized below.

The first step in making a comparison between experiment and theory was to compare the rigid body motion of the club measured by the MEMS sensor system to that estimated from video. In particular, we used the MEMS sensor to compute the angle θ_s illustrated in Fig. 5.7 at the time of maximum deflection and then compared this computed angle to

107

that measured from video. The results for six representative trials are reported in Table 5.4.

Trial	Sensor Time	Video Frame	Video max θ_s (deg)	MEMS max θ_s (deg)	Error (deg)
Long Pointer 2	2.356	306	23.5	23.1	0.4
Long Pointer 3	2.780	533	22.4	20.8	1.6
Long Pointer 4	2.853	257	19.2	19.0	0.2
Short Pointer 1	1.928	350	27.9	28.8	-0.9
Short Pointer 2	2.073	301	26.8	29.5	-2.7
Short Pointer 3	2.245	305	24.9	25.4	-0.5

Table 5.4: Comparison of rigid body dynamics from video and MEMS sensor.

Inspection of this table reveals good agreement between the predicted orientation of the grip and that measured from the video. The agreement is most often within one degree which perhaps is not unexpected given the known accuracy of the MEMS sensor system from the more refined validation testing discussed in Chapter 2.

A similar procedure was then used to compare the flexible body motion predicted by the planar model with direct measurements from video. Table 5.5 summarizes the results for nine trials.

Trial	δ_v Video (in)	δ_v Model (in)	Error (in)	θ_v Video (deg)	θ_v Model (deg)	Error (deg)
Long Pointer 2 F 286	2.32	1.87	0.45	0.1	3.6	-3.5
Long Pointer 2 F 290	1.75	1.74	0.01	4.1	3.4	0.7
Long Pointer 3 F 514	2.52	2.05	0.47	0.2	4.0	-3.8
Long Pointer 3 F 518	2.21	1.78	0.43	3.9	3.5	0.4
Long Pointer 4 F 261	2.30	1.90	0.40	1.0	3.7	-3.7
Long Pointer 4 F 267	1.84	1.46	0.38	1.1	2.9	-1.8
Short Pointer 1 F 334	2.27	2.30	-0.03	5.6	4.5	1.1
Short Pointer 2 F 282	1.67	1.94	-0.27	4.2	3.8	0.4
Short Pointer 3 F 291	2.51	1.95	0.56	8.1	3.8	4.3

Table 5.5: Comparison of flexible body dynamics from video and planar model

The generalized coordinates (δ_v and θ_v) as calculated from video analysis and from the flexible model are reported in the table above at the time when the maximum deflection was noted in the video. (There were two distinct frames in the 'long pointer' trials where δ_v appeared to be a local maximum, so both times where analyzed.) As in the static tests, a 1 pixel difference in determining θ_v from the video leads to a 4 degree change in this angle, so the errors in θ_v noted in this table generally fall well within this limit of angular resolution from video. The resolution on deflection by video is again 0.09 inches per pixel. The errors however are generally greater than this resolution limit and the planar model nearly always under-predicts the shaft deflection. One possible source of this error may well be the unknown damping present in the shaft as described next.

Recall that the derivation of the planar model ignores dissipation. However, in the simulations leading to the results of Table 5.5, dissipation was incorporated by adding a linear damping term to both equations of motion. Specifically a terms proportional to $\dot{\delta}_v$ and $\dot{\theta}_v$ were added to (5.1.18). While the damping constants for these terms are not known *apriori*, one could tune them and doing so does alter the results reported above for the transient response of the club. Such tuning may well improve the agreement between the measured results and the planar model.

5.3 Closure

The purpose of this chapter was to demonstrate that a model of the golf club could be used in tandem with the measured motion of the grip to deduce the total (rigid + flexible) motion of the club head. The results presented herein suggest this to be true beginning with the conceptually simpler case of planar dynamics. The planar model rather accurately predicts the static deflection of the club head and the natural frequency of the shaft/club head system. In response to a swing (measured acceleration of grip), the same model provides reasonable estimates of the deflection of the club head that are largely within the (somewhat crude) resolution limits of standard video.

Given these initial results for *planar* dynamics, we extend the approach in Chapter 6 to describe the *three-dimensional* dynamics of a flexible golf club. In particular, Chapter 6 includes bending about two orthogonal axes of the shaft and twisting about the long axis of the shaft.

CHAPTER 6

THREE-DIMENSIONAL FLEXIBLE MODEL
OF A GOLF CLUB

The objective of this chapter is to extend the model derived in Chapter 5 to fully three-dimensional golf swings. This model will therefore account for shaft bending about two orthogonal axes and torsion about the centerline. The bending and torsion of the shaft are 'driven' by the acceleration (linear and angular) developed at the grip. Recall that the MEMS sensor system provides measurements of this 'input' and thus it can be used in conjunction with this flexible club model to predict the position and orientation of the club head due to both rigid and flexible body contributions. In addition, this chapter includes a limited validation study where predictions of the three-dimensional flexible model are compared with experimental observations from video.

6.1 Derivation of 3D Model (Lagrange Formulation)

Definition of Model and Unknowns

To begin, we introduce the golf club in three-dimensional space as illustrated in Fig. 6.1. This figure depicts the club with the shaft flexed (dashed line). As in the previous chapter, the shaft will be treated as a massless, inextensible, Euler-Bernoulli beam of length L and the club head will be considered a rigid body of mass m. Justification for the use of Euler-Bernoulli assumptions were given in Chapter 5.
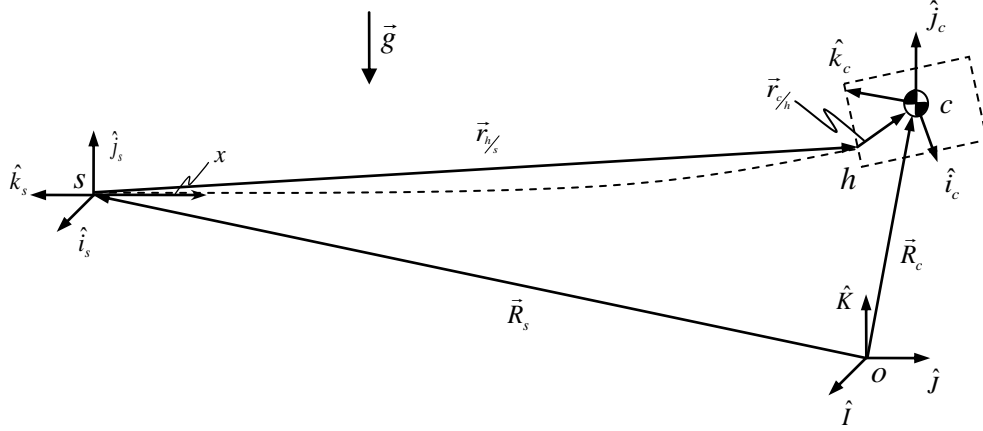
Figure 6.1: Schematic of 3D model. Points s, h and c denote the origin of the shaft frame, the hosel (point of intersection of shaft and club head), and the mass center of the club head, respectively. Dashed line represents the deflected shaft. The position vectors $\vec{R}_s$ and $\vec{R}_c$ are measured in the lab-fixed frame $\left(\hat{I},\hat{J},\hat{K}\right)$ whereas the position vectors $\vec{r}_{h/s}$ and $\vec{r}_{c/h}$ are measured in the body-fixed frame $\left(\hat{i}_s,\hat{j}_s,\hat{k}_s\right)$.

Three coordinate systems are introduced with analogous definitions to those for the two-dimensional model. The lab-fixed frame $\left(\hat{I},\hat{J},\hat{K}\right)$, is centered at point o with $\hat{K}$ aligned with the vertical direction $\left(\vec{g}=-g\hat{K}\right)$. The body-fixed frame $\left(\hat{i}_s,\hat{j}_s,\hat{k}_s\right)$, is centered at point s where the $\hat{k}_s$ direction is tangent to the *undeformed* or rigid shaft and $\left(\hat{i}_s,\hat{j}_s\right)$ are in the directions normal to the rigid shaft. The body-fixed frame $\left(\hat{i}_c,\hat{j}_c,\hat{k}_c\right)$ is centered at c with the $\hat{k}_c$ direction tangent to the *deformed* or flexible shaft and $\left(\hat{i}_c,\hat{j}_c\right)$ are normal directions to the flexible shaft. The position vectors $\vec{R}_s$ and $\vec{R}_c$ define the position of the shaft (grip) and the mass center of the club head respectively, as measured in the lab-fixed frame. The position vector $\vec{r}_{h/s}$ is measured in the body-fixed s-frame and the position vector $\vec{r}_{c/h}$ is measured in the vector body-fixed c-frame.

Deflection of the shaft in the $\left(\hat{i}_s,\hat{k}_s\right)$ plane will be described with the variable $\upsilon(x,t)$ where x is the independent spatial coordinate measured along the undeformed shaft from

s towards *h*. In the orthogonal plane, $\left(\hat{j}_s, \hat{k}_s \right)$ plane, deflection of the shaft is assigned the variable $w(x,t)$. Twisting of the shaft about the $\hat{k}_s$ direction is denoted by the variable $\psi(x,t)$.

For the three-dimensional problem, five generalized coordinates (5 degrees-of-freedom) are required to describe the flexible body dynamics of the club head relative to the rigid shaft. (The sixth dof is eliminated due to the assumption of inextensibility.) The deflection of the shaft at point *h* in the $\left(\hat{i}_s, \hat{k}_s \right)$ plane is denoted by δ_v (the deflection at the hosel) and the slope of the shaft at this same point *h* is denoted as θ_v (the rotation of the deformed shaft relative to the undeformed shaft at the hosel). These quantities are identical to those introduced in the two-dimensional model. Counter-clockwise (CCW) rotation of the deformed shaft relative to the undeformed shaft is defined to be positive about the $-\hat{j}_s$ direction. The analogous definitions for the displacement and slope at the hosel in the $\left(\hat{j}_s, \hat{k}_s \right)$ plane lead to the coordinates δ_w and θ_w, respectively. For θ_w, the positive sign convention is defined as CCW rotation about the $\hat{i}_s$ direction of the deformed shaft relative to the undeformed shaft. The twist of the shaft at point h relative to point *s* is defined as the coordinate ψ_h. Positive twist is defined as CCW twisting about the $-\hat{k}_s$.

We now turn attention to developing the equations of motion of our five dof model using a Lagrangian formulation. The major steps of the derivation are summarized below and the final linear equations of motion are provided in full in Appendix A.

Potential Energy

Using the definitions of the generalized coordinates above, we first develop expressions for the strain energy and gravitational potential energy which constitute the potential

energy for our five dof model. The boundary conditions are the same as in the two-dimensional model. The left boundary is equivalent to a 'clamped' boundary condition and the right boundary conditions are the deflections and rotations described by the generalized coordinates. The bending strain energy for bending in the $\left(\hat{i}_s, \hat{k}_s\right)$ plane is the same as the previous chapter Eqn. (5.1.10) as given by

$$V_{ik\_bend} = \frac{2EI\left(3\delta_v^2 - 3L\theta_v\delta_v + L^2\theta_v^2\right)}{L^3}$$

(5.1.10)

Similarly, the bending strain energy for bending in the $\left(\hat{j}_s, \hat{k}_s\right)$ plane is

$$V_{jk\_bend} = \frac{2EI\left(3\delta_w^2 - 3L\theta_w\delta_w + L^2\theta_w^2\right)}{L^3}$$

(6.1.1)

Next, we describe the twisting of the shaft, $\psi(x,t)$, wholly in terms of the generalized coordinate ψ_h. Fig. 6.2 shows an image of the cantilevered shaft with circular cross-section subject to a torque, T, which is the reaction torque from the club head on the shaft.
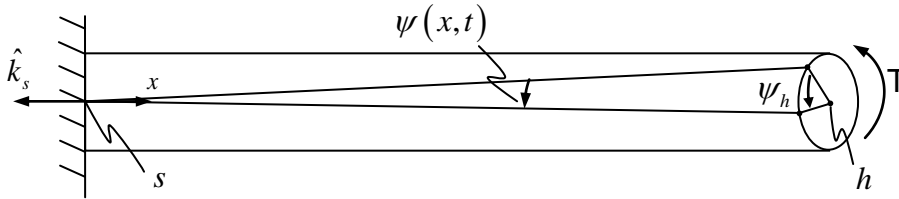
Figure 6.2: Cantilevered Euler-Bernoulli beam subject to torque T applied at the end.

Considering the equilibrium of an infinitesimal section of length dx, the differential equation of equilibrium for torsion is

$$GJ\psi'' = 0$$

(6.1.2)

when no distributed torque is present [51] and GJ denotes the shaft torsional stiffness. Therefore ψ' is a constant. Applying the boundary condition, $\psi(0) = 0$ leads to the classical result

$$\psi(x) = \frac{T}{GJ}x \qquad (6.1.3)$$

for ψ as a function of x. The twist at the end of the shaft is

$$\psi(L) = \psi_h = \frac{TL}{GJ} \qquad (6.1.4)$$

Solving (6.1.4) for T and substituting into (6.1.3) yields the shaft twist

$$\psi(x) = \frac{\psi_h}{L}x \qquad (6.1.5)$$

as a function of x and the generalized coordinate ψ_h. The strain energy for the shaft due to torsion is

$$V_{tor} = \frac{GJ}{2}\int_0^L \left(\frac{\partial \psi(x,t)}{\partial x}\right)^2 dx$$
$$= \frac{GJ}{2L}\psi_h^2 \qquad (6.1.6)$$

where Eqn. (6.1.5) has been substituted [51].

Summing all the terms associated with strain energy yields the result

$$V_{strain} = \frac{2EI}{L^3}\left(3\delta_v^2 - 3L\delta_v\theta_v^2 + L^2\theta_v^2 + 3\delta_w^2 - 3L\delta_w\theta_w^2 + L^2\theta_w^2\right) + \frac{GJ}{2L}\psi_h^2 \qquad (6.1.7)$$

The remaining potential energy derives from gravity and is given by

$$V_{grav} = mgZ \qquad (6.1.8)$$

where m is the mass of the club head, g is the acceleration due to gravity, and Z is the $\hat{K}$ component of the position vector $\vec{R}_c$, refer to Fig. 6.1. The expansion for $\vec{R}_c$ will be developed below in the derivation of the kinetic energy. Combining the strain energy, (6.1.7), and the gravitational potential energy, (6.1.8), yields the total potential energy for the model.

Kinetic Energy

Just as in the two-dimensional case, we formulate the kinetic energy of the club head. In three-dimensions, the kinetic energy of this rigid body is

$$T = \frac{1}{2} m \vec{v}_c^T \vec{v}_c + \frac{1}{2} \vec{\omega}_c^T \underline{I}_c \vec{\omega}_c \qquad (6.1.9)$$

where $\vec{v}_c$ is the absolute velocity of mass center, c, $\vec{\omega}_c$ is the absolute angular velocity of the club head (hence the angular velocity of the body-fixed frame at c), and $\underline{I}_c$ is the inertia tensor defined by the body-fixed frame at the mass center, c.

Beginning with the translational component of the kinetic energy, the velocity vector $\vec{v}_c$ can be expanded as

$$\vec{v}_c = \vec{v}_h + \vec{\omega}_c \times \vec{r}_{c/h} \qquad (6.1.10)$$

where $\vec{v}_h$ is the absolute velocity of hosel (point h) and $\vec{r}_{c/h}$ is the position of c relative to h. This position vector is a function of the club head geometry and is constant when written in the $\left(\hat{i}_c, \hat{j}_c, \hat{k}_c \right)$ frame as

$$\vec{r}_{c/h} = x_c \hat{i}_c + y_c \hat{j}_c - z_c \hat{k}_c \qquad (6.1.11)$$

The velocity of the hosel can also be expanded as

$$\vec{v}_h = \vec{v}_s + \vec{v}_{h/s} + \vec{\omega}_s \times \vec{r}_{h/s} \qquad (6.1.12)$$

where $\vec{v}_s$ is absolute velocity of sensor origin (point s) which is derived from measurements as detailed in Chapter 2. The velocity vector $\vec{v}_{h/s}$ is the velocity of point h relative to point s. The third term of this expression contains $\vec{\omega}_s$ which is the absolute angular velocity of the body-fixed reference frame at s, which is again derived from measurement. The vector $\vec{r}_{h/s}$ is the position of point h relative to point s. This position can be written as

$$\vec{r}_{h/s} = \delta_v \hat{i}_s + \delta_w \hat{j}_s - L \hat{k}_s \qquad (6.1.13)$$

using the definitions of the generalized coordinates introduced at the beginning of the chapter. The time derivative of Eqn. (6.1.13) leads to an expression for $\vec{v}_{h/s}$ as

$$\vec{v}_{h/s} = \dot{\delta}_v \hat{i}_s + \dot{\delta}_w \hat{j}_s \tag{6.1.14}$$

Return to equation (6.1.10) and expand $\vec{\omega}_c$ as

$$\vec{\omega}_c = \vec{\omega}_s + \vec{\omega}_{c/s} \tag{6.1.15}$$

where $\vec{\omega}_{c/s}$ is the angular velocity of the c-frame relative to the s-frame. That relative angular velocity can also be expressed in terms of the generalized coordinates per

$$\vec{\omega}_{c/s} = \dot{\theta}_w \hat{i}_s - \dot{\theta}_v \hat{j}_s - \dot{\psi}_h \hat{k}_s \tag{6.1.16}$$

The signs of the terms above reflect the sign conventions for positive rotations introduced previously.

To develop a full expression for the translational kinetic energy all vectors will first be transformed into components in the $\left(\hat{i}_s, \hat{j}_s, \hat{k}_s \right)$ frame. The transformation from the shaft frame, $\left(\hat{i}_s, \hat{j}_s, \hat{k}_s \right)$, to the club head frame, $\left(\hat{i}_c, \hat{j}_c, \hat{k}_c \right)$, can be written as [43]

$$^cC^s = \begin{bmatrix} \cos\theta_2 \cos\theta_3 & \sin\theta_3 \cos\theta_2 & -\sin\theta_2 \\ \sin\theta_1 \sin\theta_2 \cos\theta_3 - \cos\theta_1 \sin\theta_3 & \cos\theta_3 \cos\theta_1 + \sin\theta_3 \sin\theta_1 \sin\theta_2 & \sin\theta_1 \cos\theta_2 \\ \sin\theta_3 \sin\theta_1 + \cos\theta_1 \sin\theta_2 \cos\theta_3 & \sin\theta_3 \sin\theta_2 \cos\theta_1 - \cos\theta_3 \sin\theta_1 & \cos\theta_1 \cos\theta_2 \end{bmatrix} \tag{6.1.17}$$

where $\left(\theta_1, \theta_2, \theta_3 \right)$ are three successive CCW rotations about the positive $\left(\hat{i}_s, \hat{j}_s, \hat{k}_s \right)$ axes, respectively. The (Euler) angles $\left(\theta_1, \theta_2, \theta_3 \right)$ are related to the generalized coordinates $\left(\theta_w, \theta_v, \psi_h \right)$ by the following

$$\begin{aligned} \theta_1 &= \theta_w \\ \theta_2 &= -\theta_v \\ \theta_3 &= -\psi_h \end{aligned} \tag{6.1.18}$$

Substituting Eqn. (6.1.18) into the transformation matrix (6.1.17) yields

$$^cC^s = \begin{bmatrix} 1 & -\psi_h & \theta_v \\ -\theta_w \theta_v + \psi_h & 1 + \theta_w \theta_v \psi_h & \theta_w \\ -\psi_h \theta_w - \theta_v & \theta_v \psi_h - \theta_w & 1 \end{bmatrix} \tag{6.1.19}$$

where $\sin\theta = \theta$ and $\cos\theta = 1$ are used in keeping with the kinematic assumption of (small rotation) Euler-Bernoulli beam theory. In addition, only terms of second order or lower will be retained in (6.1.19) as only these terms will contribute toward the linear equations of motion in the end. In other words, terms up to second order in the kinetic energy yield the first order terms in the equations of motion. The final expression for $\vec{v}_c$ is

$$\vec{v}_c = \vec{v}_s + \vec{v}_{b/s} + \vec{\omega}_s \times \vec{r}_{b/s} + \left(\vec{\omega}_s + \vec{\omega}_{c/s}\right) \times {}^sC^c \vec{r}_{/h} \tag{6.1.20}$$

Continuing on, we now focus on the rotational portion of the kinetic energy, $T_{rot} = \dfrac{1}{2}\vec{\omega}_c^T \underline{I_c}\vec{\omega}_c$, realizing that $\vec{\omega}_c$ has already been defined in the s-frame above and $\underline{I_c}$ is constant in the c-frame. Transforming $\underline{I_c}$ to the s-frame leads to the final expression

$$T_{rot} = \frac{1}{2}\vec{\omega}_c^T \left({}^sC^c\right)^T \underline{I_c}\left({}^sC^c\right)\vec{\omega}_c \tag{6.1.21}$$

for the rotational kinetic energy.

Having established the kinematic relations above, we now return to the missing part of the potential energy formulation that relies on formulating an expression for the position vector $\vec{R}_c$. Notice that

$$\vec{R}_c = \vec{R}_s + {}^LC^s\left(\vec{r}_{b/s} + {}^sC^c\vec{r}_{/h}\right) \tag{6.1.22}$$

where ${}^LC^s$ is the transformation from the s-frame to the lab-fixed frame $\left(\hat{I},\hat{J},\hat{K}\right)$ as introduced in Chapter 2, and where ${}^sC^c = \left({}^cC^s\right)^T$. The $\hat{K}$ component of this vector, namely Z, is needed for the gravitational potential energy Eqn. (6.1.8).

Linear Equations of Motion

With complete expressions for the potential and kinetic energies, we turn our attention obtaining the five equations of motion via Lagrange's equations as follows

$$\frac{d}{dt}\left(\frac{\partial T}{\partial \dot{q}_i}\right) - \frac{\partial T}{\partial q_i} + \frac{\partial \left(V_{strain} + V_{grav}\right)}{\partial q_i} = 0 \quad i = 1, 2, 3, 4, 5 \tag{6.1.23}$$

The quantities q_i denote the generalized coordinates $\left(\delta_v, \delta_w, \theta_v, \theta_w, \psi_h\right)$. In formulating these equations, we retaining only the linear terms in the generalized coordinates which leads to a system of linear differential equations of the form

$$\underline{M}\ddot{\vec{q}} + \underline{C}\dot{\vec{q}} + \underline{K}\vec{q} = \tilde{F} \tag{6.1.24}$$

The complete form of Eqn. (6.1.24) is provided in Appendix A.

6.2 Experimental Validation

We present next a limited set of experiments that were used to validate the three-dimensional model for a flexible golf club outlined above. The experiments follow closely those performed for the two-dimensional model of Chapter 5. Due to limited time, these experiments are not exhaustive, but they do offer some validation of both the natural frequencies of the flexible club as well as transient dynamics during a controlled swing.

Natural Frequencies of Club

Experimental results for the two-dimensional model of Chapter 5 already considered the natural frequency for shaft bending in a single plane. The two-dimensional model provided a very reasonable estimate for this natural frequency. The model parameters given in Table 5.1 were used as inputs for both bending axes in the three-dimensional model. A similar eigenvalue problem to that described by Eqs. 5.2.9 to 5.2.12 was analyzed for the 3-D model resulting in the prediction of the two bending natural

frequencies as 1.39 Hz which shows that the bending natural frequencies for the 3-D model converge to that of the 2-D model (1.39 Hz from 2-D model).

A new feature of the three-dimensional model is that it explicitly accounts for the torsion of the shaft. Thus, one could now use a measured torsional natural frequency of the club to provide further validation of the three-dimensional model. To this end, the torsional natural frequency of the same exaggerated club introduced in the previous chapter was measured by clamping the grip end of the shaft, applying a torque to the aluminum block club head, and then allowing the system to vibrate freely. From the recorded free response, this natural frequency was measured to be 14.4 Hz. A similar eigenvalue problem to the one considered in (5.2.12) was constructed for the three-dimensional model. The eigenvalue problem for torsion upon substituting the club properties is given as

$$I_{zz}\ddot{\psi}_h + K_{tor}\psi_h = 0$$
$$\text{where } K_{tor} = \frac{GJ}{L}$$

(6.2.1)

The model parameters detailed in Table 5.1 were used as input to this eigenvalue problem together with the following estimate of GJ

$$GJ = \frac{EI}{(1+v)} = 146\left(lbf \cdot ft^2\right)$$
$$v = 0.29 \text{ for steel}$$

(6.2.2)

obtained by relating the previously measured bending stiffness (EI) to the torsional stiffness (GJ) of a circular shaft. Doing so leads a predicted value of the torsional natural frequency as 23.3 Hz. This is a 62% error in predicting the torsional natural frequency. The main cause of this discrepancy is the assumption that the shaft can be model as a constant cross-section. Revisiting Eq. (6.1.2) and allowing J to vary along the length of the shaft results in the boundary value problem

$$GJ(x)\psi^{''} = 0$$
$$\psi(0) = 0 \text{ and } \psi(L) = \psi_h$$

(6.2.3)

The solution of (6.2.3), separating the variables, leads to

$$GJ(x)d\psi = Tdx$$

(6.2.4)

Next we assume that the shaft tapers linearly from an outer diameter of D_1 at $x = 0$ to an outer diameter of D_2 at $x = L$ and that the shaft has a constant thickness of t. Therefore $J(x)$ can be approximated by the function

$$J(x) = \frac{\pi}{32}\left(\left(D_1 + (D_2 - D_1)\frac{x}{L}\right)^4 - \left(D_1 + (D_2 - D_1)\frac{x}{L} - 2t\right)^4\right)$$ (6.2.5)

The parameters D_1, D_2, and t for the measured club are $0.59in$, $0.34in$ and $0.02in$ respectively. Integrating the left hand side of Eq. (6.2.3) from 0 to ψ_h, the right hand side from 0 to L and substituting the known constants leads to

$$\psi_h = \frac{39883in^{-3} \cdot T}{G}$$ (6.2.6)

where G is the shear modulus of the shaft (steel). The twist at $x = L$, ψ_h, is related to the stiffness parameter K_{tor} by

$$K_{tor} = \frac{T}{\psi_h} = 24.2\,ft \cdot lb$$ (6.2.7)

Now we substitute the new value for K_{tor} into (6.2.1), which leads to a predicted natural frequency of 18.5 Hz. This reduces the natural frequency discrepancy to 28%. Further refinement of the torsional model could be accomplished by accounting for the fact that the actual shaft maintains the outer diameter of D_2 for approximately the last $9in$ of the $46in$ shaft and modeling the shaft in discrete sections since the real shaft is stepped. During so will ultimately reduce K_{tor} further and thus lower the predicted natural frequency.

Transient Response

The transient response of the two-dimensional model was validated by comparing the transient motion measured by standard video to the model predictions. The model predictions used the measured sensor data for a simple swing (slow slewing motion) that was largely confined to the vertical plane. Only the associated two-dimensional

components of the measured sensor data were used for validation of the two-dimensional model.

Here, we return to that same experiment but now include the complete three-dimensional components of the measured sensor data as input to the three-dimensional model. Again we add in dissipation terms proportional to the generalized velocities as we did in the 2D model simulation. Our expectation is that the three-dimensional model will largely replicate the results of the two-dimensional model but that there should also be torsional and out-of-plane bending components that are excited during the experiment. The computed output of the three-dimensional model is presented below.
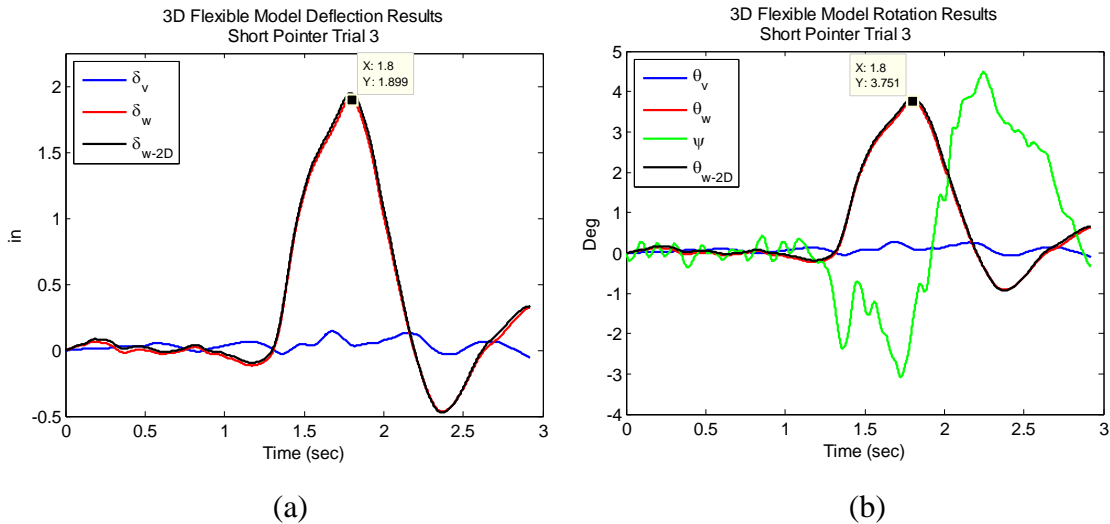
Figure 6.3: Simulation results of three-dimensional flexible shaft model using measured input from MEMS sensor system. This test is described in Chapter 5. (a) Computed time histories of the two displacement coordinates, δ_v and δ_w. (b) Computed time histories of the three rotation coordinates, θ_v, θ_w, and ψ_h. The results from the 2D model are superimposed in black.

Figure 6.3 illustrates the time histories for the five generalized coordinates computed for the slow 'slewing' experiment of the club previously described in Chapter 5. The red curves of Fig. 6.3, which represent the two "in-plane" degrees-of-freedom, are nearly identical to those computed for the two-dimensional model (black curves). (Minute difference do exist due to the coupling terms with the out-of-plane motion components in

the equations of motion for the three-dimensional model.) The two data points illustrated in Figs. 6.3(a)-(b) designate the maximum in-plane displacement and rotation of the club head as predicted by the three-dimensional model. These values closely reproduce those of the two-dimensional model which correlate reasonably well with those measured via video as described in Chapter 5. The out-of-plane bending and rotation components (blue curves) comparably small indicating that the club motion is indeed largely planar as expected. The torsional motion, though clearly excited, is also reasonably small (never exceeding 4.5 degrees) and it also clearly shows oscillations in response to inadvertent torque inputs applied to the shaft during the experiment. Unfortunately, there was no means to detect/measure these small torsional motions via the video camera.

6.3 Closure

This chapter provides an important extension of the results of Chapter 5. In particular, we derive a five degree-of-freedom model that describes the three-dimensional flexible body dynamics of a golf club. The model captures the two-axis bending of the shaft as well as the twisting of the shaft. These bending and twisting motions are ultimately induced by the golfer through linear and angular accelerations developed at the grip during the swing. The MEMS sensor system allows one to measure these 'inputs' to the flexible body motion. A limited amount of experimental validation is also presented in this chapter which includes analyses of the natural frequencies of a club in torsion and the transient response of a club in a slow slewing motion. Additional validation is recommended in the future by employing golf clubs with embedded strain gauges and/or through a refined analysis of high-speed video/motion capture cameras.

Overall, the flexible body modeling efforts described in Chapters 5 and 6 add new capabilities to the original use of the MEMS sensor system as a means to track the rigid body dynamics of the club. The two- and three-dimensional models of a flexible club require *apriori* knowledge of a limited number of club parameters that describe the shaft geometry and stiffness (in both bending and torsion) and the geometry and inertia properties (mass and inertia tensor) of the club head. Once these parameters are specified, they are used to define a flexible body model of the golf club that enables the prediction

of the overall motion of the club (both rigid and flexible motions components) based on the measured motion components from the MEMS sensor system.

CHAPTER 7

CONTRIBUTIONS, CONCLUSIONS
AND FUTURE DIRECTIONS

7.1 Contributions and Conclusions

Overall, this research contributes a novel technology for measuring the three-dimensional motion of a golf club that is highly portable and far less expensive when compared to state-of-the-art camera based measurement systems. The marrying of MEMS inertial sensors with a wireless transceiver yields a compact and lightweight design that fits wholly within the grip end of the club. The broad uses of this technology include golf swing training, golf club design, and custom golf club fitting. We summarize briefly below four major outcomes.

The first major outcome of this research is the design, fabrication and testing of a novel, miniature, wireless, six degree-of-freedom, inertial measurement unit (IMU) for measuring the rigid body dynamics of a golf club. A second major outcome is the development of a companion measurement theory that uses the sensor acceleration and angular velocity signals to compute the three-dimensional kinematics of a golf club including the club head path and velocity, and the club head orientation (lie, loft and face angles). A third major outcome is the use of the hardware and measurement theory to understand the major features of putting strokes and full swings. Finally, a fourth major outcome is the prediction of flexible body motion using measured sensor signals as input to flexible golf club models. The application of this sensor hardware and measurement theory leads to the following conclusions for golf swing dynamics.

The systematic evaluation of putting strokes with a putting robot demonstrates that one can predict the three-dimensional position of the club head to within 3mm and the

orientation of the club head (lie, loft and face angles) to within 0.5°, all with millisecond updates. An in depth study of putting techniques also reveals that this technology can pin-point common putting faults including, for example, 1) excessive face angles at impact, 2) off-center impacts of the ball on the clubface, and 3) improper uses of the wrists. A second-generation design that incorporates higher-range sensors allows the concept to be extended to full swings. The analysis of swings made with irons and drivers readily distinguishes important features within the three major phases of a full swing; namely, the address, the backswing, and the downswing. For example, both the backswing and the downswing are largely confined to distinct swing planes and the orientation of these two planes can be calculated from the sensor data. The significant linear and angular accelerations developed at the grip during the final stage of the downswing may induce flexible body motion of the club. Both two- and three-dimensional models describing the bending and twisting of the shaft are derived to estimate these flexible body components. The MEMS sensor system provides the essential inputs to these models thereby allowing one to incorporate flexible body influences with no additional sensors/instrumentation.

7.2 Future Directions

This research has laid the foundation for the application of MEMS inertial sensor technology to the analysis and teaching of golf swings. However, it is important to recognize that success in golf follows from a combination of skills, including developing highly effective swing mechanics. For example, success in putting requires that a player correctly read the green, align to the intended target line, and then finally execute an accurate stroke. In this context, this technology provides a truly superior means for assessing the latter skill, namely the development of an effective putting stroke. Indeed, the studies included in Chapter 3 provide compelling evidence that this technology can pin-point common faults in the putting stroke through systematic analysis of the club head position and orientation. Of course one way to remedy any fault is through concerted practice with specific and timely feedback. In some instances and alternative may be to alter the club characteristics to minimize the fault leading to the

concept of custom club fitting. In either instance, this technology provides the essential measurement hardware and analysis theory to guide and to track improvements.

Additional research and development is now necessary to improve the analysis of full golf swings. In particular, the need exists to precisely identify the first instance of ball/club impact as input to the analysis of full swings. A second area of improvement lies with the identification and systematic correction of measurement errors, including sensor bias error. Beyond these improvements in predicting the rigid body motion during full swings, one should focus on improving the predictions of the flexible body motion. Advances will follow from developing/using a fully instrumented golf club that senses strain and/or displacements for two-axis bending and torsion. These measurements will no doubt enable additional improvements to the three-dimensional model of a flexible club. A ready starting point would be to explicitly account for the taper of the shaft.

Despite these limitations, this research overall has contributed a promising technology to the advance the game of golf.

Appendix A: Three-Dimensional Model Equations

This appendix contains the full expression for all the terms of the 3D flexible model described in Chapter 6. The 3D model is of the form:

$$\underline{M}\ddot{\vec{q}} + \underline{C}\dot{\vec{q}} + \underline{K}\vec{q} = \vec{F}$$
$$\text{Where: } \vec{q} = (\delta_v, \delta_w, \theta_v, \theta_w, \psi_h)$$

Gerneralized Mass Matrix Terms

The following matrix is the generalized mass matrix:

$$\underline{M} = \begin{pmatrix} m & 0 & mz_c & 0 & my_c \\ 0 & m & 0 & mz_c & -mx_c \\ mz_c & 0 & mx_c^2 + mz_c^2 + \text{Iyy} & mx_cy_c & my_cz_c \\ 0 & mz_c & mx_cy_c & my_c^2 + mz_c^2 + \text{Ixx} & -mx_cz_c \\ my_c & -mx_c & my_cz_c & -mx_cz_c & mx_c^2 + my_c^2 + \text{Izz} \end{pmatrix}$$

Generalized Damping Matrix Terms

Here are the generalized damping trems:

$C11 = 0$

$C12 = -2m\omega_z(t)$

$C13 = 2mx_c\omega_y(t)$

$C14 = 2my_c\omega_y(t) - 2mz_c\omega_z(t)$

$C15 = 2mx_c\omega_z(t)$

$C21 = 2m\omega_z(t)$

$C22 = 0$

$C23 = 2mz_c\omega_z(t) - 2mx_c\omega_x(t)$

$C24 = -2my_c\omega_x(t)$

$C25 = 2my_c\omega_z(t)$

$C31 = -2mx_c\omega_y(t)$

$C32 = 2mx_c\omega_x(t) - 2mz_c\omega_z(t)$

$C33 = 0$

$C34 = m\omega_z(t)x_c^2 + m\mathrm{v}_y(t)x_c + Lm\omega_x(t)x_c + 3mz_c\omega_x(t)x_c - my_c\mathrm{v}_x(t) + Lmy_c\omega_y(t) + 3my_cz_c\omega_y(t) + my_c^2\omega_z(t) - 2mz_c^2\omega_z(t)$

$C35 = -2m\omega_x(t)x_c^2 - 3my_c\omega_y(t)x_c + 3mz_c\omega_z(t)x_c + mz_c\mathrm{v}_y(t) + my_c\mathrm{v}_z(t) + my_c^2\omega_x(t) + mz_c^2\omega_x(t) + Lmz_c\omega_x(t)$

$C41 = 2mz_c\omega_z(t) - 2my_c\omega_y(t)$

$C42 = 2my_c\omega_x(t)$

$C43 = -m\omega_z(t)x_c^2 - m\mathrm{v}_y(t)x_c - Lm\omega_x(t)x_c - 3mz_c\omega_x(t)x_c + my_c\mathrm{v}_x(t) - Lmy_c\omega_y(t) - 3my_cz_c\omega_y(t) - my_c^2\omega_z(t) + 2mz_c^2\omega_z(t)$

$C44 = 0$

$C45 = m\omega_y(t)x_c^2 - m\mathrm{v}_z(t)x_c - 3my_c\omega_x(t)x_c - mz_c\mathrm{v}_x(t) - 2my_c^2\omega_y(t) + mz_c^2\omega_y(t) + Lmz_c\omega_y(t) + 3my_cz_c\omega_z(t)$

$C51 = -2mx_c\omega_z(t)$

$C52 = -2my_c\omega_z(t)$

$C53 = 2m\omega_x(t)x_c^2 + 3my_c\omega_y(t)x_c - 3mz_c\omega_z(t)x_c - mz_c\mathrm{v}_y(t) - my_c\mathrm{v}_z(t) - my_c^2\omega_x(t) - mz_c^2\omega_x(t) - Lmz_c\omega_x(t)$

$C54 = -m\omega_y(t)x_c^2 + m\mathrm{v}_z(t)x_c + 3my_c\omega_x(t)x_c + mz_c\mathrm{v}_x(t) + 2my_c^2\omega_y(t) - mz_c^2\omega_y(t) - Lmz_c\omega_y(t) - 3my_cz_c\omega_z(t)$

$C55 = 0$

Generalized Stiffness Terms

Here are the generalized stiffness terms:

$K11 = -m\omega_y(t)^3 - m\omega_z(t)^2 + \frac{12EI}{L^3}$

$K12 = m\omega_x(t)\omega_y(t) - m\dot{\omega}_z(t)$

$K13 = -mz_c\omega_y(t)^2 - mz_c\omega_z(t)^2 + mx_c\omega_x(t)\omega_z(t) + mx_c\dot{\omega}_y(t) - \frac{6EI}{L^2}$

$K14 = mz_c\omega_x(t)\omega_y(t) + my_c\omega_x(t)\omega_z(t) + my_c\dot{\omega}_y(t) - mz_c\dot{\omega}_z(t)$

$K15 = -my_c\omega_y(t)^2 - mx_c\omega_x(t)\omega_y(t) - my_c\omega_z(t)^2 + mx_c\dot{\omega}_z(t)$

$K21 = m\omega_x(t)\omega_y(t) + m\dot{\omega}_z(t)$

$K22 = -m\omega_x(t)^2 - m\omega_z(t)^2 + \frac{12EI}{L^3}$

$K23 = mz_c\omega_x(t)\omega_y(t) + mx_c\omega_z(t)\omega_y(t) - mx_c\dot{\omega}_x(t) + mz_c\dot{\omega}_z(t)$

$K24 = -mz_c\omega_x(t)^2 - mz_c\omega_z(t)^2 + my_c\omega_y(t)\omega_z(t) - my_c\dot{\omega}_x(t) - \frac{6EI}{L^2}$

$K25 = mx_c\omega_x(t)^2 + my_c\omega_y(t)\omega_x(t) + mx_c\omega_z(t)^2 + my_c\dot{\omega}_z(t)$

$K31 = -mz_c\omega_y(t)^2 - mz_c\omega_z(t)^2 + mx_c\omega_x(t)\omega_z(t) - mx_c\dot{\omega}_y(t) - \frac{6EI}{L^2}$

$K32 = mz_c\omega_x(t)\omega_y(t) + mx_c\omega_z(t)\omega_y(t) + mx_c\dot{\omega}_x(t) - mz_c\dot{\omega}_z(t)$

$K33 = -mx_c^2\omega_x(t)^2 + 2Ixz\omega_z(t)\omega_x(t) + 2mx_cz_c\omega_z(t)\omega_x(t) - mx_c^2\omega_y(t)^2 - mz_c^2\omega_y(t)^2 - mz_c^2\omega_z(t)^2 - mx_c\dot{v}_x(t) + mz_c\dot{v}_z(t) + my_cz_c\dot{\omega}_x(t) + Lmx_c\dot{\omega}_y(t) + mx_cy_c\dot{\omega}_z(t) + \frac{4EI}{L}$

$K34 = -m\omega_x(t)\omega_y(t)y_c^2 + m\dot{\omega}_z(t)y_c^2 - mx_c\omega_x(t)^2y_c + mx_c\omega_z(t)^2y_c - 2gm(e_1e_3 - e_2e_4)y_c - mv_z(t)\omega_y(t)y_c + mv_y(t)\omega_z(t)y_c + Lm\omega_x(t)\omega_z(t)y_c + 2mz_c\omega_x(t)\omega_z(t)y_c - m\dot{v}_x(t)y_c + Lm\dot{\omega}_y(t)y_c + 2mz_c\dot{\omega}_y(t)y_c + mz_c^2\omega_x(t)\omega_y(t) + mx_cz_c\omega_y(t)\omega_z(t) + mx_cz_c\dot{\omega}_x(t) - mz_c^2\dot{\omega}_z(t)$

$K35 = -m\omega_y(t)\omega_z(t)x_c^2 - m\dot{\omega}_x(t)x_c^2 - 2mz_c\omega_x(t)\omega_y(t)x_c + my_c\omega_x(t)\omega_z(t)x_c - 2my_c\dot{\omega}_y(t)x_c + mz_c\dot{\omega}_z(t)x_c + my_cz_c\omega_x(t)^2 - my_cz_c\omega_y(t)^2 - 2gm(e_2e_3 + e_1e_4)z_c + mz_cv_z(t)\omega_x(t) - mz_cv_x(t)\omega_z(t) + mz_c^2\omega_y(t)\omega_z(t) + Lmz_c\omega_y(t)\omega_z(t) + my_c\dot{v}_z(t) + my_c^2\dot{\omega}_x(t)$

$K41 = mz_c\omega_x(t)\omega_y(t) + my_c\omega_x(t)\omega_z(t) - my_c\dot{\omega}_y(t) + mz_c\dot{\omega}_z(t)$

$K42 = -mz_c\omega_x(t)^2 - mz_c\omega_z(t)^2 + my_c\omega_y(t)\omega_z(t) + my_c\dot{\omega}_x(t) - \frac{6\text{EI}}{L^2}$

$K43 = -m\dot{\omega}_z(t)x_c^2 - my_c\omega_x(t)^2x_c + my_c\omega_z(t)^2x_c + mz_c\omega_y(t)\omega_z(t)x_c - m\dot{v}_y(t)x_c - Lm\dot{\omega}_x(t)x_c - 2mz_c\dot{\omega}_x(t)x_c - 2gm(e_1e_3 - e_2e_4)y_c - my_cv_z(t)\omega_y(t) - my_c^2\omega_x(t)\omega_y(t) + mz_c^2\omega_x(t)\omega_y(t) + my_cv_y(t)\omega_z(t) + Lmy_c\omega_x(t)\omega_z(t) + 2my_cz_c\omega_x(t)\omega_z(t) - my_cz_c\dot{\omega}_y(t) + mz_c^2\dot{\omega}_z(t)$

$K44 = -my_c^2\omega_x(t)^2 - mz_c^2\omega_x(t)^2 - my_c^2\omega_y(t)^2 - mz_c^2\omega_z(t)^2 + 2\text{Iyz}\omega_y(t)\omega_z(t)$
$+2my_cz_c\omega_y(t)\omega_z(t) - my_c\dot{v}_y(t) + mz_c\dot{v}_z(t) - Lmy_c\dot{\omega}_x(t) - mx_cz_c\dot{\omega}_y(t) - mx_cy_c\dot{\omega}_z(t) + \frac{4\text{EI}}{L}$

$K45 = m\dot{\omega}_y(t)x_c^2 + mz_c\omega_x(t)^2x_c - mz_c\omega_y(t)^2x_c - my_c\omega_y(t)\omega_z(t)x_c - m\dot{v}_z(t)x_c$
$-2my_c\dot{\omega}_x(t)x_c + 2gm(e_1e_3 - e_2e_4)z_c + mz_cv_z(t)\omega_y(t) + 2my_cz_c\omega_x(t)\omega_y(t) - mz_cv_y(t)\omega_z(t) + my_c^2\omega_x(t)\omega_z(t) - mz_c^2\omega_x(t)\omega_z(t) - Lmz_c\omega_x(t)\omega_z(t) - my_c^2\dot{\omega}_y(t) + my_cz_c\dot{\omega}_z(t)$

$K51 = -my_c\omega_y(t)^2 - mx_c\omega_x(t)\omega_y(t) - my_c\omega_z(t)^2 - mx_c\dot{\omega}_z(t)$

$K52 = mx_c\omega_x(t)^2 + my_c\omega_y(t)\omega_x(t) + mx_c\omega_z(t)^2 - my_c\dot{\omega}_z(t)$

$K53 = -m\omega_y(t)\omega_z(t)x_c^2 + m\dot{\omega}_x(t)x_c^2 - 2mz_c\omega_x(t)\omega_y(t)x_c + my_c\omega_x(t)\omega_z(t)x_c + my_c\omega_y(t)\dot{\omega}_x... x_c$
$- 2mz_c\dot{\omega}_z(t)x_c + my_cz_c\omega_x(t)^2 - my_cz_c\omega_y(t)^2 - 2gm(e_2e_3 + e_1e_4)z_c + mz_cv_z(t)\omega_x(t) - mz_cv_x(t)\omega_z(t) + mz_c^2\omega_y(t)\omega_z(t) + Lmz_c\omega_y(t)\omega_z(t) - mz_c\dot{v}_y(t) - mz_c^2\dot{\omega}_x(t) - Lmz_c\dot{\omega}_x(t)$

$K54 = m\omega_x(t)\omega_z(t)y_c^2 + m\dot{\omega}_y(t)y_c^2 + 2mz_c\omega_x(t)\omega_y(t)y_c - mx_c\omega_y(t)\omega_z(t)y_c + mx_c\dot{\omega}_x(t)y_c - 2mz_c\dot{\omega}_z(t)y_c + mx_cz_c\omega_x(t)^2 - mx_cz_c\omega_y(t)^2 + 2gm(e_1e_3 - e_2e_4)z_c + mz_cv_z(t)\omega_y(t) - mz_cv_y(t)\omega_z(t) - mz_c^2\omega_x(t)\omega_z(t) - Lmz_c\omega_x(t)\omega_z(t) + mz_c\dot{v}_x(t) - mz_c^2\dot{\omega}_y(t) - Lmz_c\dot{\omega}_y(t)$

$K55 = -mx_c^2\omega_x(t)^2 + 2\text{Ixy}\omega_y(t)\omega_x(t) - 2mx_cy_c\omega_y(t)\omega_x(t) - my_c^2\omega_y(t)^2 - mx_c^2\omega_z(t)^2 - my_c^2\omega_z(t)^2 - mx_c\dot{v}_x(t) - my_c\dot{v}_y(t) - Lmy_c\dot{\omega}_x(t) - my_cz_c\dot{\omega}_x(t) + Lmx_c\dot{\omega}_y(t) + mx_cz_c\dot{\omega}_y(t) + \frac{\text{GJ}}{L}$

Generalized Forces

Here are the generalized forces:

$F1 = m(-x_c\omega_y(t)^2 + v_z(t)\omega_y(t) + y_c\omega_x(t)\omega_y(t) - x_c\omega_z(t)^2 + 2ge_1e_3 - 2ge_2e_4 - v_y(t)\omega_z(t) - L\omega_x(t)\omega_z(t) - z_c\omega_x(t)\omega_z(t) + \dot{v}_x(t) - L\dot{\omega}_y(t) - z_c\dot{\omega}_y(t) - y_c\dot{\omega}_z(t))$

$F2 = m(-y_c\omega_x(t)^2 - v_z(t)\omega_x(t) + x_c\omega_y(t)\omega_x(t) - y_c\omega_z(t)^2 + 2ge_2e_3 + 2ge_1e_4 + v_x(t)\omega_z(t) - L\omega_y(t)\omega_z(t) - z_c\omega_y(t)\omega_z(t) + \dot{v}_y(t) + L\dot{\omega}_x(t) + z_c\dot{\omega}_x(t) + x_c\dot{\omega}_z(t))$

$F3 = m(\omega_x(t)\omega_z(t)x_c^2 - \dot{\omega}_y(t)x_c^2 + L\omega_x(t)^2x_c + z_c\omega_x(t)^2x_c + L\omega_y(t)^2x_c - z_c\omega_z(t)^2x_c + v_y(t)\omega_x(t)x_c - v_x(t)\omega_y(t)x_c + y_c\omega_y(t)\omega_z(t)x_c + \dot{v}_z(t)x_c + y_c\dot{\omega}_x(t)x_c + g(-x_ce_1^2 + 2e_3z_ce_1 -$

131

$e_2^2 x_c + e_3^2 x_c + e_4^2 x_c - 2e_2 e_4 z_c) + z_c \mathrm{v}_z(t)\omega_y(t) + y_c z_c \omega_x(t)\omega_y(t) - z_c \mathrm{v}_y(t)\omega_z(t) - z_c^2 \omega_x(t)\omega_z(t) - Lz_c \omega_x(t)\omega_z(t) + z_c \dot{\mathrm{v}}_x(t) - z_c^2 \dot{\omega}_y(t) - Lz_c \dot{\omega}_y(t) - y_c z_c \dot{\omega}_z(t))) - \mathrm{Iyy}\dot{\omega}_y(t)$

$F4 = \mathrm{Ixx}\dot{\omega}_x(t) + m(\omega_y(t)\omega_z(t)y_c^2 + \dot{\omega}_x(t)y_c^2 + L\omega_x(t)^2 y_c + L\omega_y(t)^2 y_c + z_c \omega_y(t)^2 y_c - z_c \omega_z(t)^2 y_c + \mathrm{v}_y(t)\omega_x(t)y_c - \mathrm{v}_x(t)\omega_y(t)y_c + x_c \omega_x(t)\omega_z(t)y_c + \dot{\mathrm{v}}_z(t)y_c - x_c \dot{\omega}_y(t)y_c + g(-y_c e_1^2 + 2e_4 z_c e_1 - e_2^2 y_c + e_3^2 y_c + e_4^2 y_c + 2e_2 e_3 z_c) - z_c \mathrm{v}_z(t)\omega_x(t) + x_c z_c \omega_x(t)\omega_y(t) + z_c \mathrm{v}_x(t)\omega_z(t) - z_c^2 \omega_y(t)\omega_z(t) - Lz_c \omega_y(t)\omega_z(t) + z_c \dot{\mathrm{v}}_y(t) + z_c^2 \dot{\omega}_x(t) + Lz_c \dot{\omega}_x(t) + x_c z_c \dot{\omega}_z(t))$

$F5 = m(-\omega_x(t)\omega_y(t)x_c^2 - \dot{\omega}_z(t)x_c^2 + y_c \omega_x(t)^2 x_c - y_c \omega_y(t)^2 x_c + \mathrm{v}_z(t)\omega_x(t)x_c - \mathrm{v}_x(t)\omega_z(t)x_c + L\omega_y(t)\omega_z(t)x_c + z_c \omega_y(t)\omega_z(t)x_c - \dot{\mathrm{v}}_y(t)x_c - L\dot{\omega}_x(t)x_c - z_c \dot{\omega}_x(t)x_c + g(-2e_2 e_3 x_c - 2e_1 e_4 x_c + 2e_1 e_3 y_c - 2e_2 e_4 y_c) + y_c \mathrm{v}_z(t)\omega_y(t) + y_c^2 \omega_x(t)\omega_y(t) - y_c \mathrm{v}_y(t)\omega_z(t) - Ly_c \omega_x(t)\omega_z(t) - y_c z_c \omega_x(t)\omega_z(t) + y_c \dot{\mathrm{v}}_x(t) - Ly_c \dot{\omega}_y(t) - y_c z_c \dot{\omega}_y(t) - y_c^2 \dot{\omega}_z(t)) - \mathrm{Izz}\dot{\omega}_z(t)$

REFERENCES

1 D. T. Cameron, Method and apparatus for determining golf ball performance versus golf club configuration, US Patent No. 6669571, (2003).

2 M. J. McNitt, Method and system for presenting information for physical motion analysis, US Patent No. 6567536, (2003).

3 C. J. Funk, Interactive method and apparatus for tracking and analyzing a golf swing, US Patent No. 6533675, (2003).

4 Phasespace *Optics based motion tracking*, Retrieved May 2006 from, http://www.phasespace.com/index.html

5 PTI *Optics based motion tracking*, Retrieved May 2006 from, http://www.ptiphoenix.com/application/science/life_sciences/golf_swing.php

6 BioVision *Optics based motion tracking*, Retrieved May 2006 from, http://www.popularmechanics.com/science/sports/1283176.html

7 L. E. Johnson, Golf swing analysis system, US Patent No. 5907819, (1999).

8 IST Inc *Magnetic marker based motion tracking*, Retrieved May 2006 from, http://www.innsport.com/Sport.htm

9 A. Menache, Motion tracking system and method, US Patent No. 6831603, (2004).

10 Science and motion golf, *Ultra-sound based motion tracking*, Retrieved May 2007 from, http://www.scienceandmotion.de/index.php?lang=en

11 K. K. Tue, W. Kim and F. K. Fuss, Motion synthesis based on anatomical movement of joints during golf swings, *The Engineering of Sport 5,* 1 (2004) 608-614.

12 M. Tsunoda, R.C.H. Bours and H. Hasegawa, Three-dimensional motion analysis and inverse dynamic modeling of the human golf swing, *The Engineering of Sport 5,* 2 (2004) 326-332.

13 T. Iwatsubo, K. Adachi, T. Aoki, M. Onuki and H. Kakiuchi, A study of the 2D dynamic simulation for the golf swing, *The Engineering of Sport 5,* 2 (2004) 389-395

14 G. S. Simon and A. J. Rankin, A three-dimensional examination of the planar nature of the golf swing, *Journal of Sports Sciences*, *v 23 i 3* (2005) 227-235

15 A. D.Penner, The physics of golf, *Reports on Progress in Physics, 66* (2003) 131-171.

16 C. L. Vaughan, A three-dimensional analysis of the forces and torques applied by a golfer during the downswing, *Biomechanics VII-B,* (1979) 325-331

17 P. D. Milburn, Summation of segmental velocities in the golf swing, *Med. Sci. Sports Exercise, 14* (1982) 60–64

18 M. A. J. Cooper and J. S. B. Mather, Categorizations of golf swings, *Science and Golf II, St. Andrews, Scotland, July, 1994*, pp. 65-70.

19 M. McTeigue, S. R. Lamb, R. Mottram and F. Pirozzolo, Spine and hip motion analysis during the golf swing, *Science and Golf II, St. Andrews, Scotland, July, 1994*, pp. 50-58.

20 R. L. Robinson, A study of the correlation between swing characteristics and club head velocity, *Science and Golf II, St. Andrews, Scotland, July, 1994*, pp. 84-90.

21 K. Mitchell, Shoulder motions during the golf swing in male amateur golfers, *Journal of Orthopedic and Sports Physical Therapy*, *v 33 i 4* (2003) 196-203.

22 J. S. Wheat, The measurement of shoulder alignment during the golf drive, *Journal of Sports Sciences*, *v 32 i 2* (2005) 101.

23 C. J. Gatt, Three-dimensional knee joint kinetics during a golf swing- Influences of skill level and footware, *American Journal of Sports Medicine*, *v 26 i 2* (1998) 285-294.

24 N. C. Perkins, Electronic measurement of the motion of a moving body of sports equipment, US Patent No. 7021140, (2006).

25 N. C. Perkins, Electronic measurement of the motion of a moving body of sports equipment, US Patent No. 7,234,351, (2007)

26 N. Yazdi, F. Ayazi and K. Najafi, Micromachined inertial sensors, *Proceedings of the IEEE*, *86* (1998) 1640-165.

27 D. H. Titterton and J. L. Weston, *Strapdown Inertial Navigation Technology*, The Institution of Electrical Engineers, Stevenage, UK and The American Institute of Aeronautics and Astronautics, Reston, USA, 2nd edn., 2004, pp. 189-216.

28 Kionix *MEMS accelerometers,* Retrieved June 2007 from, http://www.kionix.com/accelerometers/accelerometers.html

29 M. F. Zaman, A. Sharama and F. Ayazi, High performance match-mode tuning fork gyroscope, *Proceedings IEE Conference on MEMS, 2006, Istanbul, Turkey, 22-26 January, 2006,* pp. 66-69.

30 J. A. Green, S. J. Sherman, J. F. Chang and S. R. Lewis, Single-chip surface micromachined integrated gyroscope with 50°/h allan deviation, *IEEE Journal of Solid-State Circuits, v 37 i 12* (2002) 1860-1866.

31 R. L. Kubena, D. J. Vickers-Kirby, R. J. Joyce, F. P. Stratton, and D. T. Chang, A new tunneling-based sensor for inertial rotation rate measurements, *Sensors and Actuators A 83* (2000) 109-117.

32 X. Jiang, J. I. Seeger, M. Kraft, and B. E. Boser, A monolithic surface micromachined z-axis gyroscope with digital output, *Symposium on VLSI Circuits Digest of Technical Papers*, *2000,* pp. 16-19.

33 Analog Devices *MEMS angular rate sensors*, Retrieved June 2007 from, http://www.analog.com/en/subCat/0,2879,764%255F801%255F0%255F%255F0%255F,00.html

34 P. G. Savage, *Strapdown Analytics*, Strapdown Associates, Inc., Maple Plane, 2002, pp. 18.77-18.103.

35 R. M. Rogers, *Applied Mathematics in Integration Navigation Systems*, American Institute of Aeronautics and Astronautics, Inc. (AIAA), Reston, 2003, pp. 163-178.

36 N. J. Lee, Instrumented golf club system and method of use, US Patent No. 6224493, (2001)

37 A. Bedford and K. Liechti, *Mechanics of Materials*. Prentice Hall, Upper Saddle River, 2000.

38 T. R. Kane, R. R. Ryan and A. K. Banerjee, Dynamics of a cantilever beam attached to a moving base, *Journal of Guidance, Control and Dynamics, v 10 i 2*, (1987) 139-151.

39 J. H. Bulter and D. C. Windeld, The dynamic performance of the golf shaft during the downswing, *Science and Golf II, St. Andrews, Scotland, July, 1994*, pp. 259-264.

40 A. Yigit, R. A. Scott and G. Ulsoy, Flexural motion of a radially rotating beam attached to a rigid body, *Journal of Sound and Vibration, v 121 i 2*, (1988) 201-210

41 D. Pelz, *David Pelz's Putting Bible*. Doubleday, New York, 2000.

42 B. Lowe, Centrifugal force and the planar golf swing, *Science and Golf II, St. Andrews, Scotland, July, 1994*, pp. 59-64.

43 T. R. Kane, P. W. Likins and D. A. Levinson, *Spacecraft Dynamics,* McGraw-Hill, New York, 1983, pp. 58-60.

44 L. Mangiacasale, *Flight Mechanics of a µ-Airplane with a MATLAB Simulink Helper,* Edizioni, Libreria CLUP, Milan, 1998.

45 S. Utley, *The Art of Putting*. Gotham Books, New York, 2006.

46 E. Craig, *Putt Perfect*. Hamlyn, London, 2005.

47 Clubmaker-online.com *Image of Bobby Jones' Golf Swing*, Retrieved Sept. 2005 from, http://www.clubmaker-online.com/bj003.gif

48 K. R. Williams and B. L. Sih, Changes in golf clubface orientation following impact with the ball, *Sports Engineering, v 5* (2002) 65-80

49 G. P. Horwood, Golf shafts – a technical perspective, *Science and Golf II, St. Andrews, Scotland, July, 1994*, pp. 245-258.

50 Golfsmith *Club head and golf shaft dimensions and properties*, Retrieved May 2007 from, http://www.golfsmith.com

51 E. P. Popov, *Introduction to mechanics of solids*, Prentice Hall, Englewood Cliffs, 1968, pp. 143-177